The study of the interactions between a low pressure steam turbine and axial-radial diffuser

by

Gursharanjit Singh

Submitted in partial fulfilment of the requirements

of the Degree of Doctor of Philosophy

School of Engineering and Materials Science,

Queen Mary University of London

December 2014

The study of the interactions between a low pressure steam turbine and axial-radial diffuser

by

Gursharanjit Singh

(Student ID: 100544008)

Submitted in partial fulfilment of the requirements

of the Degree of Doctor of Philosophy

Supervisor: Dr. Andrew P.S. Wheeler

School of Engineering and Materials Science

Queen Mary University of London

December 2014

Statement of originality:

I, Gursharanjit Singh, confirm that the research included within this thesis is my own work or that where it has been carried out in collaboration with, or supported by others, that this is duly acknowledged below and my contribution indicated. Previously published material is also acknowledged below.

I attest that I have exercised reasonable care to ensure that the work is original, and does not to the best of my knowledge break any UK law, infringe any third party's copyright or other Intellectual Property Right, or contain any confidential material.

I accept that the College has the right to use plagiarism detection software to check the electronic version of the thesis.

I confirm that this thesis has not been previously submitted for the award of a degree by this or any other university.

Signature: Gursharanjit Singh

Date: 17/12/2014

Details of collaboration and publications (peer reviewers recommended it as a journal quality paper):

Singh, G.; Singh, G.; Wheeler, A.P.S.;, The effect of rotor casing on low pressure steam turbine and diffuser interactions. GT2015-43030, Proceedings of ASME Turbo Expo 2015: June 15-19, 2015

Title of thesis:

The study of the interactions between a low pressure steam turbine and axial-radial diffuser.

Abstract:

Specific power output from a Low Pressure (LP) steam turbine can be enhanced by increasing the stage efficiency or raising its pressure ratio; both methods are interlinked and must be dealt with together. The latter is achieved by connecting to the exhaust diffuser; space and cost constraints often insist the use of an axial-radial diffuser with high levels of diffusion. The present study aims to investigate the interaction between the last-stage blade and the axial-radial diffuser, which can influence the diffuser performance and thus the total work output from the stage. This work is carried out using CFD simulations of a generic last stage low pressure (LP) turbine and axial-radial exhaust diffuser attached to it. In order to determine the validity of the computational method, the CFD predictions are first compared with data obtained from an experimental test facility. A computational study is then performed for different design configurations of the diffuser and rotor casing shapes. The study focuses on typical flow features such as effects of rotor tip leakage flows and subsequent changes in the rotor-diffuser interactions. The results suggest that the rotor casing shape and diffuser configurations influences the rotor work extraction capability and yields significant improvements in the static pressure recovery.

Acknowledgements

It would not be possible for me to complete this thesis without support of many people involved with it. Firstly, I would like to thank my supervisor, Dr. Andrew P.S. Wheeler, for giving me an opportunity to work under his guidance. Andy, through his unwavering passion kept my spirits up and encouraged me to work systematically in order to produce a good quality research. He is an exceptionally gifted researcher and a mentor with constant enthusiasm to uncover the underlying flow mechanisms and, above all, has a genuine concern for others. I feel lucky to have a supervisor like him who worked more like a fellow teammate than a boss and always showed great sense of patience and compassion while I used to make mistakes on regular basis.

I am grateful to Prof. John Denton for providing his CFD solver and turbine geometries along with his initial comments. I am thankful to Dr. Brian R. Haller, Alstom Power for sharing his ideas that lead to formulation of this project. Despite busy schedules, he was always available to answer my calls and brought different perspective that helped in broadening the scope of this thesis. I am also thankful to him for giving his kind permission to use Alstom's rig test results. At the same time, I would acknowledge Dr. Gurnam Singh, Alstom Power for sharing his expert thoughts on developing CFD simulations. I am greatly indebted to Dr. Sungho Yoon who motivated me to pursue a doctorate degree and spent a lot of time in giving me regular project feedbacks. I cherish frequent encouragements from these researchers while unwearyingly providing their technical inputs on this study.

I am thankful to School of Engineering and Materials Science, QMUL for providing a studentship to fund my studies. I also thank my second supervisor, Dr. Jens D. Mueller for his administrative support in absence of Dr. Wheeler. Jonathon Hills, Rajesh Chadha, Mick Etheridge and Dennis Ife were always helpful in fulfilling my administrative requirements. I will miss Late Raymond Lam for his extraordinary willingness to help others in need.

The time spent in both QMUL and London was made much more enjoyable in the company of highly motivated and fun-loving friends. I am indebted to my parents, Sd. Gurmukh Singh and Sdn. Manjit Kaur and my sisters, Aman and Raman, for their love and support in all my endeavours. At the same time, I missed my family a lot especially my young niece and nephews, Ekkam, Inesh and Tejas. Finally, I thank almighty for showering his blessings on me and giving me an opportunity to pursue a Ph.D. degree.

Table of Contents

List of Figures

List of Table

Nomenclature

P	Static pressure
P_o	Stagnation pressure
T	Static temperature
T_o	Stagnation temperature
η	Efficiency
τ	Wall shear stress
v	Velocity along the surface/radial velocity
δ	Boundary layer displacement thickness
S_a	Entropy generation per unit surface area
S	Total entropy generated
ρ	Density
C_D	Boundary layer dissipation coefficient
C_{ax}	Blade axial chord

Δs	Change in entropy
R	Gas constant/Radii of blade
γ	Heat capacity ratio
c_p	Specific heat capacity at constant pressure
c_v	Specific heat capacity at constant volume
M	Mach number
g/h	Tip gap as a fraction of span
c/s	Pitch to chord ratio
C_d	Discharge coefficient
V_s	Suction side velocity
V_p	Pressure side velocity
CP	Diffuser pressure recovery coefficient
Y_s	Diffuser pressure loss coefficient
ζ	Effective area change/Blockage
V_x	Axial velocity
V_r	Radial velocity
V_t	Tangential velocity
E	Energy
I	Streamwise direction
J	Spanwise direction

K	Pitchwise directcion
m	Mass flow
W_m	Meridional speed
A	Area
I	Rothalpy
I_m	Moment of momentum
ω	Rotational speed
h_s	Static enthalpy
h_o	Stagnation enthalpy
SysPr	System pressure ratio (P_o/P)
s/So	Normalised length
r/R	Normalised radii
Δs/R	Normalised entropy change
θ	Tangential direction
u	Blade speed
a	Sonic speed
S/H	Diffuser casing axial length : blade height
L/H	Diffuser hub axial length : blade height
AR	Diffuser area ratio

1: Introduction

Chapter Outline:

This chapter will discuss the importance of steam turbines in the energy sector and in particular, the requirement to improve the performance of the coupled low pressure steam turbine and diffuser. This chapter also discusses the typical operating conditions, current knowledge in this area, and then outlines the structure of this thesis.

1.1 Background of the study

Since the advent of industrialisation, energy has played a key role in the development of humanity and its sustainability across the world. Energy rich nations have high capability towards growth which correlates directly with the living standards of its people and their GDP (Gross Domestic Product). Be it the recent US shale gas revolution, the Chinese investment in hydroelectric power, the decline in Japanese nuclear power production or climate change talks and diversification of power resources, energy is constantly in the news. Although socio-economic and political drivers often play an important role in energy requirements, the recent shale gas revolution demonstrates that technological improvements are always critically important in terms of improving energy efficiency and reducing energy demand. While the current energy consumption trends for OECD (Organisation for Economic Co-operation and Development) economies remain stable, there has been a 30% increase in energy consumption in the non-OECD nations over the last decade (C. Ruhl 2013). Figure 1.1 shows the world energy consumption during the last 46 years for each major fuel type. Hidden within Figure 1.1 are two recent trends: OECD nations are shifting towards greener technologies and non-OECD nations are bound to increase, due to high demand, in their non-renewable (coal) consumption (Luckemeyer, et al. 2011).

With booming industrialisation in the developing economies (China followed by India) that fall outside OECD sector, the non-renewable (coal) consumption is expected to rise at a rate of 1.1% per annum in the next decade(Ruhl 2014). This is due to cheap and abundant availability of coal reserves across these nations; International Energy Agency (IEA) estimates show that currently coal provides 40% of the world electricity. Improvement in the efficiency of electricity production can be made using existing proven technologies such as: Fluidised Bed Boilers (FBD), supercritical cycles, reheating and regeneration of steam at

higher temperatures via feed water heaters; and are found to be economically viable for most of the power plants. Additionally, simple design strategies such as single-shaft compounding, double flow low pressure steam turbines help reduce both construction costs and machine efficiencies. However, the promising carbon reduction technologies such as Integrated Gasification Combined Cycle (IGCC) and Carbon Capture and Storage (CCS) are yet to pass their large scale commercial viability tests. The carbon mitigation initiative at Princeton University concludes that it is hard to maintain constant carbon content by using current technologies (Pacala and Socolow 2004), (Socolow and Lam 2007). Nevertheless, non-renewable fuels such as coal, natural gas and nuclear fuels are bound to remain important in future and the majority (>60%) of the world's energy production is made through steam turbine power plants using these natural resources. Thus, it becomes essential to endeavour on improving the efficiency of these machines.

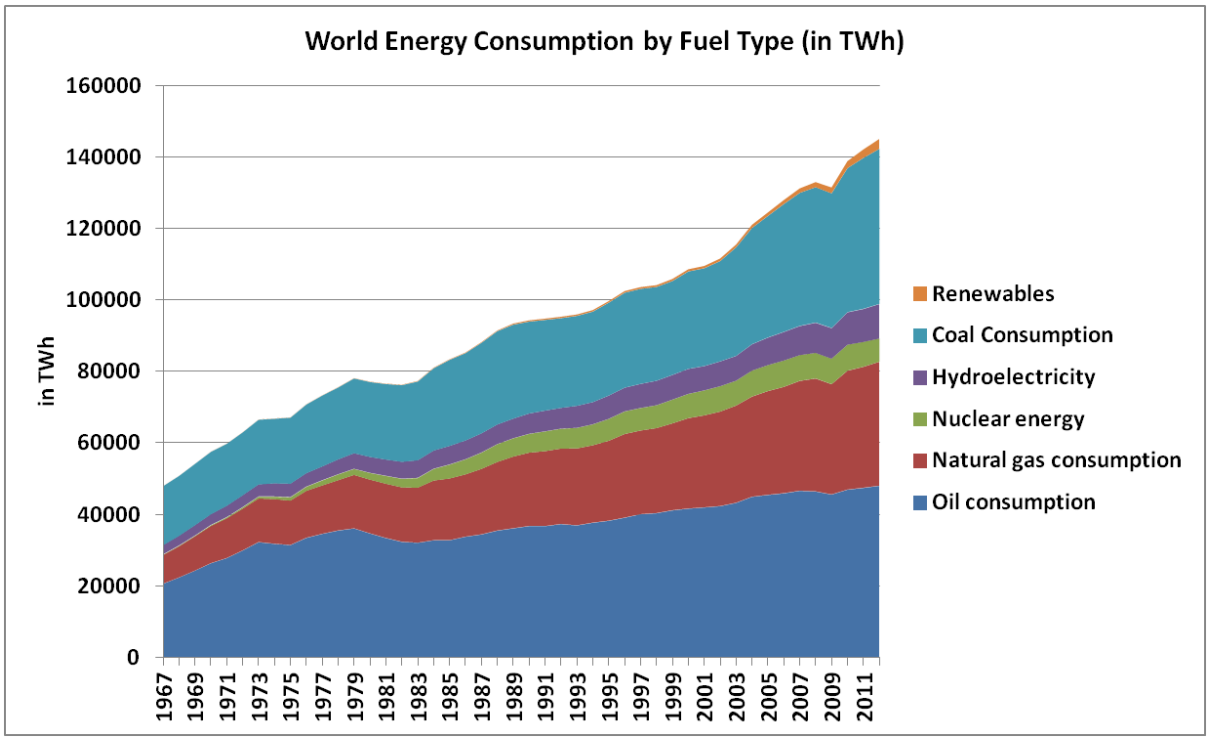

FIGURE 1.1. WORLD ENERGY CONSUMPTION BASED ON FUEL TYPE (IN MWH), (C. RUHL 2013)

A steam turbine is a turbomachine that extracts thermal energy via aerodynamic action from a pressurised hot steam (typically produced by burning fuels) and uses it to do mechanical work on a rotating output shaft. For any power plant, steam turbines contain primarily three sections: High pressure (HP), Intermediate pressure (IP) and Low pressure

(LP). These sections vary considerably in size, power output and flow rate. For example, in a conventional power plant one HP turbine being connected to three double flow LP turbines (see Figure 1.2) is not uncommon. The design conditions at the inlet of HP turbine can reach around 650^{o}C/250Bar, while a typical LP outlet is designed to operate at 40^{o}C/0.07Bar. Large variations in the flow conditions require entirely different design strategies that often reach both aerodynamic and mechanical limits of these machines. At the same time these machines are expected to operate around the year and variations in guaranteed efficiency can differentiate between a highly successful and a failed product. Thus, further improvements in the efficiency of steam turbines are important in order to meet both increasing contractual obligations, power needs and controlling fuel costs with less exploitation of natural resources.

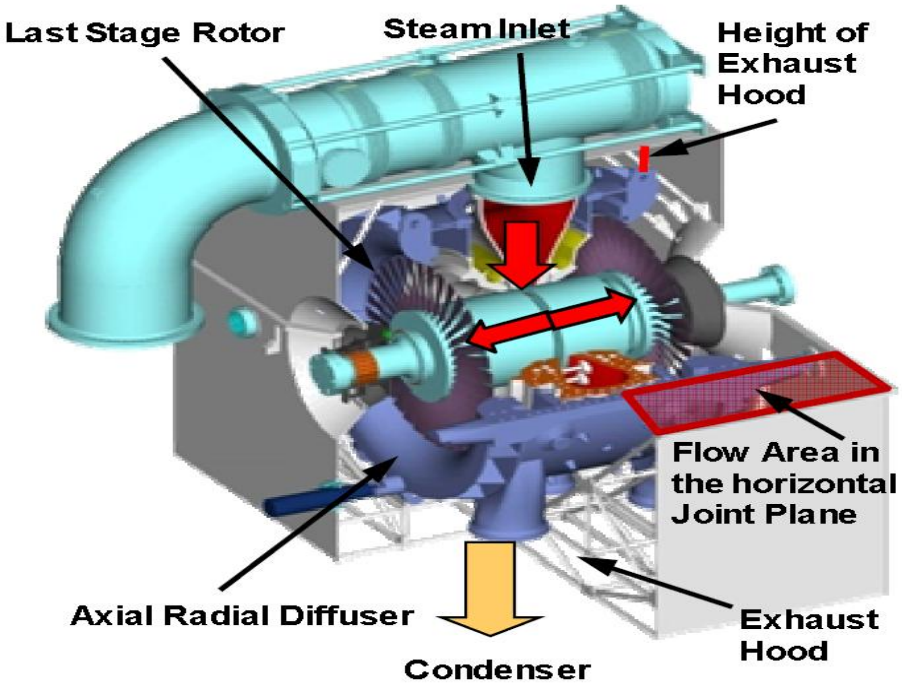

FIGURE 1.2. A TYPICAL EXAMPLE OF A DOUBLE FLOW LP STEAM TURBINE (FINZEL, ET AL., 2011)

Over the past few decades, the technology has been developed to use longer last stage blades (Stuer H. 2005) in steam turbines and these are now contributing up to 20% of the total power produced in the steam power plants (McBean, I.; Havakechian, S.; Masserey, P.-A. 2010). This value has been reported as 50% for the utility-scaled steam turbines that are used in the process industries (Zachary, Justin; Koza, Donald J. 2006).

1.2 Current Knowledge

Specific power output from a Low Pressure (LP) steam turbine can be enhanced by increasing its internal efficiency or raising the pressure ratio across its ends. Improvements in efficiency can be achieved through better designs such as exploiting fully 3D blading (Haller and Hesketh 1993), (Stuer H. 2005), (Denton and Xu, 1998), or a reduction in the internal losses (J. Denton, 1993). Advance design strategies such as nozzle blade lean are increasingly used in modern LP turbine blades (Ono, et al. 2013). Improvements in the overall turbine efficiency can also be achieved by connecting the turbine to an exhaust diffuser. The flows within steam turbine exhausts are highly complex and the nature of the flow inside the diffuser is still unknown to a great extent (Yoon, Stanislaus, et al. 2011). A large number of diffuser performance mappings (channel, conical, annular) have been studied(Sovran and Klomp 1967) and compiled (for instance (Japikse and Baines 1998)). However these mappings cannot be used directly for axial-radial diffusers (common for steam-turbine exhausts). One of the main reasons for this is the short axial length available for most of the industrial designs, which commonly necessitates an axial-radial design (see Figure 1.2). Furthermore the flow exiting the last stage is highly non-uniform and the influence of this spatial and temporal non-uniformity on the diffuser performance is not well understood. For example, as a general trend, an axial-radial channel diffuser will have lower pressure recovery when compared to its axial counterpart for a given area ratio (Japikse and Baines 1998). For axial-radial steam turbine diffusers, although both total pressure and swirl angle changes are important ((Liu and Hynes 2003),(Fu, Liu and Zhou 2012), (Becker, Gretschel and Casey 2005) and (Hirschmann, Volker, et al. 2012)) the exact mechanism of performance changes is not well understood due to the three-dimensional nature of the flow. Axial diffusers tend to have more uniform exit flows but necessarily require greater axial length for the same diffusion, and hence due to high costs are not practical to use with steam turbines.

LP steam turbines are by far the most powerful class of turbomachines and the design conditions include high Mach number regions (1.5 < peak Mach numbers < 2.2), three dimensional and unsteady wet steam flows. They often require titanium alloy blading (to sustain large stresses) and currently these machines can be expected to operate for 34000 hours with a reliability of 99% availability and 2400 normal starts between major outages (Haller 2005). Aerodynamically, the size of the last stage blades depends on the flow

expansion and condenser conditions. The height of a low hub to casing ratio last stage blade can vary between 26 inch (0.6604m) to 74 inch (1.8796m) depending on the machine rotational speed and required pressure ratios. The study of diffuser inlet non-uniformities, wetness effects, droplet size modelling and unsteadiness effects such as blade row interactions by wake chopping and rotating instabilities have been made by different researchers such as (Starzmann, et al. 2011), (Chandler, White and Young 2011), (Tanuma et al., 2012) and (Zhang, He and Stuer 2013). Their findings suggest that modelling of wet steam flow is still complex and requires a separate study in its own right. Thus, such effects will be kept outside the scope of this study. Further insights into the development of last stage blades and typical flow and mechanical design conditions can be gained by referring to works of Mitsubishi (Fukuda, H.; Ohyama, H; Miyawaki, T; Mori, K; Kadoya, Y; Hirakawa, Y 2009), Bechtel (Zachary, Justin; Koza, Donald J. 2006), Alstom (McBean, I.; Havakechian, S.; Masserey, P.-A. 2010), Hitachi (Senoo, 2012)/(Mizumi, S.; Ishibashi, K. 2013), Toshiba (Tanuma, Sasao, et al., 2011) and Siemens (Luckemeyer, et al. 2011). These authors have covered the development of last stage blades from a broader perspective by comparing real industrial data on LP steam turbines. The understanding into the operating design range of the low pressure steam turbines has been compiled from a real power plant case study by (Raj 2008). For this study, it assumed that the fluid-dynamic limits of a LP steam turbine are reached much earlier than the mechanical limits, and the performance of the last stage blades varies with the variation in condenser conditions (with a peak performance at the designed conditions).

Significant technological improvements have been made in the understanding of the flow physics inside a blade passage (Sakuma, Matsuura and Kodama 2007) and its exhaust diffuser (Yoon, Stanislaus, et al. 2011); in general the exit flow from the last stage blade (LSB) is non-uniform with large variations in the spanwise reaction; the primary flow is affected by the tip leakage jet and other secondary flows generating a highly three-dimensional flow. Within the diffuser, casing side separations tend to limit the maximum achievable diffusion of the flow, making casing shape optimisation essential at the initial design stage. A further compilation of LP steam turbine exhaust hood literature is given by (Burton, Ingram and Hogg 2013a). However, the main focus of the literature remains on the exhaust hood flow structure rather than the diffuser flow, where the majority of the pressure recovery occurs. Other factors (see Figure 1.3) such as blade wakes, spanwise flow

variations, leakage flows, diffuser casing shocks, are key in modifying the performance of both the rotor and the diffuser flow. Apart from these, ultra long blade design space (>50inch) can experience supersonic inlet/exit conditions especially near the casing side (Senoo, 2012), thus requiring reversed cambered supersonic flow sections.

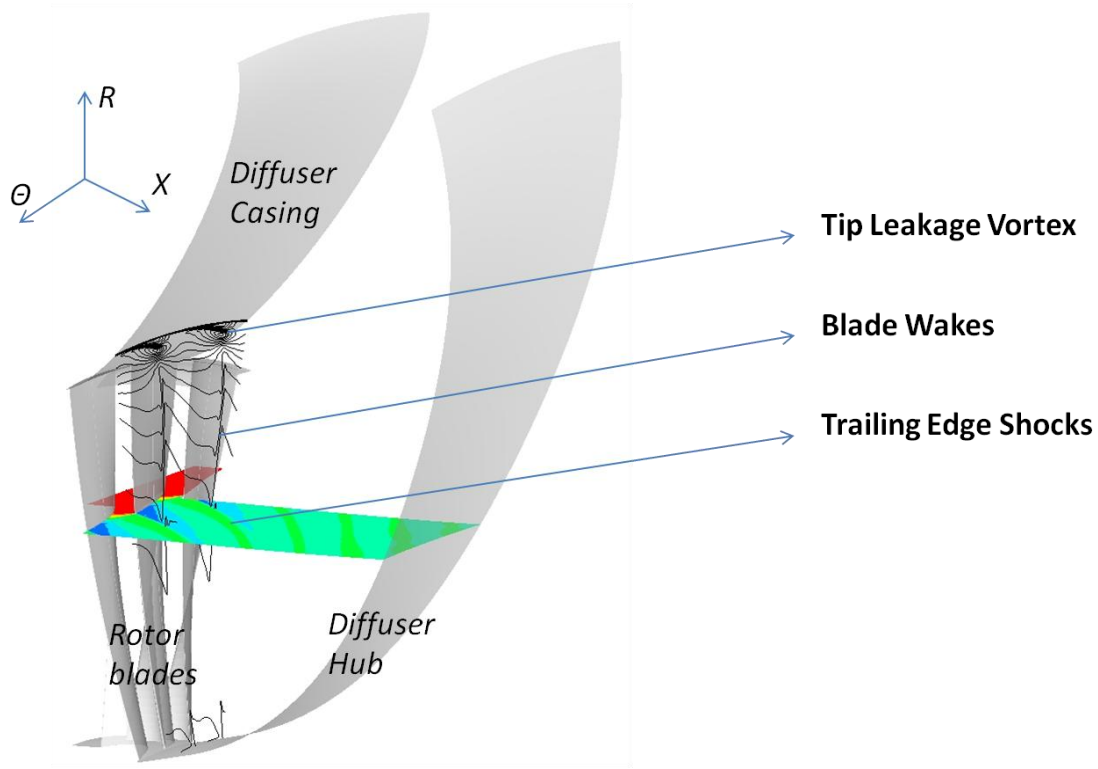

FIGURE 1.3. FLOW FEATURES AT THE EXIT OF THE LAST STAGE BLADES (COLOURED CONTOUR IS A STATIC PRESSURE FIELD AND LINE CONTOUR IS A MACH NUMBER FIELD)

1.3 Thesis Scope and Outline

This thesis examines the interaction of the both viscous and inviscid flow features on the fluid-dynamic coupling between last stage of a low pressure steam turbine and its axial-to-radial diffuser. This investigation has the following main objectives:

- To determine the key interaction mechanisms between the LSB and diffuser. This includes understanding the relative changes in the defined performance factors and general dynamics.
- Quantify the effect of casing and diffuser shape on these flow features, and hence system performance.
- Translate this knowledge into design recommendations.

In order to meet these objectives a series of computational studies were performed of different design configurations of last stage blade and its diffuser. The interacting flow features were identified as flow streamline curvature, tip leakage flow, blade wakes, trailing edge shocks and diffuser casing side shocks. These flow features are fundamental to any long last-stage blade in a low pressure steam turbine. The interaction of these flow phenomena was either studied by numerically isolating them or by making geometrical changes to the design. The thesis structure is as follows:

- General concepts in steady flow physics including the origins of loss mechanisms and their effect on the performance in steam turbine blades and diffusers are discussed in chapter 2. This chapter also reviews the work carried out by other researchers on flow coupling covering both numerical and experimental studies on the subject.
- Chapter 3 describes the methodology, flow solver, calculations set-up used in this study and the validation of the solver against the industrial collaborator's experimental data.
- Chapter 4 describes the three dimensional flow regime in a generic last stage blade and its axial-radial diffuser. The flow features playing a key role in the turbine-diffuser coupling are described. It does so by isolating the flow features via numerical case studies and determining their relative effects on diffuser and system performance.
- Chapter 5 describes the effects of casing side supersonic flow on the turbine-diffuser coupling. This is achieved by studying the effect of casing shape on both rotor and diffuser performance.
- Chapter 6 provides a parametric study of different diffuser and rotor tip gap variations on overall system performance, studying the effects of diffuser length, area ratio and tip gap.
- The discussion of the current work, conclusions and subsequent recommendations for the future work are made in chapter 7.

2: Literature review

Chapter Outline:

This chapter reviews the current state-of-knowledge regarding low pressure steam turbine flows. It will explain the flow physics while covering the effects of loss mechanisms of boundary layer, mixing processes, shock waves, tip leakage flows, profile loss mechanisms and end-wall losses. Further, this chapter will cover LSB-diffuser coupling, diffuser design methods, diffuser performance measurements. Finally, the present level of research on last-stage and diffuser coupling will be covered and gaps are literature identified.

2.1. Introduction

As highlighted in the previous chapter, the present study concentrates on adding to the current understanding of the flow field inside the last stage of a low pressure steam turbine, and in particular on determining the interaction mechanisms with the downstream diffuser. This improvement in the current knowledge can only be regarded as forming part of a wider body of work into the design and fluid dynamics of low pressure steam turbines which has been ongoing for many years. Thus the following discussion is not an exhaustive summary of the work done in the field, but instead aims to capture the current understanding of the relevant flow features.

The specific power output from a Low Pressure (LP) steam turbine can be enhanced by connecting it to an exhaust diffuser, which increases the static pressure ratio across the last-stage by reducing the static pressure at rotor exit; this is because, for a given exhaust pressure, the diffuser enables a lower rotor exit pressure by converting some of the kinetic energy leaving the rotor into a static pressure rise across the diffuser. Specific power can also be increased by reducing aerodynamic losses, and thus increasing component efficiencies. The following discussion is thus in two main parts; the sources of turbomachinery losses are first described, then diffuser flows, design and performance are then discussed.

2.2. Loss mechanisms for LSB and diffuser flow

Figure 2.1 gives the representational diagram for the last stage blades and a diffuser system. From stage inlet '1' to exit '2', the red line depicts the isentropic drop in enthalpy across the last stage blades. Similarly, the blue and green lines depict the non-isentropic change in enthalpy of the steam flow with respect to the pressure isobars P_{o1}, P_{o2} and P_2. A diffuser attached downstream of the stage, gives rise to the stage exit static pressure from P_2 to P_3, thus adding to the enthalpy change across the stage by letting it operate at P_2. At the same time, the diffuser undergoes a non-isentropic process that leads to a drop in total pressure (P_{o2} to P_{o3}). Entropy production in both the turbine and the diffuser therefore lead to a reduction in available work output. Therefore, understanding of the loss generating mechanisms becomes essential to study the interactions between last stage blades and diffuser.

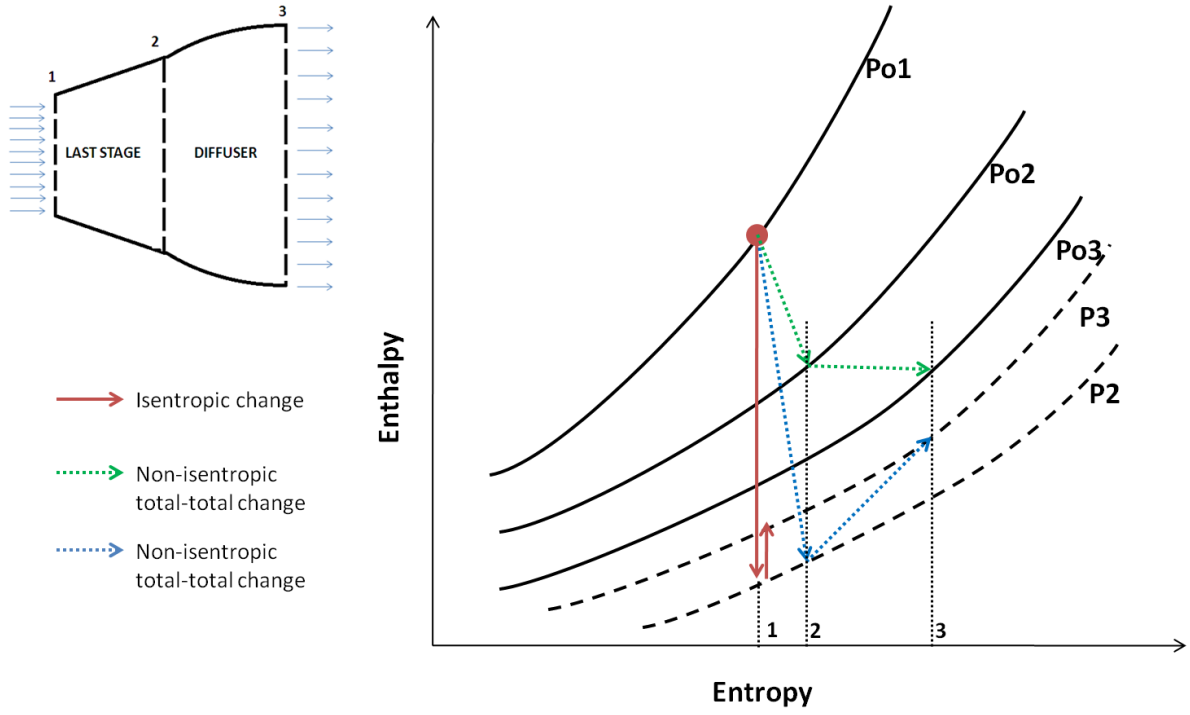

FIGURE 2.1. THERMODYNAMIC REPRESENTATION OF THE LAST STAGE AND DIFFUSER SYSTEM

The standard definition of loss can be regarded as any flow feature that reduces the machine efficiency, (J. Denton, 1993). For any turbine or a turbine-diffuser system, the usual definition of efficiency is based on the actual work output against the isentropic work output, as shown below:

$$\eta = \frac{\text{Work Output}}{\text{Isentropic Work Output}} \quad \textbf{(2.1)}$$

This definition implies that only rises in entropy can reduce the efficiency and since entropy is only generated by heat transfer or flow irreversibility, "the only rational measure of loss in an adiabatic machine is entropy creation", (J. Denton, 1993).

The disadvantages of using entropy are that it cannot be measured directly and that only changes in entropy have any meaning, necessitating the measurement of reference conditions. For the purpose of this study, unless specified, only isentropic efficiencies are used to calculate the performance of the last stage turbine rotor. However, since the leaving energy exiting the rotor can be recovered by the diffuser downstream, the meaningful measure of rotor performance in the last stage will be a total-to-total efficiency (determined from the total pressure ratio) whereas the system (rotor-diffuser) efficiency can be computed as total-to-static efficiency (determined from the system total-to-static pressure ratio). Throughout this thesis, steam will be approximated as an ideal gas, which simplifies the estimation of efficiency based on the gas temperature. Subsequent chapters will employ these definitions while specifying the efficiencies for both rotor and system as shown below:

$$\eta_{\text{total-total, rotor}} = \frac{T_{\text{o, rotor inlet}} - T_{\text{o, rotor exit}}}{T_{\text{o, rotor inlet}} - T_{\text{os, rotor exit}}} \quad \textbf{(2.2)}$$

$$\eta_{\text{total-static, system}} = \frac{T_{\text{o, system inlet}} - T_{\text{o, system exit}}}{T_{\text{o, system inlet}} - T_{\text{s, system exit}}} \quad \textbf{(2.3)}$$

There are three fundamental loss generating processes: viscous dissipation, heat transfer and non-equilibrium processes (J. Denton, 1993). In order to provide a clearer physical insight into the flow field, these loss sources can be divided into the various components of the two-dimensional (2D) and three-dimensional (3D) losses, although they are often indistinguishable from each other. Although 3D loss mechanisms can be much larger than 2D losses, 2D loss mechanisms are much better understood. The following discussion describes the important loss mechanisms relevant to this thesis. It should be noted that since all walls in the computational domain are assumed to be adiabatic in this thesis, the effects of heat transfer from the flow will not be considered here.

2.2.1 Two-dimensional loss mechanisms

The loss in a two-dimensional flow field through a blade row can be sub-divided into:

- Boundary layer loss: Generated by shear stresses in the boundary layers.
- Shock loss: Generated by shock waves in the flow field at high Mach numbers.
- Mixing loss: Generated by mixing of the flow field behind the blade trailing edge.

2.2.1.1 Boundary layer loss

A boundary layer on the blade surfaces or domain wall consists of multiple levels of shear layers that generate entropy due to presence of shear stresses acting on the flow. This process can effectively be termed as conversion of viscous shear work into internal energy (J. Denton, 1993) as shown at a boundary layer edge (δ) below:

$$\dot{S}_a = \int_0^{\delta} \frac{\tau}{T} \frac{dv}{dy}\, dy \qquad (2.4)$$

where $\dot{S}_a$ is the total entropy generation rate per unit area. Thus, most of the entropy generation takes place in the regions where the shear stress is maximum, which is normally in the inner part of the boundary layer. For turbulent boundary layers most of the entropy is generated in the viscous sub-layer and the turbulent wall region. (Wallace and Davies 1997) defined the entropy sub-layer as the near wall region within the boundary layer where 99 % of the entropy is generated.

The entropy production rate per unit surface area can be converted into a dissipation coefficient which can be defined as:

$$C_D = \frac{\mathrm{T}\,\dot{\mathrm{S}}}{\rho v_{\delta}^3} \qquad (2.5)$$

The magnitude of entropy generation requires a complete knowledge of the boundary layer but experimental correlations can provide general results as highlighted by (Thorpe, et al. 2007) and (Miller and Denton 2012). The dissipation coefficient is dependent on both the momentum thickness Reynolds number and the state of the boundary-layer (laminar or turbulent). Typical values for a zero pressure gradient are depicted in Figure 2.2; this figure shows that in regions where both laminar and turbulent boundary-layers could exist,

turbulent boundary-layers generate several times more loss than a laminar boundary-layer. The effects of pressure gradient are usually small, with a slight increase in dissipation for accelerating flow. Thus, the total entropy generated is found by integrating over the axial length of the blade for both surfaces:

$$\dot{S} = \int_0^{C_{ax}} \frac{\rho v_\delta^3 C_D}{T_\delta} dx \qquad \textbf{(2.6)}$$

The above equation gives a general rule that the suction side of the blade boundary layer will give a larger share of the total entropy production due to the higher flow speeds near the suction-side. Strong adverse pressure gradients, such as from impinging shock-waves, can increase boundary-layer losses further, by causing separations which lead to intense mixing in the region of reattachment. Such interactions commonly occur on the suction surface of the last stage rotor blades near to the tip, and also on the diffuser casing boundary layer, as discussed later in this thesis.

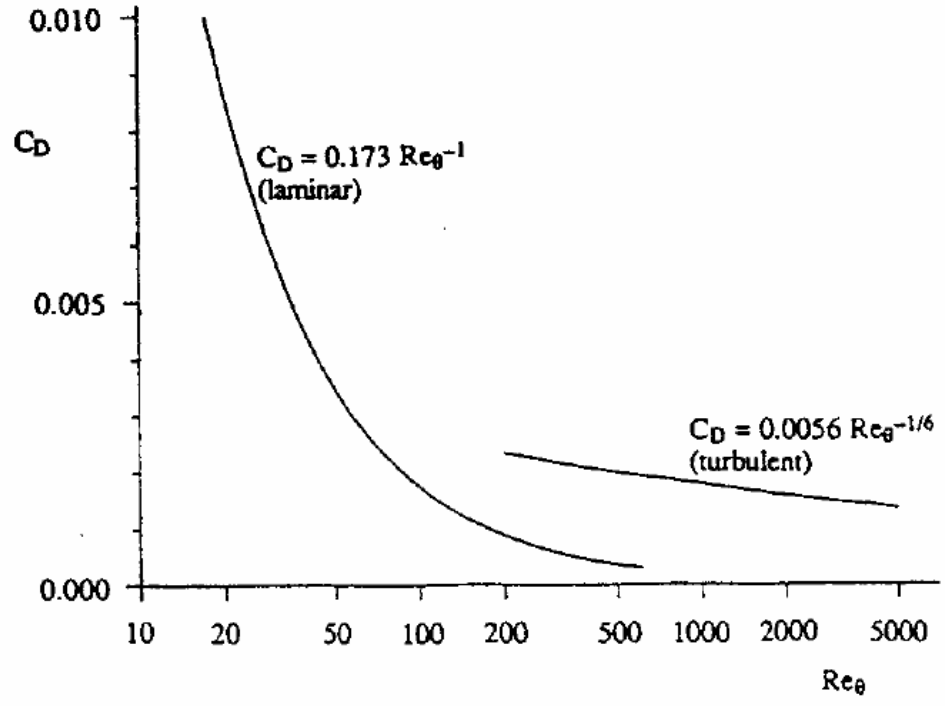

FIGURE 2.2. DISSIPATION COEFFICIENT FOR LAMINAR AND TURBULENT BOUNDARY LAYERS (J. DENTON, 1993)

2.2.1.2 Shock losses

In the absence of boundary-layers and other viscous effects, the entropy creation across a shock wave occurs due to heat conduction and the presence of high viscous normal stresses typically within a thickness of a few molecular mean free paths. For weak normal shock waves the corresponding entropy rise is given by (Tyler and Shapiro 1953) and (Delery and Marvin 1986):

$$\Delta s \cong \frac{2\gamma}{3(\gamma+1)^2}\,(M_1^2-1)^3 + O(M^2-1)^4 \qquad (2.7)$$

This relationship shows that the entropy generation is roughly dependent on the $(M_1^2 - 1)^3$. Such small values of entropy rise across a weak shock will reduce further in the case of oblique shock waves, since in this case, the entropy rise is a function of the Mach number normal to the shock wave. However, in the trailing-edge region, high Mach numbers can exist which lead to the formation of additional shocks at the junction of the pressure and suction side flow.

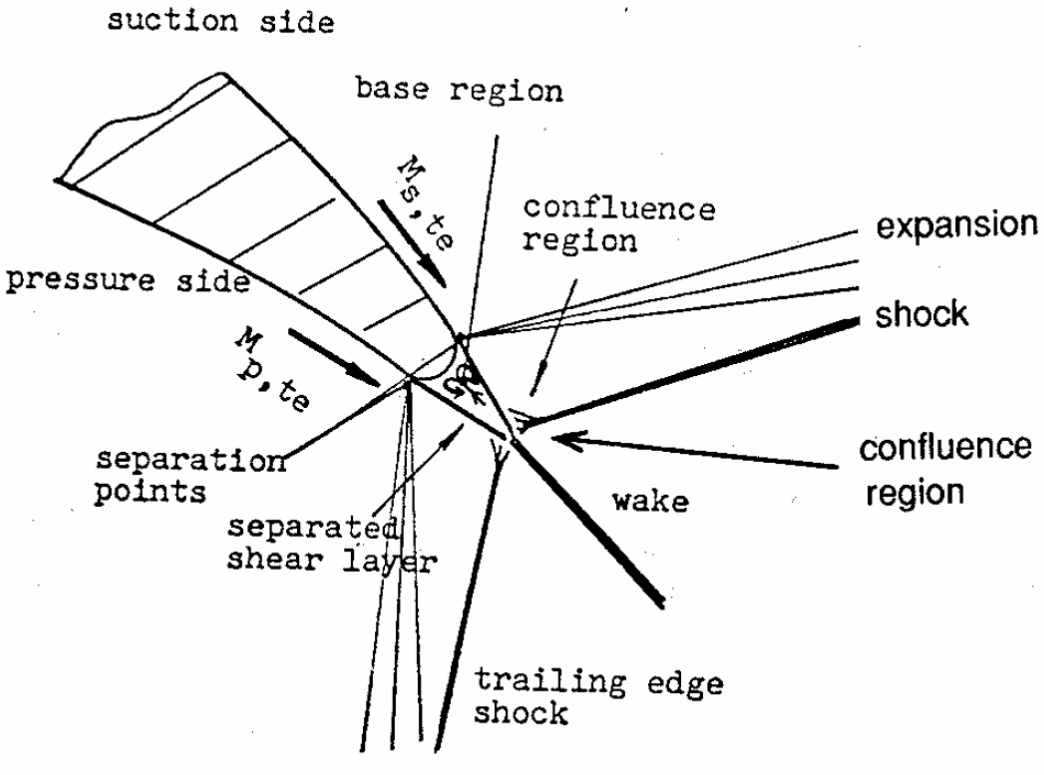

FIGURE 2.3. SHOCK STRUCTURE FORMATION FOR SUPERSONIC TRAILING EDGE FLOW, (DENTON AND XU, 1998)

(Denton and Xu, 1998) elaborate on the structure of the flow regime behind the blade trailing edges (see Figure 2.3). Immediately downstream of the blade trailing edge, forms a small triangular region of approximately uniform pressure, which is termed as the 'base region'. Shear layers surround this region where the velocity rises rapidly up to the freestream value. At the separation point of shear layers, the flow expansion waves are created due to the change in flow direction. A region of confluence is formed when suction and pressure side streams meet. Here, the flow changes its direction and can generate shock waves if the flow is supersonic. Such shock waves, formed due to the turning of the pressure and suction side flow streams, are referred to as trailing-edge shocks. As will be depicted within the results chapters, the pressure side arm of the trailing edge shock interacts with the suction side of the adjacent blade; while the suction side arm (usually slightly stronger) travels through the diffuser. As the blade rotates, the suction side arm of the trailing edge shocks forms a moving pressure field in the diffuser region. Trailing-edge shocks, depending on the blade stagger angles, can impinge on the neighbouring blade suction surface. As discussed above, such interactions, often seen near the tip side flow of the rotor blades, can lead to increases in the boundary layer thickness causing increase in the suction surface loss (Babinsky and Harvey 2014).

2.2.1.3 Mixing loss

Mixing loss occurs when two flow regimes mix together creating shear stresses between adjacent layers. Examples of mixing processes are wake flows, jet flows, boundary layer separations and reattachment flows. The amount of loss generated by the mixing of flows with differing velocities is proportional to the velocity difference squared.

In particular, at high Mach numbers the intense viscous dissipation immediately behind the trailing edge can generate considerable levels of entropy (Denton and Xu, 1998). (J. Denton, 1993) has demonstrated that local entropy generation due to mixing around the trailing edges can be quantified using a control volume approach. These values nearly match with the numerical predictions since they are based on the same conservation equations. However, the value of base pressure used in loss calculations significantly affects the predicted loss since these predictions are extremely sensitive to the value of this pressure. Also, the shape of trailing edge can affect the value of the base pressure. For example, (El-

Gendi, et al. n.d.) found that the trailing edge loss can be reduced by employing elliptic edges which can reduce the average base pressure by 5.26%. For the purpose of this thesis, the rotor trailing edges were kept circular in order to retain the original blade pressure distribution near its edges (see chapter 3 for detailed explanation).

R.J. Miller and J.D. Denton provided the review on the effects of varying static pressure field on the mixing loss (Miller and Denton 2012). They describe that when a shear layer (say a blade wake) is passing through a diffusing flow regime inside a diffuser, it undergoes a unfavourable streamwise pressure gradient due to which the transverse velocity gradient is increased. The change in the transverse velocity gradient occurs since "slow moving fluid resides in the favourable pressure gradient for longer than the fast moving fluid causing the slower fluid to have a larger increase in velocity". The entropy generation rate inside a shear layer is proportional to the square of transverse velocity gradient (J. Denton, 1993), thereby increasing the entropy creation in a diffuser and thus mixing loss will increase.

2.2.2 Three-dimensional loss mechanisms

The three-dimensional loss mechanisms can be roughly divided into three categories.

- End wall loss: Forms due to the presence of endwall boundary layers producing a range of vortices including passage vortex, corner vortex, scraping vortex (Sieverding 1985). The primary mechanism driving the endwall loss is the presence of the cross passage pressure gradient near the walls. It should be noted that the passage vortex forms when the incoming endwall boundary layer hits the blade leading edge forming a famous horseshoe vortex profiles. The two arms of this vortex are present on the either side of the blade surfaces near the leading edge. As flow moves downstream along the blade passage, the pressure side arm of the passage vortex along the endwall fluid within the endwall boundary layer starts to move from pressure to suction side of the blade and eventually rolls-up near the suction side forming a passage vortex (labelled as 'PV' in Figure 2.4). This flow field near the endwalls is highly three dimensional and at times interferes with the blade flow, in particular the suction side flow in the high hub/tip ratio turbines. The last stage of a low pressure turbine has a low value of hub/tip ratio yielding a relatively small influence of the endwall loss. Recently, (Denton and Pullan, 2012) gave the computational investigation of the

various sources of the endwall loss generation in a turbine cascade flows. They highlighted that a mixing interface between the stator and rotor might not represent the true rotor inlet flow near the walls. For this study, a pitchwise uniform inlet boundary condition to the rotor is assumed.

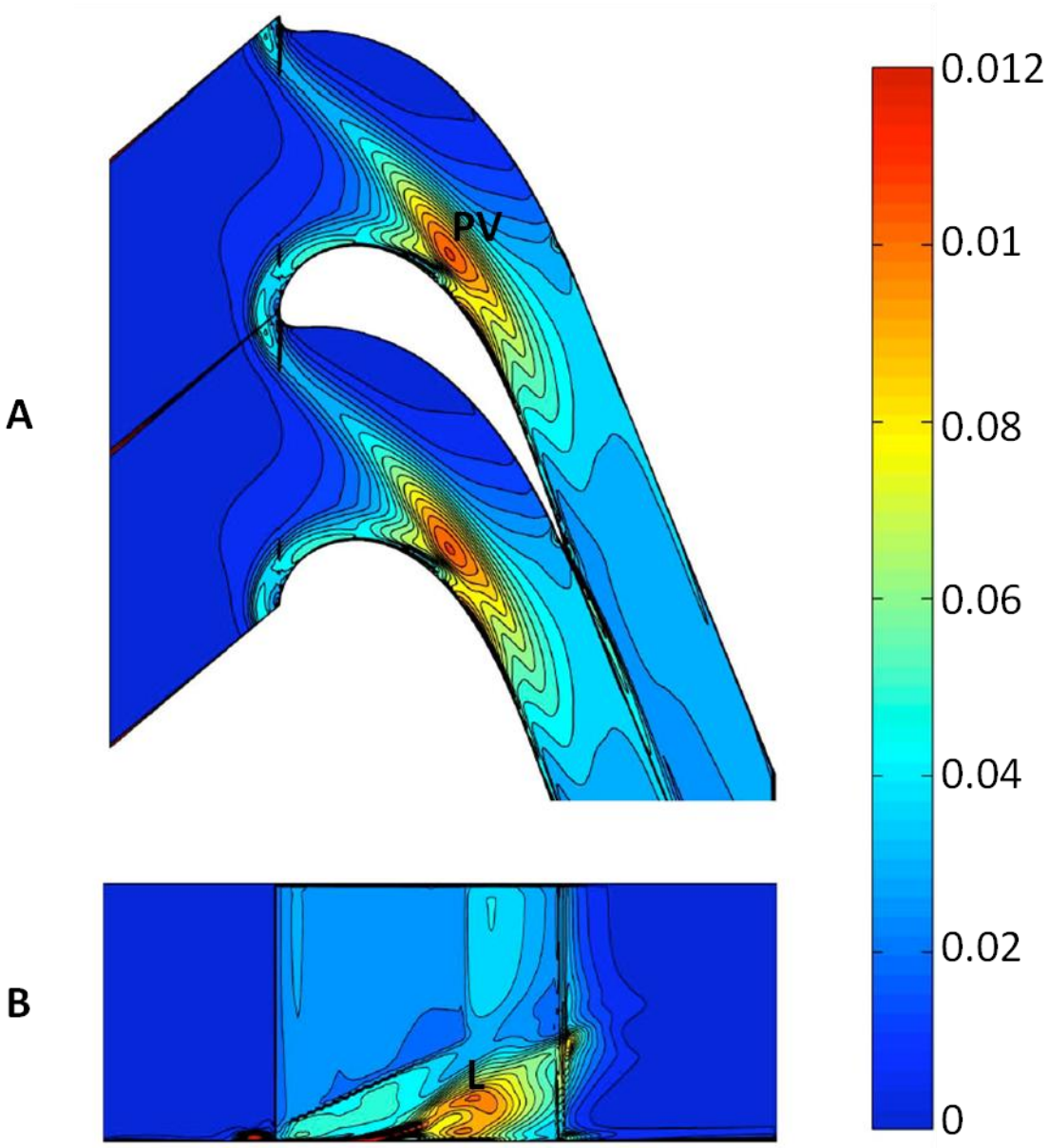

FIGURE 2.4. (A) DIMENSIONLESS ENTROPY GENERATION RATE PER UNIT SURFACE AREA ON THE ENDWALL AND ON THE SUCTION SURFACE FOR A TURBINE BLADE ROW. (B) TANGENTIAL PROJECTION OF THE BLADE SUCTION SURFACE. (DENTON AND PULLAN, 2012)

- Profile loss: The boundary layer on the blade surfaces is typically three-dimensional. The presence of the large flow variations from hub to tip gives rise to variable size

and nature of flow along the blade boundary layer. Figure 2.4 illustrates the typical three-dimensional nature of the boundary layer (labelled as 'L') on the blade suction surface. Here, secondary flow influences the blade boundary layer that increases the entropy generation on the blade surfaces.

- Tip leakage loss: The pressure difference between the suction and pressure side of the unshrouded rotor tip gaps produces a leakage flow that eventually rolls into a vortex and is responsible for an increase in mixing loss (Figure 2.5). Since, the tip leakage loss is essential to this thesis, the following section explores tip-leakage flows in more detail.

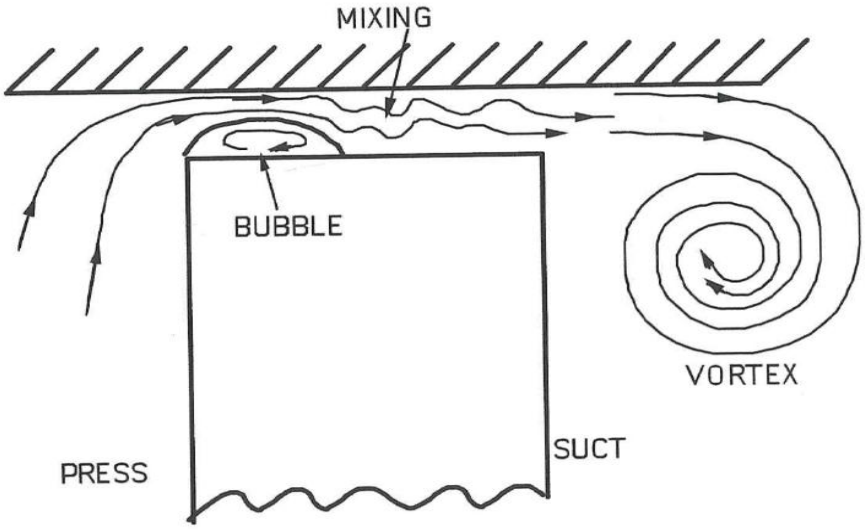

FIGURE 2.5. ILLUSTRATION OF THE TIP LEAKAGE FLOW OVER AN UNSHROUDED BLADE (J. DENTON, 1993)

2.2.2.1 Tip leakage loss

The presence of a gap between last stage rotor and the casing is inevitable due to the relative motion between the rotor and casing. This leads to a tip leakage (sometimes referred to as over tip leakage) flow, which can have a significant effect on the performance of the LSB-diffuser interactions. Figure 2.5 depicts a typical tip leakage flow for an unshrouded turbine blade where a high pressure fluid leaks over the tip gap and eventually is ejected out on the suction side. The mass flow rate of the leakage flow is dependent on the size of separation bubble that forms a vena contracta. Once this leakage flow leaves the tip gap, it is eventually pushed down by the unfavourable pressure gradient and rolls-down into a leakage vortex. It can be associated with a direct reduction in work output since the energy of the leakage jet remains unutilized (thus offloading the rotor tip). After ejecting out of the

tip gap, the leakage flow starts to mix with the main flow which becomes a major source of loss. Thus, the formation of a leakage flow is essentially an inviscid phenomenon, however, the loss production can be attributed to the viscous effects of flow mixing.

The change in blade loading, due to the presence of a tip leakage flow, changes the radial loading distribution to which a blade was originally designed. The primary literature on the tip leakage flow interactions with the endwall boundary layer is either described based on the tip gap geometry or the relative motion between casing and the blade tip. (Peacock, 1982) described that the casing side boundary layer flow affects the tip region performance by enhancing the formation of a secondary distributed vorticity. The secondary vortex (formed in a similar manner as cross-passage vortex) gets locked in the region of the interface between the blade suction surface and the annulus wall, resulting in a three-dimensional separation contributing to the loss of efficiency. Further, the presence of a relative motion between the blade and the casing side endwall boundary layer encourages a jet flow through the gap. This flow is in opposite direction to the leakage flow emerging out of the tip gap and thus forms a scrapping vortex at the junction of leakage flow interacting with the casing side passage flow (Peacock, 1983). (Blanco, Hodson and Vazquez 2009) performed the experimental cascade study where they injected a leakage flow from a cavity into the mainstream endwall flow for low pressure turbine blades and thereby simulating near casing interactions. They found that leakage strongly modifies the endwall flow structure while its interactions were independent of the leakage mass flow rate and tangential velocity.

The strength of the jet emerging out of a tip gap depends mainly on the height, width, blade passage configuration and flow conditions on the pressure and suction side of the tip gap. (J. Denton, 1993) provides a control volume flow approach to model a generalised loss in the blade row efficiency caused by a leakage flow in an unshrouded LSB:

$$\varsigma = \frac{2C_d}{\cos\beta_2}\left(\frac{g}{h}\right)\left(\frac{c}{s}\right)\int_0^1 \left(\frac{V_s}{V_2}\right)^3 \left(1-\frac{V_p}{V_s}\right)\left[1-\frac{V_p}{V_s}\right]^{1/2}\frac{dz}{c} \qquad \textbf{(2.8)}$$

where V_p and V_s are pressure and suction surface velocities, (g/h) is relative gap height, (s/c) is pitch to chord ratio and C_d is the discharge coefficient dependent on the size of separation bubble (see Figure 2.5). The above equation shows that C_d remains a big source of loss, and can be significantly affected by tip shapes which modify the blockage and hence

over-tip mass flow rates as studied extensively in the industrial gas turbines by (Krishnababu, et al. 2009a) and (Krishnababu, et al. 2009b).

The interaction of a leakage jet with the boundary layer of the diffuser lip can have a positive influence on the overall performance. For instance, (Musch, Stuer and Hermle, 2011) optimised diffuser performance/stage efficiency against lip shape and blade flow exit angles. This improvement occurred in the presence of a tip leakage flow due to the reduction in unfavourable pressure gradient experienced by the flow along the diffuser casing. Here, the working phenomena can be described using a Coanda-effect which causes a high energy jet to keep attached along a surface even when the surface is highly curved and offers a unfavourable pressure gradient (Volkmer, et al. 2012). This effect occurs due to the turbulent momentum exchange of the leakage flow jet and the casing side boundary layer. Thus a leakage flow delays flow separations on the diffuser casing. Recently various researchers have exploited this effect in order to operate their diffuser at a higher pressure ratio (Becker, Gretschel and Casey 2005), (Babu, et al. 2011), (Goudkov, et al. 2014), (Finzel, et al. 2011), (Hirschmann, Volkmer, et al. 2012), (Li, et al., 2012) and (Li, Li and Feng 2013). However, the existence of a high curvature and fast moving leakage flow jet can induce formation of shock waves on the diffuser casing. (Maier and Wachter 1988) constructed an experimental investigation of the oscillations produced by the shock-boundary layer interactions on the steam turbine diffuser casing. They demonstrated that such oscillations can be detrimental to the last stage and diffuser performance. They also established that an unsteady diffuser flow was not connected with the particular type of flow field, but was largely connected with the tip leakage flow.

(Rosic, 2006) studied shroud leakages in a low-speed three-stage turbine model and found that geometric complexities had a significant influence on performance. A similar study was performed by (Mahle and Schmierer 2011) in order to include further complexity of the gas turbine shroud geometry in order to study the interactions between the leakage flow and the primary blade path flow. These studies show that a detailed knowledge of the flow field and geometrical intricacies is necessary to accurately predict the loss generation by a leakage flow. Modifications to the casing shape can change the leakage jet, and its interaction in the diffuser, as shown by (Musch, Sievert, et al. 2009). They analysed different shroud and casing side shapes, on both rotor inlet and outlet side, to assess the major sources of the loss. This study revealed that casing shape on the rotor inlet was less

sensitive to the overall performance and a continuous rotor casing profile attached with the diffuser casing profile gave better diffuser pressure recovery. Further, (Jung, et al. 2012) analysed the effects of non-uniform tip clearance profile on the performance and flow field in a centrifugal compressor. They concluded that the blade passage vortex interacts differently with the leakage vortex due to non-uniform tip clearance that yields a modified blade exit pressure distribution. This effect enhances the downstream diffuser pressure recovery by keeping it attached for the longer duration.

In general, a leakage flow passing through a tip goes through a drop in relative stagnation pressure. However, it is possible that a turbine blade can do an effective work on the leakage flow due to the unsteady pressure field generated by the moving rotor blade. (Thorpe, et al. 2007) analysed such flows using both experimental and numerical studies and found increased stagnation enthalpy within tip leakage flow, that yields high absolute stagnation temperature and pressures, which gave rise to the over-tip casing heat transfer. (Yoon, Selmeier, et al. 2014) analysed a similar effect for the compressor hub leakage flows. They highlighted the difference in the conventional loss coefficients (that consider only pressure loss) and the actual loss predicted by CFD, thereby stressing on the importance of the additional energy transferred to the leakage flow due to the presence of a unsteady pressure field inside the tip gaps. The present study will explore a similar mechanism that occurs near casing region for the last stage blade within chapter 5.

2.3. Axial-radial diffuser design and flow features

The diffuser performance can be assessed (Hirschmann, Volker, et al. 2012) by determining the contributions of the stagnation pressure loss (Y_s) and blockage (ζ) to the diffuser pressure rise coefficient (CP), as indicated by:

$$CP = \frac{P_{out} - P_{in}}{P_{o,in} - P_{in}} = \left(1 - \frac{P_{o,out} - P_{out}}{P_{o,in} - P_{in}}\right) - \left(\frac{P_{o,in} - P_{o,out}}{P_{o,in} - P_{in}}\right) \qquad \textbf{(2.9)}$$
$$= (1 - \zeta) - Y_s$$

where total pressure loss (Y_s) gives the sum of stagnation pressure loss due to viscous effects (mixing/shearing) and non-equilibrium processes (shocks) within the diffuser flow; and inviscid loading (1-ζ) is a measure of blockage produced by processes such as boundary

layer separation, where ζ is essentially the ratio of exit to inlet kinetic energy (only approximate for compressible flows). The relationship shows that, for a given area-ratio, Y_s has a direct negative effect on the pressure recovery capability of the diffuser; for a fixed exit static pressure, this can be understood by considering total pressure losses in the diffuser as having a back-pressuring effect on the stage, requiring a higher diffuser inlet total pressure in order to overcome the momentum lost through viscous effects in the diffuser.

The last stage rotor exit flow conditions are generally non-uniform in both radial and circumferential directions (Senoo, 2012), but most of the studies have focussed on swirl and tip leakage jets at the inlet of the diffuser such as(Volkmer, et al. 2012) or (Babu, et al. 2011). In the past, higher swirl has shown improvements in CP for conical diffusers (McDonald, Fox and Dewoestine 1971) which is studied further by (Japikse and Baines 1998).

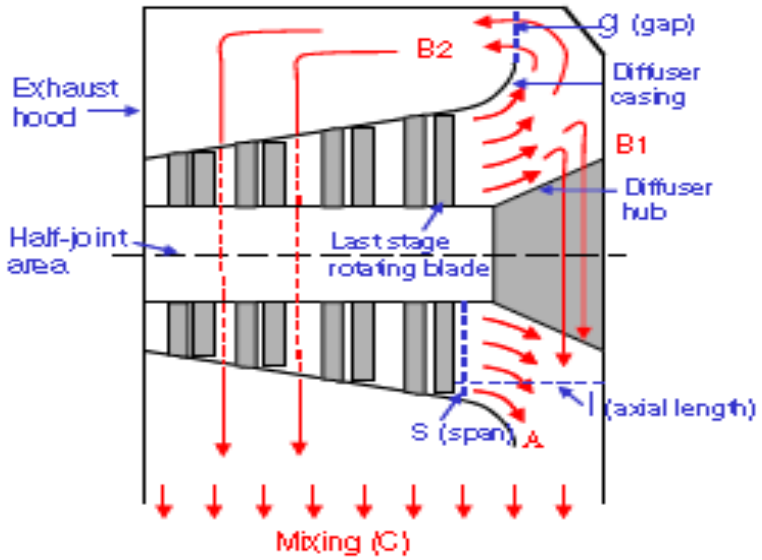

FIGURE 2.6. GENERAL FLOW STRUCTURE IN THE EXHAUST HOOD (YOON, STANISLAUS, ET AL. 2011)

Early fundamental investigations of diffuser flows were carried out by(Sovran and Klomp 1967). They investigated the performance of an annular diffuser and compared their results with previously published data. They showed that with the appropriate selection of non-dimensional length for all cases, the optimal geometry lines for different diffuser types have a significant degree of similarity. They tested different turbulent inlet boundary layer profiles and noticed that increasing boundary-layer thickness leads to a reduction in the pressure recovery due to early separation of the flow. Furthermore, they developed a

correlation based on the area blockage due to velocity non-uniformities over the cross-section was developed. Such mappings for lab based diffuser geometries were later catalogued by (Japikse and Baines 1998).

The performance of a diffuser is linked to the flow boundary condition at the inlet, separation of the flow at walls and unsteadiness. Since these factors are dependent on rotor flow features such as tip leakage jets and wakes, the diffuser pressure recovery (CP) is likely to have a high dependency on these features. This in-turn affects the exit conditions at the rotor because of low pressure recovery in the diffuser forming a highly coupled system.

(Stastny, Kolar and Tucek, 1997) described the three-dimensional flow field inside the steam turbine diffuser which was connected to a non-axisymmetric exhaust hood. The presence of three-dimensional flow field at the diffuser exit gave rise to the two counter rotating vortices within the exhaust hood flow (located on the outside periphery of the diffuser). These vortices, much like a horse-shoe vortex around a blade leading edge, influenced the majority of the diffuser exit side and collector hood flow field. (Stastny, Tajc, et al. 2000) continued this study by analysing the effects of the diffuser inlet swirl on the exhaust hood flow field comparing different RANS turbulence models with experimental findings. Figure 2.6 illustrates the general axial-radial flow in the diffuser. In the lower part of the diffuser, the flow leaving the rotor is turned through 90deg before exiting the hood (path A). In the upper part of the diffuser, the flow is first turned through the diffuser, moves radially outwards, and then spills circumferentially and axially (paths B1 and B2). The flow B2 further splits into two counter-rotating vortices, each located on the either side of the turbine-diffuser casing line. Finally, flow paths A, B1 and B2 meet near the exhaust hood exit where they mix with each other. Thus, forming a highly three-dimensional flow inside the diffuser.

Although the industrial diffuser design can be iterative, it is usually divided into three steps depending on the design stage:

- Streamline curvature calculation of axisymmetric flows using throughflow and boundary layer methods: A throughflow method in conjunction with various boundary layer solvers can provide a useful initial flow path design. Throughflow calculations coupled with spanwise mixing models (due to both secondary flows (Adkins and Smiths 1981) and turbulence (Gallimore and Cumpsty, 1986)) as cited by (Huntsman, Denton and Dawes 2004) have been achieved for various

turbomachinery applications. They further cited that (Lewis 1990) developed throughflow methods on turbines based on secondary flows and turbulence. Further, (Gallimore, 1997) developed a more sophisticated throughflow approach known as 'viscous throughflow' where entropy generation on the end walls is modelled together with the secondary flow and tip leakage losses near endwalls. But a throughflow method lacks the ability to predict flow behaviour after flow separations and the solution convergence is highly dependent on the scale of relaxation factors. Successful throughflow methods tend to rely heavily on empiricism. Despite its inherent limitations, an optimisation of the diffuser lip using this method may be very fast (if not accurate) and can reduce efforts in more complex design stages.

- Single blade pitch axisymmetric stage calculations using 3D-RANS: This step is the most common start for the diffuser partly due to availability of existing geometries and partly because of increased computing power. (Kreitmeier and Greim 2003) describes that a system is simulated using single stator and rotor passages (typically interfaced with a mixing-plane) and a sector of the diffuser and exhaust hood. This allows for the detailed blade geometry and endwall shape to be simulated, although the fully 3D exhaust hood geometry is not captured. By conducting stage calculations over a range of operating conditions, a performance database can be established. This step can help to improve the diffuser lip/hub shapes, at the same time blade tip leakage, blade wakes, splitters modelling can be performed to yield more accurate models. A similar approach is taken in Chapter 3 to generate diffuser designs employed throughout this thesis.

- Full annulus/exhaust hood calculations with 3D-RANS/U-RANS: Industry designers usually go one step further in order to include geometrical intricacies within the diffuser and its exhaust hood. One such proprietary technique is described (Kreitmeier and Greim 2003) and later employed by (Yoon, Stanislaus, et al. 2011), is known as Exhaust Design System (EDS). In this technique, the full exhaust downstream of the last stage blades is modelled. To begin with, a circumferentially uniform inlet boundary condition can be applied. After the first calculation, the inlet boundary conditions are updated based on the flow characteristics at the coupling plane. In order to capture the circumferential variation at the exhaust inlet (downstream of the blade trailing edge), the exhaust inlet boundary plane as well as

the coupling plane is segmented into over a hundred smaller circumferential pieces and each segment's flow properties are updated after each iteration. By iterating this procedure several times, a realistic asymmetric inlet boundary condition can be produced. However, sometimes such methods may disregard important flow features such as blade wakes, unsteady flow effects and wetness effects in order to gain robustness in their design process.

Recent advancements demonstrated that Non Linear Harmonics (NLH) method developed by (He and Ning 1998) can be used to model flow interactions between last stage blades and fully three-dimensional non-axisymmetric exhaust diffuser (Burton, Z.; Ingram, G.; Hogg, S. 2013). They showed that increases in the computational costs using this method were about seven times the quasi-steady numerical simulations. Such an increase in the computational cost is very small as compared to the expected simulation time required for the full three-dimensional unsteady flow interactions.

(Musch, Stuer and Hermle, 2011) have applied the use of step 1 (throughflow methods) to optimise the diffuser lip in conjunction with the tip leakage jets and blade exit flow angles where new diffuser area ratio was expanded by 20%. This led to the improvement in 4% stage efficiency, 10% increase in diffuser pressure recovery and 50% reduction in the leaving losses at the diffuser exit. (Tanuma, Sasao, et al., 2011) carried out compressible Navier-Stokes calculations using high-order high-resolution finite-difference method including the wet steam condensation model. The study concluded that inlet turbulence intensity just downstream of the turbine stages is necessary for the numerical analyses of the turbine diffusers. But in order to avoid high computational costs, the simulations were performed for only one quarter section of the diffuser annulus and without asymmetric boundary conditions at the diffuser inlet.

(Greitzer, Tan and Graf 2004) discuss the effect of flow non-uniformity in simple axial (annular) diffusers. In this analysis, they categorised the flow regime into boundary layer flow and core flow (flow outside the boundary layer). They established that the distortions due to pressure forces on core velocity non-uniformity can reduce diffuser CP relative to the uniform core flow. Further, the influence of viscous forces in transferring momentum to low velocity streams tends to mitigate the effect of pressure forces and, for longer diffusers, pressure recovery can be enhanced. Since the analysis was not performed for the axial-radial

diffusers, it cannot be simply assumed that the results will apply for steam-turbine diffuser, especially when a diffuser encounters the complex flow environment of wakes, leakage vortices and 3D non-uniformity in the flow.

(Stastny, Kolar and Tucek, 1997) demonstrated (by CFD calculations on a full exhaust hood) that the flow structure in the axisymmetric diffuser changes considerably when compared with uniform inlet velocity profile. Flow separations were observed at the inner diffuser walls at the exit. They also showed the occurrence of a vortex in a horseshoe shape between the outer periphery of the diffuser and exhaust hood. This vortex formation is due to the combined effect of velocity non-uniformities and the exhaust hood shape (also shown by Liu & Hynes, (2002b)).

One of the first extensive works on LSB-asymmetric exhaust hood interactions (with axial-radial diffuser) was done by (Liu, Cui and Jiang 2001). Full exhaust hood (Inlet/exit) boundary conditions were analysed both experimentally and numerically by employing Actuator Disc Theory (ADT). It was asserted that the flow pattern and hood performance were different with or without turbine exit flow conditions simulated. The overall pressure recovery was mainly achieved inside the diffuser and the diffuser performance was strongly influenced by the inflow/outflow conditions. The ADT method is generally fast in numerical modelling of the LSB by directly jumping to LSB exit by achieving required flow turning and entropy rise, but it cannot determine LSB choking, tip leakages, blade wakes and possibly unsteady effects.

As mentioned earlier, (Burton, Ingram and Hogg, 2013) employed the usage of non-linear harmonics to accurately transfer circumferential asymmetries in both directions for last stage blades and exhaust diffuser. Using the same method, (Burton, Hogg and Ingram, 2013b) analysed the effects of diffuser inlet asymmetries on the diffuser exhaust hood performance. When compared against the conventional mixing plane approach, they found that the flow structure was considerably different when flow coupling is simulated. However, they found a little change in the diffuser pressure recovery between these cases.

Liu & Hynes, (2002a,b and 2003) covered different exhaust hood geometries and flow conditions to understand non-axisymmetric flows. Initially, the non-axisymmetric nature of the flow due to the exhaust hood geometry was established. The non-axisymmetric of the flow reduced the diffuser performance and pressure recovery. By comparing two different hood geometries, it was concluded that modifying the collector cross-section areas could be

used to improve the axisymmetric flow. Finally they discussed that spanwise (radial) variation of the flow conditions can generate different flow behaviours at hub and tip.

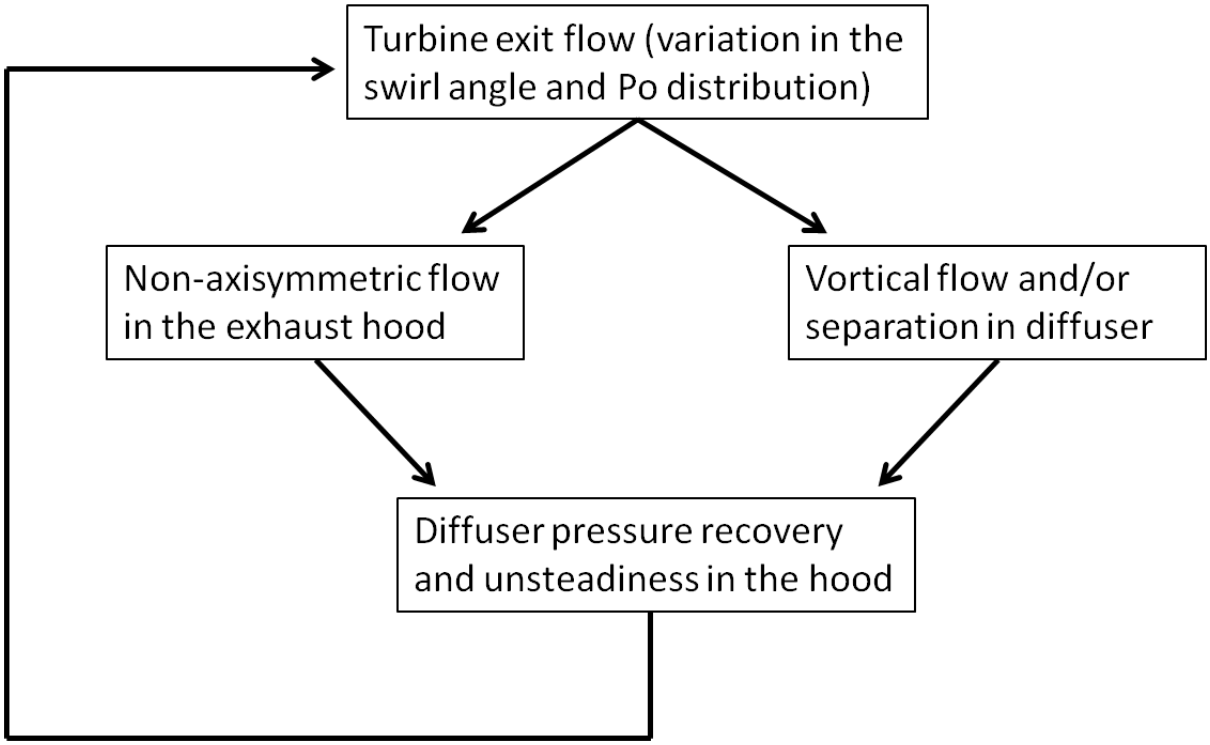

Figure 2.7. UNSTEADY FLOW INTERACTIONS BETWEEN TURBINE AND EXHAUST HOOD (Fu, Liu and Zhou 2012)

(Finzel, et al. 2011) experimentally investigated the effects of geometrical parameters on the pressure recovery of the exhaust hoods. Their findings suggested that allowance should be made for increasing area along the flow path length within the exhaust collector for sufficient diffusion levels in the diffuser. This change in area ratio (of exhaust hood to diffuser exit) was nearly independent of the diffuser geometry but the optimum value is linked with tip leakages from the last stage blades. As mentioned earlier in the tip leakage flow section, their study also demonstrated that increasing tip leakage Mach number helps to lower the blockage (ζ) while keeping the flow attached to the diffuser casing. (Bernier, Ricklick and Kapat 2011) conducted similar experimental and computational studies where they analysed various aspects ratios of the exhaust hood geometry. They revealed that the shape of the exhaust hood collector affects the diffuser flow structure and performance can reduce for tight exhaust hoods. (Mizumi, Ishibashi and Sawamura, 2012) conducted computation studies of the last stage turbine and asymmetric exhaust hood. They

demonstrated a 12% increase in the pressure recovery coefficient by using swirl separation ducts within the exhaust hood structure.

(Fu, Liu and Zhou 2012) provides an in-depth numerical and experimental study of unsteady interactions between LSB and an exhaust hood under different operation conditions. They explain that the flow interactions occur in both ways, i.e. effects of unsteady non-uniform flow at turbine exit on the exhaust hood aerodynamic performance and similarly, effects of unsteady non axisymmetric flow imposed by the exhaust hood on the aerodynamic performance of the turbine stage. Figure 2.7 depicts the interaction between LSB and exhaust hood as detailed by them. The flow field at the turbine exit affects the circumferential non-uniformity of the flow field in the exhaust hood and separations in the diffusers. Thereby this non-uniformity leads to low frequency fluctuations of flow parameters on the blade. Considerable amount of flow separations in the diffuser lowers its performance, which in-turn changes the turbine exit conditions (back pressure) due to lower recovery. Hence a strong coupling occurs between the LSB and diffuser.

2.4. Scope and gaps in the LSB literature

The literature review of the last stage blades within a low pressure steam turbine has been covered in the previous chapter. However as highlighted before, the exact mechanism of the coupling between the rotor blade and axial-radial diffuser downstream remains unknown. This is partially due to the fact that most of the research has focussed on the features of full annulus 3D diffuser and the exhaust hood present downstream. Furthermore, the literature review has been able to cover the effects of 3D diffuser shape changes on the last stage only. The literature has missed important aspects of supersonic flow and large loss generation at the rotor trailing edges that can affect the flow interactions as highlighted in the Figure 2.7. Such flow conditions can lead to presence of strong trailing edge shocks within the diffuser flow which will be highlighted in the chapter 4. As computational power increases, it is expected that exact changes within diffuser shape can be made via sophisticated shape optimization methods (for example by using evolutionary algorithms or Adjoint optimization methods). Industry has developed last stage-exhaust hood integrated design systems, multi-disciplinary workbenches have been included within major commercial CFD packages and coupling methods such as non-linear harmonics have been proving useful for the research purposes. With increasing design range, for example operating relative Mach number within last stage blades, a small geometrical change can

lead to large flow perturbations. However, much of the computational efforts can be minimized if the exact mechanism of the performance enhancement is known. It can be achieved by focussing on the flow features that are affecting the performance factors within generic designs. These features can include streamline curvature changes, flow non-uniformities, rotor overtip leakage flows, formation of shock waves within blade passages, trailing edges, diffuser passages, etc. By focussing on these features, a simple mapping of their dependence on system performance factors can be realized. Thus, the current project covers the process of differentiating flow features, studying them independently and then trying to map their effects across the design range of the machine.

2.5. Conclusions

The present chapter has outlined the current understanding of the flow features that are typical to a low pressure turbine rotor and the diffuser downstream that will be relevant to the computational study presented in the later chapters of this thesis. The performance of the last stage rotor in a low pressure steam turbine is highly linked to the pressure recovery capability of its diffuser. Since, the diffuser pressure recovery itself is dependent on the loss producing features, there remains much work to be performed on understanding how exactly these mechanisms affect the performance of the two components. The next chapter will elaborate on the methodology adopted in the present study.

3: Computational methods and flow solver validation

Chapter Outline:

This chapter discusses the flow solver used throughout the project. It will also explain the last stage configuration and diffuser design methods applied throughout the thesis. The chapter ends with a validation of the flow solver using data from an experimental test-rig obtained from the industrial collaborator.

3.1 Introduction

As highlighted in the previous chapter, most of the research has been focussed on the non-axisymmetric flow within the exhaust hood only. This has led to a gap in the parallel development of supersonic flow features within diffuser as compared to the last stage blades. While non-axisymmetric flow features affect the diffuser performance, it is these changes in the local flow at the exit of each blade row that affects the flow coupling highlighted in Figure 2.7. Thus, to understand these local flow structures only axisymmetric exhaust diffuser geometry was selected for the computational results shown in the subsequent chapters. The present chapter outlines the selected methodology to help understand the local flow characteristics such as trailing edge shocks, tip leakage flow, blade wakes, diffuser casing separation, etc.

3.2 Flow solver and turbulence model

The flow solver used in the present study is TBlock version 11.9, which is a 3D RANS solver developed by Prof. John Denton (Personal communication 2012) and is frequently used in industry for design purposes. It is a time marching method as described in (Denton, 1980). TBlock is a finite-volume multi-block structured grid solver that can solve both the steady and unsteady Reynolds-Averaged Navier-Stokes equations. Its time stepping is based on the explicit 'Scree' algorithm (based on Adams-Bashforth approach) that requires minimal artificial viscosity as shown below:

$$\Delta F = \{2\, dF/dt)^n - dF/dt)^{n-1}\}\, \Delta t \qquad \textbf{(3.1)}$$

where F is the flow property (i.e. ρ, ρV_x, ρV_r, $\rho r V_t$ or ρE) being solved for and n is the time step index. The spatial differences are completely centred and the solver uses cell corner storage method. A combination of first and second order smoothing is used to overcome issues related to odd-even decoupling. The maximum stable CFL limit for this algorithm is about 0.5 which is lower than other more complex algorithms such as five step Runge-Kutta scheme (Miller and Denton 2012). The algorithm is second order accurate in space and first order accurate in time.

For steady simulations, TBlock uses spatially varied explicit time stepping. For steady stage calculations, a mixing plane interface is implemented between blade rows; the mixing plane removes circumferential non-uniformities by circumferentially averaging the flow while conserving mass, momentum and energy.

The solver employs a multi-block approach by dividing the flow domain into various blocks of different sizes and shapes while joining them with different patches (as desired by the user). Three levels of multigrid were used for faster convergence of solutions in large sized blocks. The program follows the cylindrical coordinate system. This coordinate system greatly helps for turbomachinery applications since a tangential momentum equation can be replaced directly by a moment of momentum, thus accounting for the coriolis and centrifugal force components. The following nomenclature is adopted within the program: I-index corresponds to roughly the meridional direction, the J-index corresponds to the spanwise direction and the K-index corresponds to the circumferential/pitchwise direction. These indices will be used invariably throughout this thesis while referring to the flow directions and averaging planes.

In this thesis, periodicity was enforced in the diffuser over a sector equal to the rotor pitch using periodic interfaces. Stage calculations were performed in order to obtain realistic inflow boundary-conditions for the rotor/diffuser calculations; for these cases, the stator and rotor were interfaced with a mixing plane. In order to simulate the rotor/diffuser interaction, Throughout this thesis, only axisymmetric diffusers have been simulated; the advantage of this is that the rotor and diffuser could be directly coupled with a contiguous interface, and the relative motion between rotor and diffuser was simulated by the relative motion imposed at the endwalls. (Musch, Stuer and Hermle, 2011) has found such configuration to be a good

choice in order to capture the flow features convecting downstream into the diffuser, without the need for interpolation across the rotor/diffuser interface which can lead to numerical dissipation of the rotor flow.

The turbulence is modelled using a Spalart-Allmaras (SA) model (Spalart and Allmaras 1994). Depending on the near wall mesh resolution, wall functions can be employed if the first grid-line away from the wall is outside of the viscous sub-layer (Denton and Pullan, 2012). For the calculations performed in this project, the first grid point away from the wall was positioned at $y^+<5$ for all viscous surfaces, and thus the viscous sub-layer was fully simulated. All solid surfaces are specified as adiabatic and boundary layers are set to fully turbulent for computations. In order to generate a realistic profile of turbulent viscosity in the boundary layer, a mixing length model was used for the first 10 grid points (streamwise direction) in the inlet block.. The most common type of turbulence models used for the present application are Spalart-Allmaras (SA), k-ϵ and k-ω turbulence models. A study by (Córdova and Stoffel 2006) and (Bhat and Sullerey 2013) found good agreement with experimental diffuser data using these models. (Burton, Ingram and Hogg 2013a) have summarised the usage of various turbulence models for last stage and exhaust hood studies. However, it must be acknowledged that no single method can fully resolve all the types of flow being encountered within turbomachinery flows and SA model implementation within TBlock is no exception to it. Nonetheless, TBlock has been successfully used in the past for many turbomachinery studies, such as shroud leakage modelling by (Rosic, Denton and Pullan 2006), hot streak migration studies by (Ong, Miller and Denton 2010) and endwall loss generation in cascade flows (Denton and Pullan, 2012).

3.3 Rotor configuration and meshing

The last stage blades geometry was obtained from Prof. John D. Denton (Denton, 2012). Here, the rotor hub-to-tip ratio was set at 0.426 where the rotor circumferential pitch is set at 0.143 Radian (44 blades in total) and it was set to rotate at 3000 rpm. The inlet boundary conditions for the rotor was specified as fixed stagnation pressure (0.2421Pa) and temperature (339K) along with the flow angles uniform across the rotor passage. The spanwise distribution of the inlet boundary conditions is given by Figure 3.1. The rotor blade of the typical last stage low pressure turbine is highly loading at its tip (see Figure 3.2) requiring very fine mesh to correctly capturing the trailing edge flow. Therefore, a rigorous meshing strategy was adopted throughout this study which is explained within this section.

Computational meshes were generated via a parametric program written in the MATLAB specifically for this study. The computational mesh was required to capture the flow accurately in the presence of long (low hub to tip ratio), thin and highly twisted blades. The mesh topology was based around an multi-block H-O-H configuration. The following procedure was adopted to construct a parametric mesh using a program written in the MATLAB:

The blade geometry was imported and cubic splines were used to define the blade profiles. Any required modifications to the endwall shape are then applied. A new casing/hub line (if needed) is constructed from rotor inlet to rotor outlet in this step.

Once the blade geometry has been fixed by pre-conditioning routines, the computational space is divided into several blocks that satisfy O-H mesh topology. The spatial size of such blocks is fixed at this step, for example the rotor exit block is extended up to a distance of 5% blade chord. All grid points are adjusted within the fixed spatial dimension of each block. The computational domain is divided into 14 blocks (9-rotor, 3-diffuser and 2-rotor tip gap). Figure 3.3 provides the representational image of the blocking structure used within a blade passage. Block 1 is the inlet to the flow domain followed by a blade inlet block 2 and then blade exit block 3. Blocks 4-7 constitute an O mesh wrapped around the blade surfaces. Generally, these blocks are very thin such that high mesh resolution can be achieved inside the boundary layer regions. The width of blocks 4-7 are set by the blade surface normal vectors at a variable length. By varying the block width along the blade surfaces, the individual mesh cells can be refined at the high curvature regions such as leading and trailing edges. The usage of surface normal vectors ensures the absence of highly oblique cells near the blade surface especially when grid points are very close to each other in the high curvature regions. To capture primary flow passing through the blade passage with a sufficient resolution, blocks 8 and 9 were filled in-between boundary layer blocks.

Following blocking of the computational domain, the grid points are allocated along streamwise (I), spanwise (J) and pitchwise (K) directions. Appropriate levels of grid expansion ratios are applied in each direction. Also, in order to produce a good resolution near the thin and sharp rotor leading edges in blocks 4 and 6, the local grid expansion ratios are modified in the streamwise direction. This step can be iterative when a new geometry is

being introduced, however the author has spent considerable time to ensure a good resolution near the sharp edges of the twisted rotor blades.

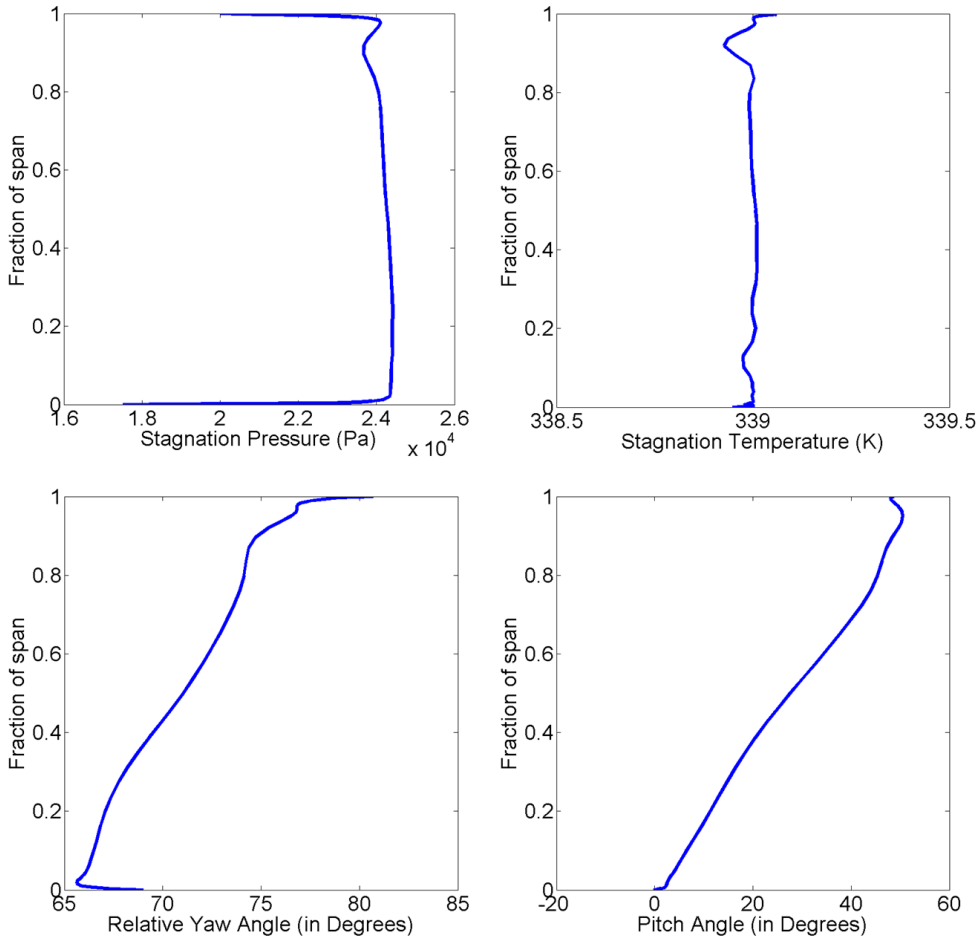

FIGURE 3.1. INLET BOUNDARY CONDITIONS TO ROTOR FLOW DOMAIN

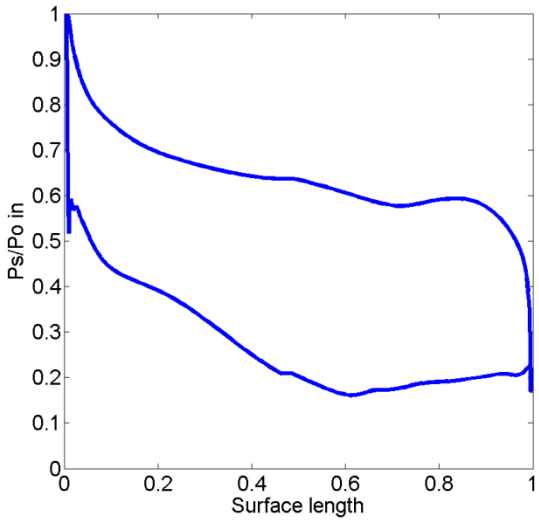

FIGURE 3.2. TYPICAL STATIC PRESSURE DISTRIBUTION AROUND ROTOR BLADE NEAR ITS TIP INDICATING PRESENCE OF HIGH LOADING CONDITIONS

The rotor inlet boundary conditions are fed from a previously converged stage (stator-rotor) solution with the datum geometry. These conditions remain fixed throughout the project. Table 1 gives the number of grid points for both rotor and diffuser blocks. The total number of grid points are over 3.5M. The optimal block mesh sizes were obtained from the mesh independence study that will be described later in this section.

The grid points on each block interface are contiguous to ensure no loss of information while transformation of fluxes from one block to another. Within blocks 8 and 9, a small degree of Laplacian smoothing of hexagonal grid was provided to ensure smooth transition of grid aspect ratios and maintaining near orthogonal cells for the mesh regions away from the walls. Smoothing of the cells is important as rotor blades are highly twisted and thus considerably bend the blocks 8 and 9 along with them.

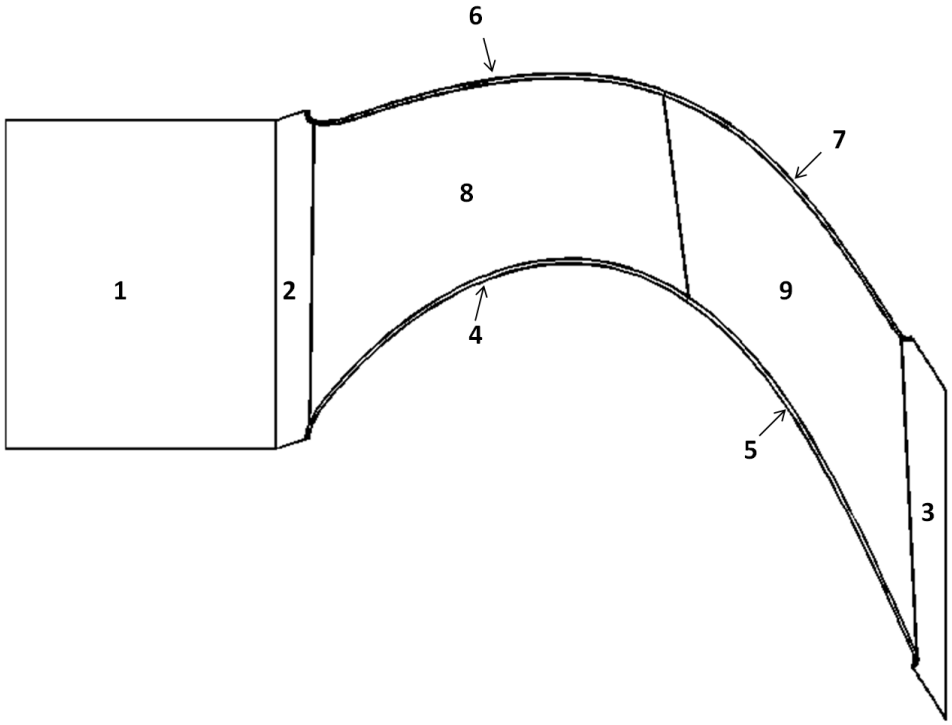

FIGURE 3.3. COMPUTATIONAL DOMAIN BLOCK TOPOLOGY WITHIN A BLADE PASSAGE

Figure 3.4 provides different views of the computational mesh. Part A shows the mesh for the whole domain as seen in the meridional plane. Part B depicts the mesh on the rotor surfaces as viewed at an oblique angle from the top. Part C gives the zoomed-in view of the mesh around rotor trailing edges. Part D shows the computational mesh for the rotor tip gap.

Appropriate level of grid expansion ratios are applied such that smooth transition of cell aspect ratios occurs across the computational domain.

The tip gap is specified as a flat tip and its blocks, 13 and 14, are modeled with an H-grid (see Figure 3.4). The hub surfaces are rotating along with the computational domain located inside the rotor passage blocks (2-9). By limiting the extension of blocks 2 and 3 up to 5% of blade chord (refer to Figure 3.3 and Figure 3.4), the rotational motion of the rotor hub is kept within the rotor passage only.

Block Number	Block Type	Mesh Size (I*J*K)
1	Domain Inlet	60x98x82 = 482160
2	Rotor Inlet	35x98x82 = 281260
3	Rotor Exit	20x98x76 = 148960
4	Boundary layer suction surface front side	67x98x15 = 98490
5	Boundary layer suction surface aft side	65x98x15 = 95550
6	Boundary layer pressure surface front side	67x98x15 = 98490
7	Boundary layer pressure surface aft side	65x98x15 = 95550
8	Primary flow	56x98x60 = 329280
9	Primary flow	57x98x60 = 335160
10	Diffuser inlet	70x98x76 = 521360
11	Diffuser flow	70x98x76 = 521360
12	Diffuser exit	70x98x76 = 521360
13	Tip gap leading edge side	67x21x21 = 29547
14	Tip gap trailing edge side	65x21x21 = 28665

TABLE 1. BLOCK STRUCTURE AND MESH SIZE

Unless specified, all calculations in this thesis are performed using Spalart-Allmaras (SA) turbulence model. The specific heat capacity at constant pressure (c_p) for all calculations was kept fixed at 7365J/Kg.K while gas constant (γ) was fixed at 1.063. These

values correspond to match wet steam flow (Stuer H. 2005). Here, specific heat capacity at constant pressure (c_p) has been estimated from the rate of change of enthalpy with temperature along a specified expansion line while gas constant (γ) from the relationship $T \propto P^{(\gamma-1)/\gamma}$ along the same line (Havakechian and Denton, 2015). The values shown for the flow solver validation studies uses a value of γ obtained from the pressure:density ratio along a specified expansion line together with an average gas constant (R) obtained from the $P = \rho RT$ relationship (Private communication with Alstom Power, Rugby, UK 2012). (Havakechian and Denton, 2015) found that despite large difference in these values, the flow solver gives same results with a negligible difference in the power.

Grid Type	Grid Size	Relative Grid Size	Rotor η_{tt} (%)	Rotor η_{ts} (%)	Rotor Work Out (KJ/Kg)
Coarse	675220	1	93.893	78.367	177.964
Medium	1466640	2.172	93.931	78.333	178.107
Fine	3094000	4.582	94.059	78.464	178.372

TABLE 2. MESH INDEPENDENCE STUDY FOR ROTOR

Grid Type	Grid Size (IxJ)	Relative Grid Size	Diffuser CP (%)	Diffuser Ys (%)	Exit KE (KJ/Kg)
Coarse	36x65	1	24.518	2.631	35.426
Medium	60x98	2.513	25.217	2.677	35.477
Fine	106x172	7.791	25.383	2.583	35.302

Table 3. MESH INDEPENDENCE STUDY FOR DIFFUSER

To arrive at the optimal mesh size for each block (described in Table 1), a mesh independence study was performed separately for the rotor passage, diffuser and tip gap regions. Three sets of meshes were obtained (coarse, medium and fine) for each component. For the rotor, a short downstream diffuser (shown in Figure 3.5) was included in order to allow the flow to mix to some extent before passing through the exit domain, in order to improve convergence. Figure 3.5 shows that the predicted Mach number distribution is relatively insensitive to the choice of mesh density tested in this study. Figure 3.6 plots the

pitchwise averaged static pressure at the rotor exit for the three meshes considered. In the region of interest to this thesis near the casing, the ‘medium’ mesh appears to provide a suitably resolved prediction of the flow.

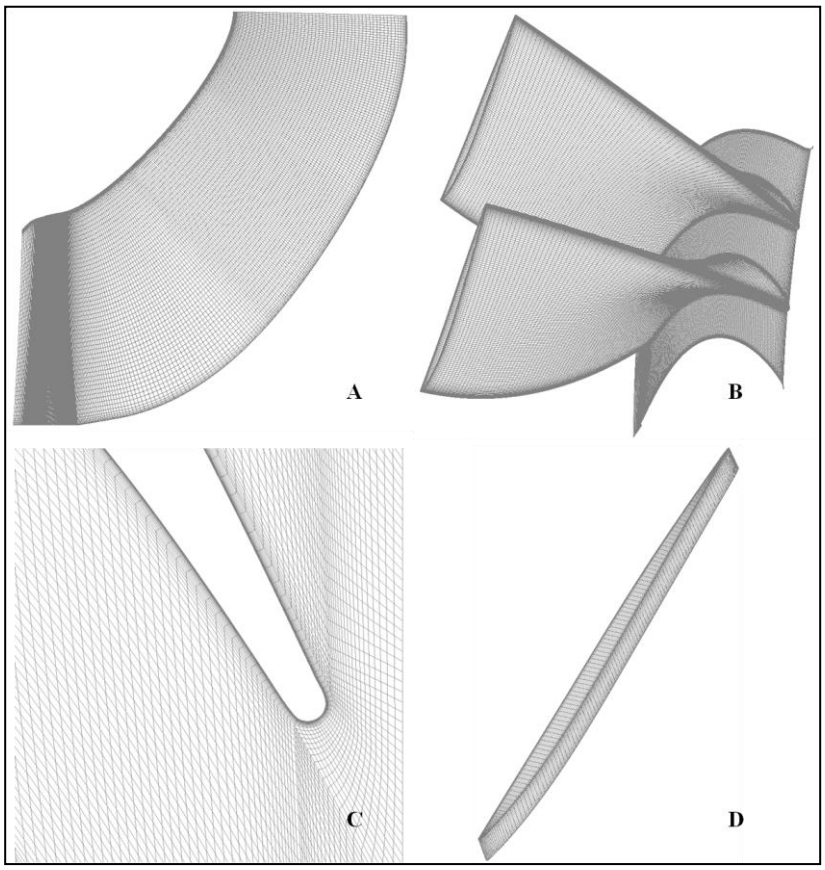

FIGURE 3.4. COMPUTATIONAL MESH USED FOR RESULTS SHOWN IN THE SUBSEQUENT CHAPTERS

Table 2 details the data obtained from results on rotor grid independence study. The number of grid points inside the rotor passage are slightly smaller since total grid size values also contains the grids within axial diffuser as well. The rotor performance factors, total-total efficiency, total-static efficiency and specific work output increase minutely across the three meshes. Thus, the medium mesh was found suitably accurate for the purposes of this thesis.

In order to determine the mesh resolution required for simulating the diffuser flow, a diffuser with an area ratio of 1.25 was constructed using the steps described in the next section. This diffuser was run in isolation using inlet boundary conditions derived from the rotor calculations. Table 3 provides the details of the meshes that were tested. Figure 3.7 plots the pitchwise averaged absolute Mach number in the diffuser. The prominent feature

appearing in this case is the presence of normal shocks near the diffuser casing, formed by the over-expansion of the supersonic flow leaving the rotor. The first shock is followed by further expansion of the flow which in turn produces a second shock located downstream. The near casing flow stays in the transonic region after passing through a second shock with fine mesh solution revealing subsequent smaller shocks. Figure 3.8 plots the normalized static pressure on the diffuser casing along its surface length. Here, all meshes predict the location of first casing shock close to each other. Thus comparing the three meshes, the medium mesh was found to be sufficiently resolving the flow features and one-dimensional performance factors.

Once both rotor and diffuser meshes were established a tip gap was introduced in the rotor-diffuser flow domain. The tip gap was tested with 10x10, 20x20 and 30x30 number of grid points in the spanwise (J) and pitchwise (K) directions. The grid expansion ratios were adjusted accordingly such that a smooth transition of mesh occurs at the rotor-tip junctions. S. The leakage mass flow through a tip gap was found to be 0.10439 Kg/s, 0.10456 Kg/s and 0.10467 Kg/s for coarse, medium and fine meshes respectively. Thus, the tip leakage flow appeared to be relatively insensitive to tip mesh resolution. The final mesh (shown in Figure 3.4) contains the rotor blocks well above their respective converged grid sizes.

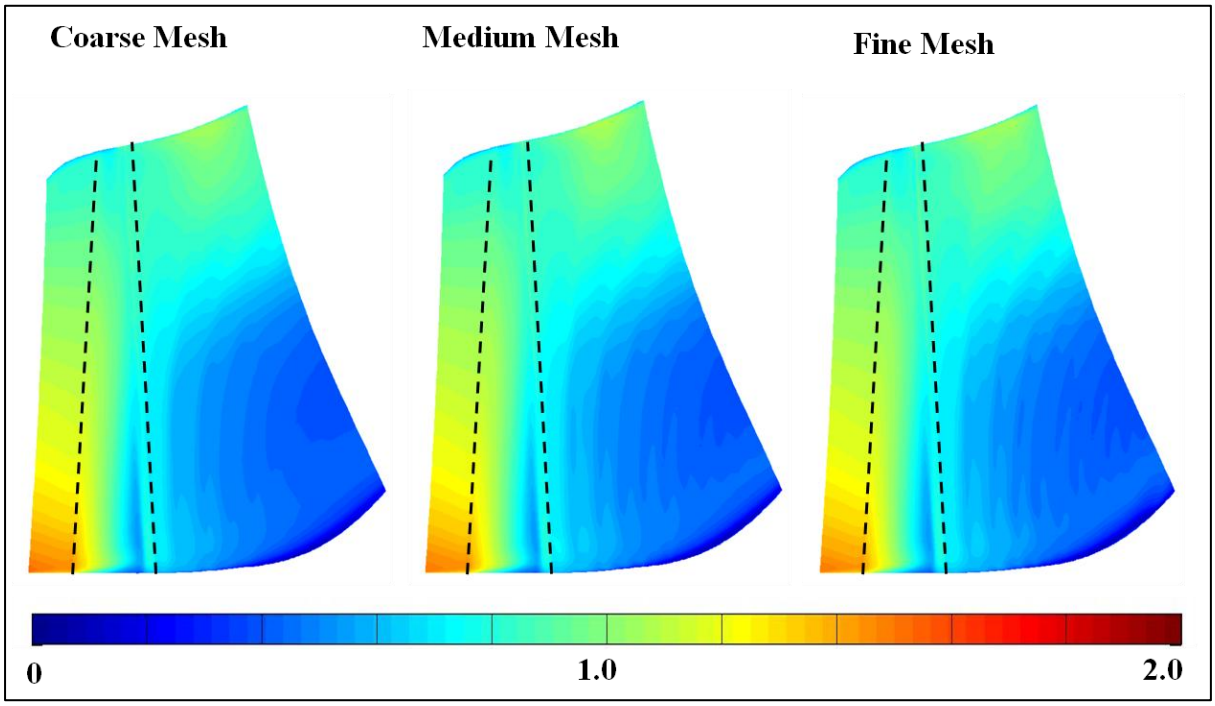

FIGURE 3.5. PITCHWISE AVERAGE ABSOLUTE MACH NUMBER CONTOURS FOR DIFFERENT ROTOR MESH SIZES

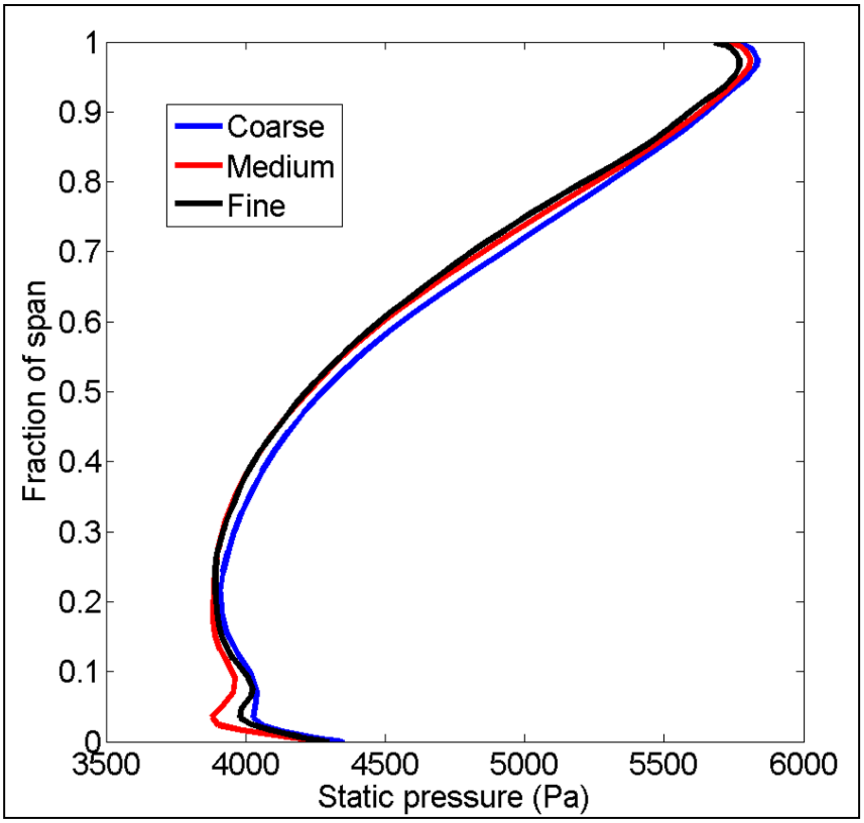

FIGURE 3.6. PITCHWISE AVERAGE ROTOR EXIT STATIC PRESSURE COMPARING DIFFERENT MESH SIZES

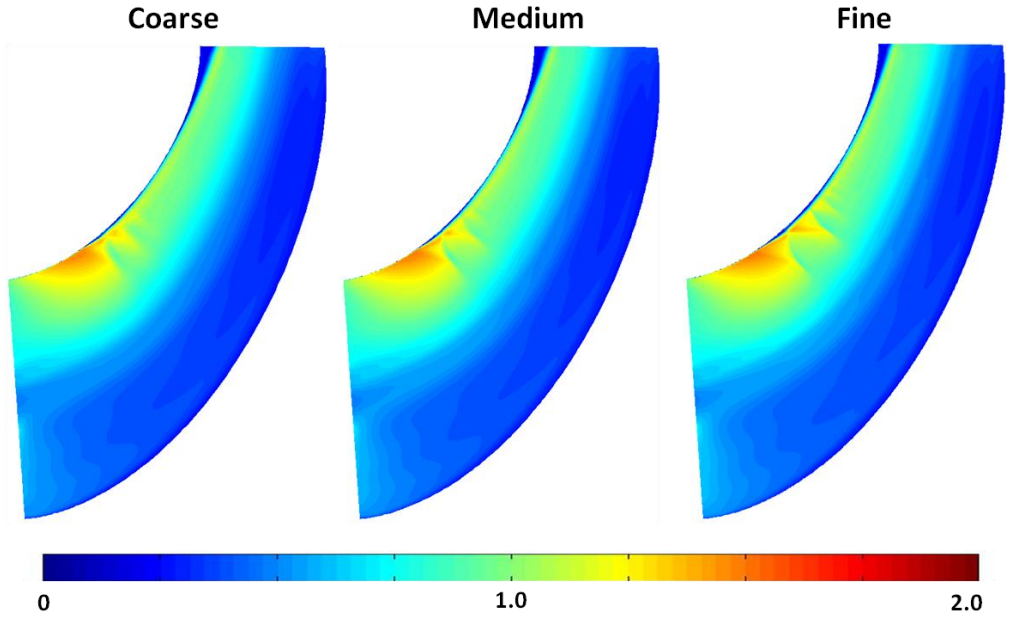

FIGURE 3.7. PITCHWISE AVERAGE ABSOLUTE MACH NUMBER CONTOURS COMPARING THREE DIFFERENT MESH SIZES

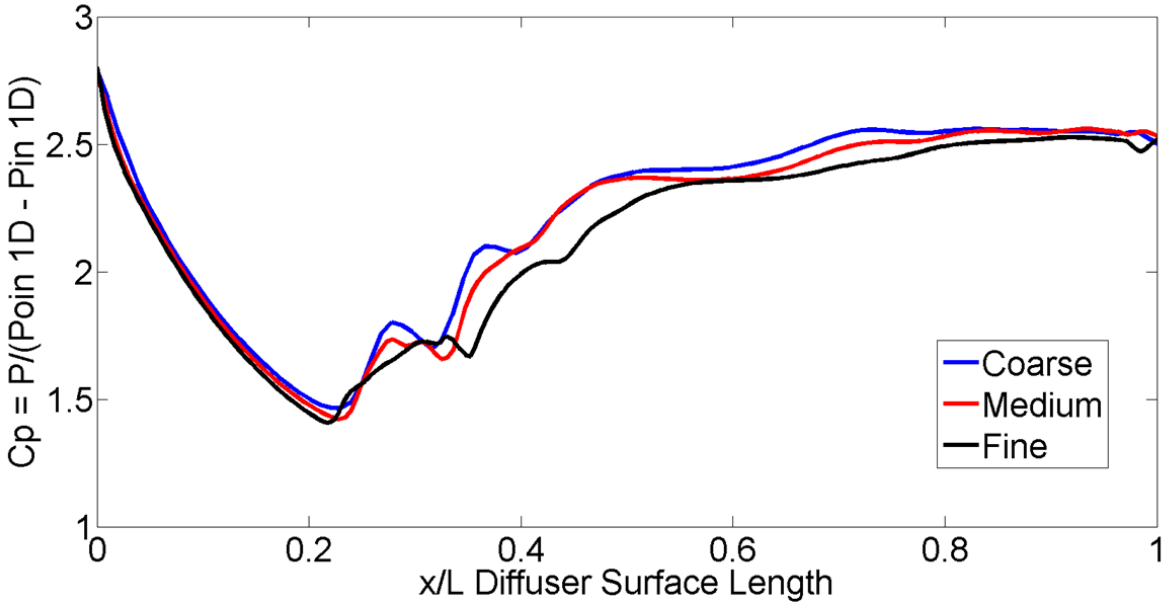

FIGURE 3.8. NORMALIZED STATIC PRESSURE ON DIFFUSER CASING SURFACE LENGTH FOR THREE DIFFERENT MESH SIZES

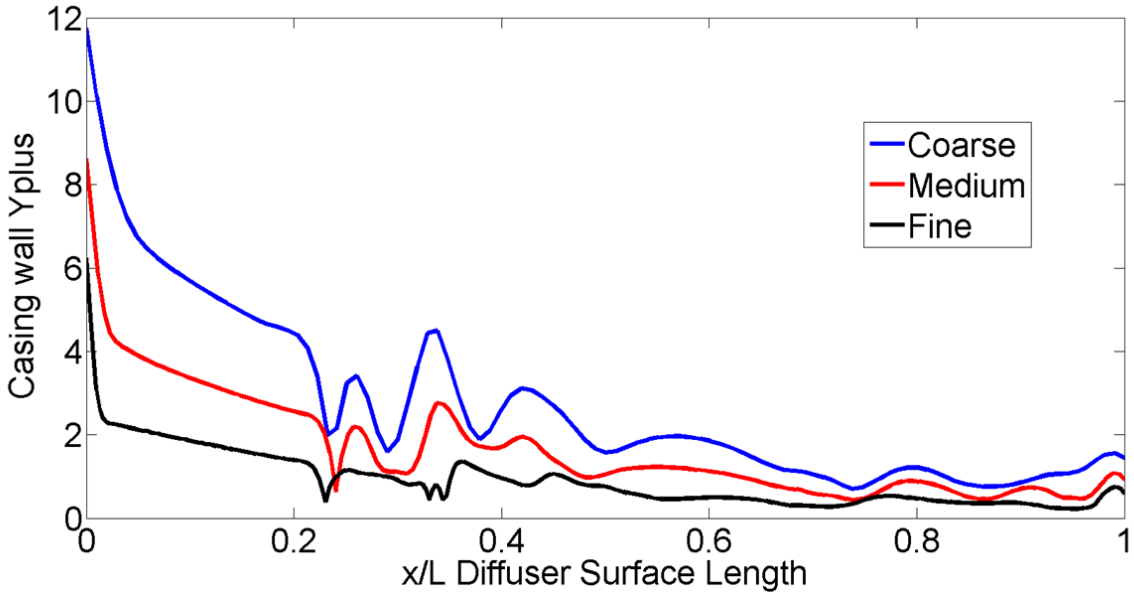

FIGURE 3.9. DIFFUSER CASING WALL YPLUS VALUES FOR DIFFERENT MESH SIZES

3.4 Axial-radial diffuser design

Once a stage mesh has been generated using the steps described in the previous section, an axisymmetric diffuser can be constructed using the coordinates from the rotor exit block. Since the focus of this project remains the casing side flow, a flexible method for modifying the shape of the casing was necessary.

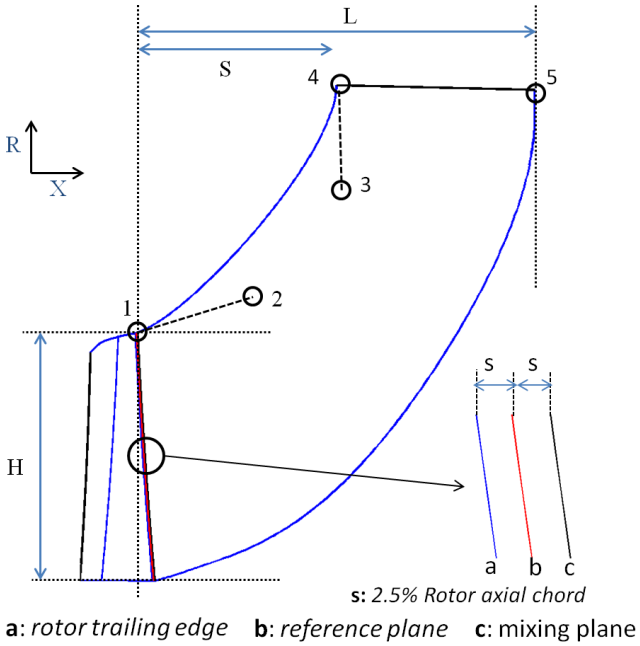

FIGURE 3.10. DIFFUSER CASING/HUB PROFILING DEPICTING DEFINITIONS OF REFERENCE PLANES AND DIFFUSER ASPECT RATIO PARAMETERS

Using the datum blade geometry, meshes were generated via automated parametric software written in the MATLAB specifically for this study. After generating the stage mesh, an axisymmetric diffuser was generated using the blade exit coordinates as described below:

The casing profile was generated by four control points (marked 1-4 in Figure 3.10) using a Bezier curve which can be derived from the sum of Bernstein polynomials as shown below:

$$\mathrm{B(t)} = \sum_{k=1}^{n} \binom{n}{k} (1-t)^{n-k} t^{k} \mathrm{P_n}, \mathrm{t} \in [0,1] \qquad \textbf{(3.2)}$$

Here, the casing coordinates are described by B(t) and its shape depends only on the relative position of knot points P_n (n = 1-4). Point 1 is determined from the rotor geometry and is specified as the casing coordinates of the rotor exit block. Point 4 is determined by a given S/H ratio (where H is fixed and is equal to the blade height). It should however be noted here that generally a designer is constrained by an axial limit of the hub line (i.e. Point 5) due to the presence of shaft bearings and the adjacent LP turbine casing which has to be compounded on the same shaft. The actual aspect ratio of diffuser is fixed by the L/H ratio and S is derived using the specified diffuser area ratio. Thus, the position of points 4 and 5

depend on the L/H ratio and the required area ratio. The relative position of Points 2 and 3 with respect to Points 1 and 4, determines the casing inlet and exit angles. Thus, Points 2 and 3 are evaluated such that the diffuser inlet casing is in-line with the rotor casing at the inlet and purely radial at the exit.

Points 2 and 3 can be regarded as the knot points that can be stretched or released to provide any desired smooth curve. Once the position of these points was determined, a casing profile was generated using software written for this study using MATLAB. Following this, the diffuser hub profile was generated such that area ratio would increase linearly along the diffuser surface length. A blending (using a 'Piecewise cubic Hermite interpolation') was provided such that the rotor hub profile can smoothly connect with the diffuser hub profile. An auto-optimization was performed using MATLAB global optimization software (using a genetic algorithm) for a standalone parameterized diffuser. The inlet boundary conditions were taken from a previously converged coupled rotor-diffuser solution. The diffuser casing profile was kept as the design variables while the diffuser pressure coefficient (CP) was kept as the objective function to be maximized. The optimized standalone diffuser generated in this step was fed to the calculations discussed in the results section. The S/H value for this study was set at 0.8 with an area ratio of 1.75. These values were selected in order to obtain a realistic L/H = 1.61 since industrial L/H varies between 0.9 to 2.1 (Private communication with Alstom Power, Rugby, UK 2012). A modest area ratio value ensured unseparated diffuser casing such that flow features can be studied as described in the next chapter.

3.5 Flow averaging

In order to compute the one-dimensional performance factors through the rotor and diffuser domain, the three-dimensional flow field variables need to be averaged. Although no three-dimensional flow can truly be represented by a single set of flow variables, different averaging methods can be applied based on need as mentioned by (Greitzer, Tan and Graf 2004) and (Cumpsty and Horlock 2006) and (Pianko and Wazelt 1983). For the purpose of this project area, mass and mixed-out averaging were employed.

A static flow quantity (F) can be area averaged as shown below:

$$\bar{F} = \frac{\int F.\,dA}{A} \tag{3.3}$$

where letters have their usual meanings.

A stagnation flow quantity (F) can be mass averaged as shown below:

$$\bar{F} = \frac{\int F.\,d\dot{m}}{\dot{m}} \tag{3.4}$$

$$\bar{F} = \frac{\int F.\rho.\,(V.\,dA)}{\dot{m}} \tag{3.5}$$

where letters have their usual meanings.

It may be noted here that these averages can be performed in both 3D and 2D space depending on the need. For example, 2D space averaging (in I-K planes) is used to compute spanwise distribution of flow quantities in the subsequent sections. These averages are useful to obtain diffuser performance and plotting of the pitchwise averaged quantities through the diffuser. The mixed-out average is computed using mass, momentum and energy conservation equations(Pianko and Wazelt 1983) for rotating ($\omega = \text{constant}$) frame of reference as shown below:

Continuity:

$$K_c = \bar{\rho}\overline{W_m} = \frac{\int \rho.\,W_m.\,dA}{A} \tag{3.6}$$

Meridional momentum:

$$K_m = \bar{\rho}.\,\overline{W}_m + \overline{P_s} = \frac{\int (\rho.\,{W_m}^2 + P_s).\,dA}{A} \tag{3.7}$$

Moment of momentum:

$$I_m = \bar{r}.(\omega.\bar{r} + \bar{W}_\theta).\bar{\rho}\bar{W}_m = \frac{\int r.(\omega.r + W_\theta).\rho.W_m.dA}{A} \quad (3.8)$$

Energy:

$$E = \left(\bar{h}_s + \frac{\bar{W}^2}{2} - \frac{(\omega\bar{r})^2}{2}\right).\bar{\rho}\bar{W}_m \quad (3.9)$$

$$= \frac{\int (h_s + \frac{W^2}{2} - \frac{(\omega r)^2}{2}).\rho.W_m.dA}{A}$$

Equation of state:

$$\bar{h}_s = \frac{\gamma}{\gamma - 1}\frac{\bar{P}_s}{\bar{\rho}} \quad (3.10)$$

Mean radii:

$$\bar{r}^2 = \frac{\int r^2.\rho.W_m.dA}{\int \rho.W_m.dA} \quad (3.11)$$

$$\bar{W}^2 = \bar{W}_\theta^{\,2} + \bar{W}_m^{\,2} \quad (3.12)$$

These equations are defined in the meridional plane and contains six unknown variables: $\bar{P}_s$, $\bar{\rho}$, $\bar{h}_s$, $\bar{W}_m$, $\bar{W}_\theta$ and $\bar{r}$. Rearranging these equations and solving for $\bar{W}_m$ gives a quadratic solution for which only one root satisfies the second law of thermodynamics in both subsonic and supersonic regions (Pianko and Wazelt 1983). Thus, $\bar{W}_m$ can be expressed in terms of known quantities as shown below. Please note that for the case of an absolute frame ($\omega = 0$), the relative velocity (W) is replaced by absolute velocity (V).

$$\bar{W}_m = \frac{\gamma}{\gamma - 1}\frac{I_m}{K_c.A} - \sqrt{\left(\frac{\gamma}{\gamma - 1}\frac{I_m}{K_c.A}\right)^2 - 2\frac{\gamma - 1}{\gamma + 1}\left(\frac{E}{K_c.A} + \frac{(\omega\bar{r})^2}{2} - \frac{\bar{W}_\theta^{\,2}}{2}\right)} \quad (3.13)$$

Using $\bar{W}_m$, other flow variables can be evaluated from the previous equations. For the purpose of this project, pitchwise mixed-out averages are computed at each spanwise location. Then, in order to separate streamline curvature difference with losses due to non-uniformities, a spanwise mass average value is used to compute 1D averages.

3.6 Solver Validation against Test Data

Specific Heat at constant pressure (c_p)	3919.270 J/Kg/K
Gas constant (γ)	1.124
Inlet Stagnation Pressure	0.935 Bar
Inlet Stagnation Temperature	344K
System Pressure Ratio (P_{oin}/P_{sout})	3.75
Nominal Turbine running speed	12604 rpm
Working fluid	Heavy gas (90% SF6/10% Air by weight)

Table 4. ALSTOM RIG TEST CONFIGURATION FOR CFD MODELLING

In the year 2010, Alstom Power (industrial collaborator for the project) conducted a series of tests involving last stage blades and its exhaust hood over a range of operating conditions. These tests were based on real site conditions and were meant to help provide a retrofit proposal and greater understanding of: 1) rotor tip gap size on the stage and its axial-radial diffuser performance, 2) effect of L/H ratio (as defined earlier) on the stage efficiency and 3) testing different 3D shapes of the diffuser and influence on stage-exhaust hood performance. Detailed examples of similar 3D diffuser shapes have been provided by (Yoon, Stanislaus, et al. 2011) via CFD studies and optimization of diffuser casing line. Subsequently, Alstom Power provided the test data in kind, so that this solver validation could be made against the actual site conditions for the current project. This section describes the test rig configuration for which the TBlock validation studies are provided. The objective of this validation was to evaluate if the predicted rotor exit conditions are in line with traverse test measurements and to determine whether the diffuser performance is

correctly predicted with the turbulence model used. Although most of the calculations performed in this project are with an un-separated diffuser casing only, some simulations do have separated diffusers later on in chapter 6.

The test rig consisted of a 0.1154 scaled model of the real site stage conditions and standard exhaust hood (L/H = 0.935) was attached to the stage. Figure 3.11 shows the layout of the test rig with visible sections of stator coloured in red, rotor in green and diffuser in blue. Here, the stator consisted of 48 blades while rotor had 55 blades. A pressure ratio of 3.75 was maintained across the system such that the working gas can flow from stage inlet to exhaust exit. Table 4 gives details of the rig test configuration used for CFD calculations.

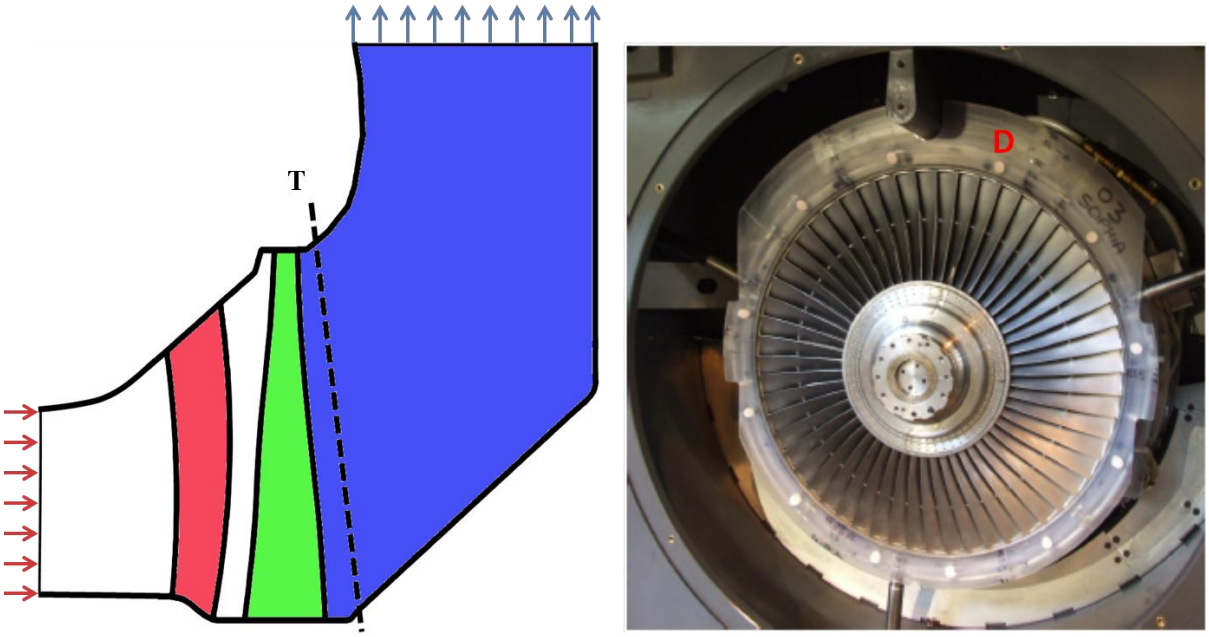

FIGURE 3.11. TEST RIG REPRESENTATIVE LAYOUT AND NON-AXISYMMETRIC DIFFUSER IN A RIG SET-UP (LABELLED AS 'D')

The rotor exit flow conditions were measured along plane T (Figure 3.11) and similar traverse probes were located at the stage inlet and diffuser exit from which boundary conditions were determined. The case study selected for solver validation contains a non-axisymmetric diffuser (Figure 3.11). Thus, a longer diffuser (upper part) was shortlisted to perform axisymmetric calculations. Since the flow will be asymmetric along the perimeter of the diffuser, two circumferential positions (hereby referred to as measuring plane 1 and 8) were compared within a longer diffuser casing side. Looking at Figure 3.12, planes 1 and 8 are marked at an angle of 27 degrees from either side of the vertical axis. On the right-hand

side of Figure 3.12 are shown the respective pressure probe positions along each measuring plane (1 and 8) on the diffuser casing. These planes were selected to simulate a longer part of the diffuser casing as shown in Figure 3.12. Although circumferential positions are identical on either side of the vertical axis, two positions could average the effect of the stator wake (if present) and more importantly, the asymmetric flow exiting the rotor due to the circumferential exhaust asymmetries. The pitch angle was with respect to the meridional velocity and the swirl angle was with respect to axial velocity (see Figure 3.13).

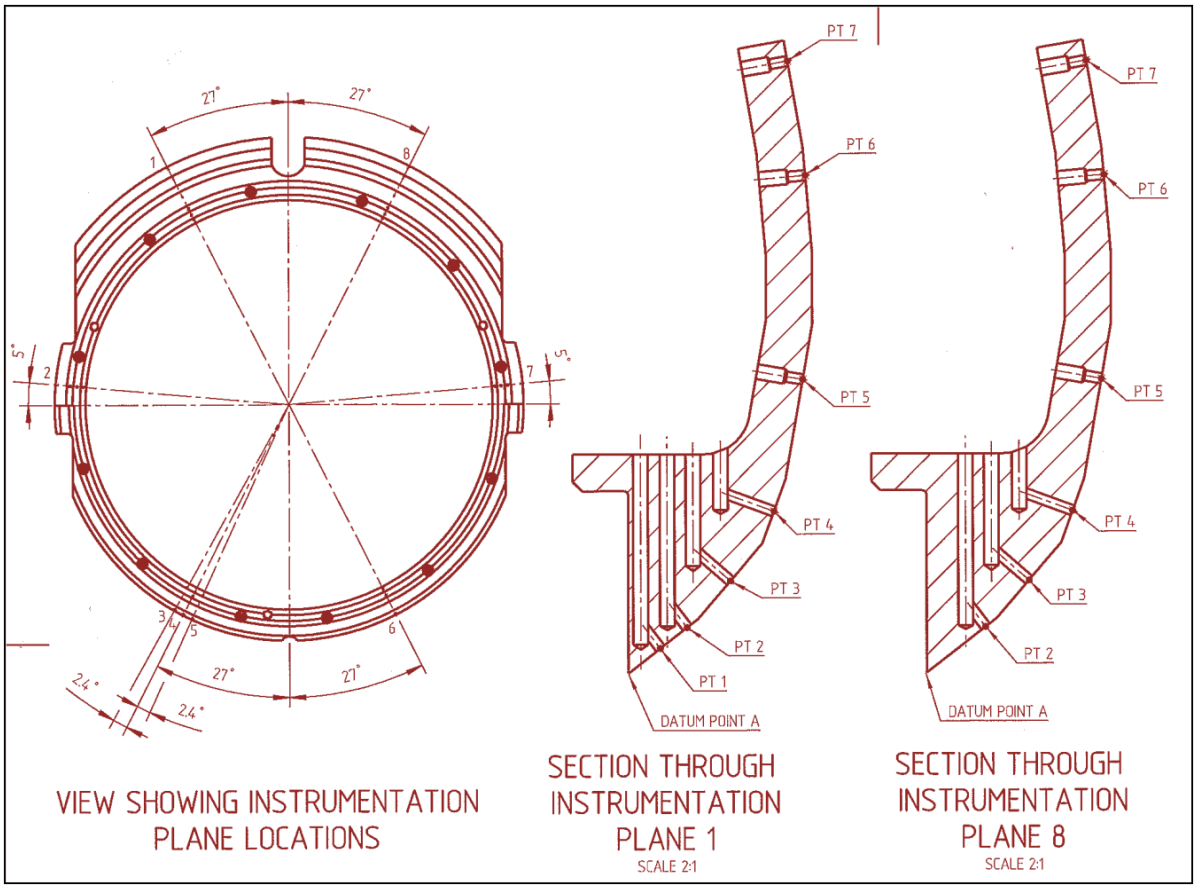

FIGURE 3.12. POSITION OF PROBES ON DIFFUSER CASING (ALSTOM POWER, UK 2012)

It may be noted here that the diffuser casing turns (Figure 3.12) more than 90^{o} with design L/H value of 0.935. Such tight exhaust conditions place the present diffuser into a highly aggressive category. Moreover, the casing profile is kinked (discontinuous slope) at several places along its surface length. Under these conditions, the diffuser casing boundary layer will likely separate, which makes this case particularly challenging for the solver. Also, the traverse plane T (see Figure 3.11 and Figure 3.13) is located after the first kink (discontinuity in slope) where the flow is likely to separate. The diffuser shown in Figure

3.13 is different from the actual design shown in Figure 3.11 and is provided for representational purposes of flow angles only. Comparing the one-dimensional diffuser performance factors for asymmetric diffuser's experimental results with axisymmetric computational results will not give one-to-one comparison. Thus, a comparison will be provided only within specific regions of experimental study under which the computational studies are based.

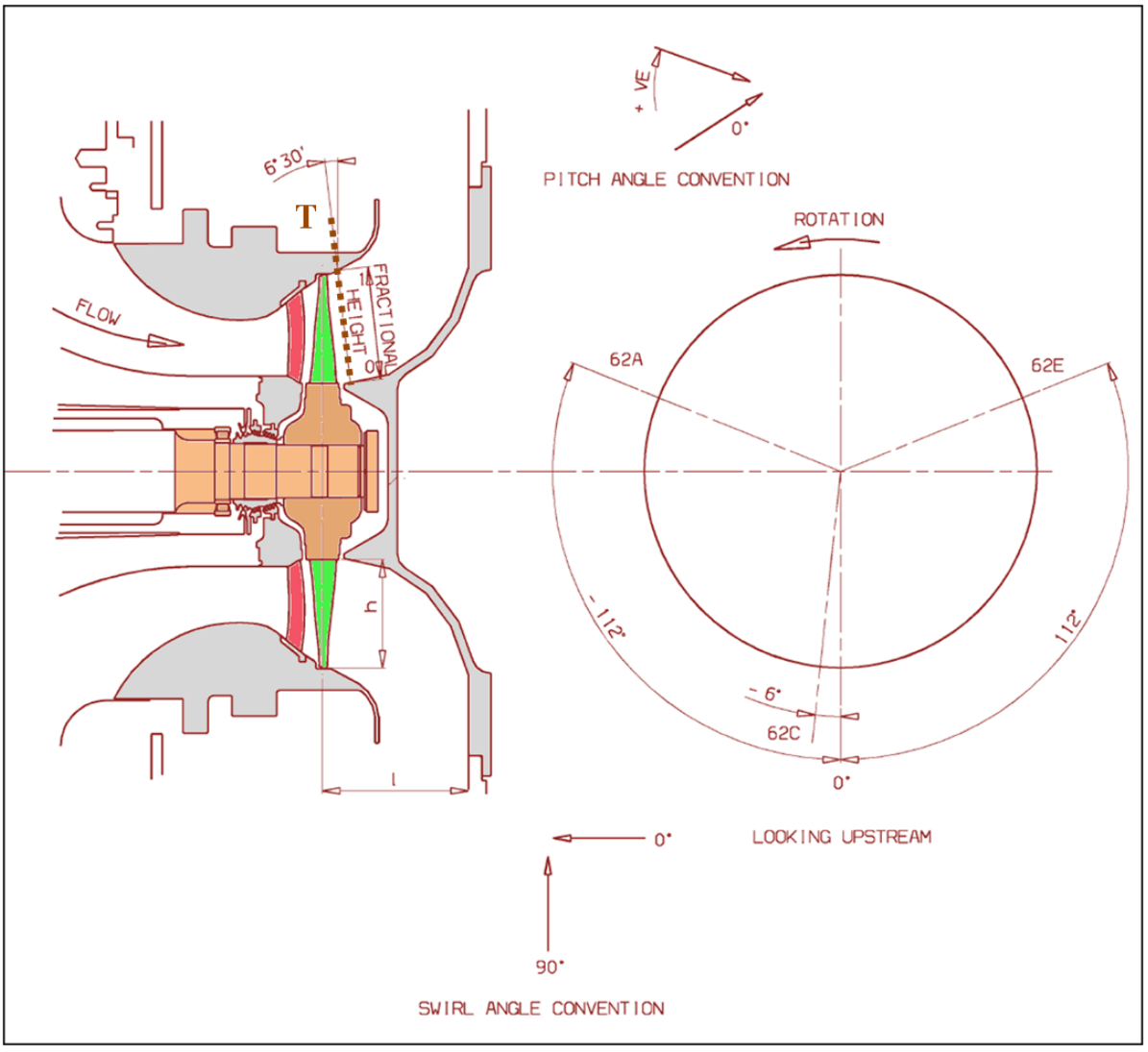

FIGURE 3.13. PITCH ANGLE AND SWIRL ANGLE CONVENTION (ALSTOM POWER, UK 2012)

The method to configure the computational set-up for this industrial case was similar to the description given in section 4.0. The diffuser design was fixed and its mesh was directly generated using geometry coordinates imported from the Alstom test data. To start with, the initial set of boundary conditions at the stator trailing edge were obtained from an H-grid based stage.

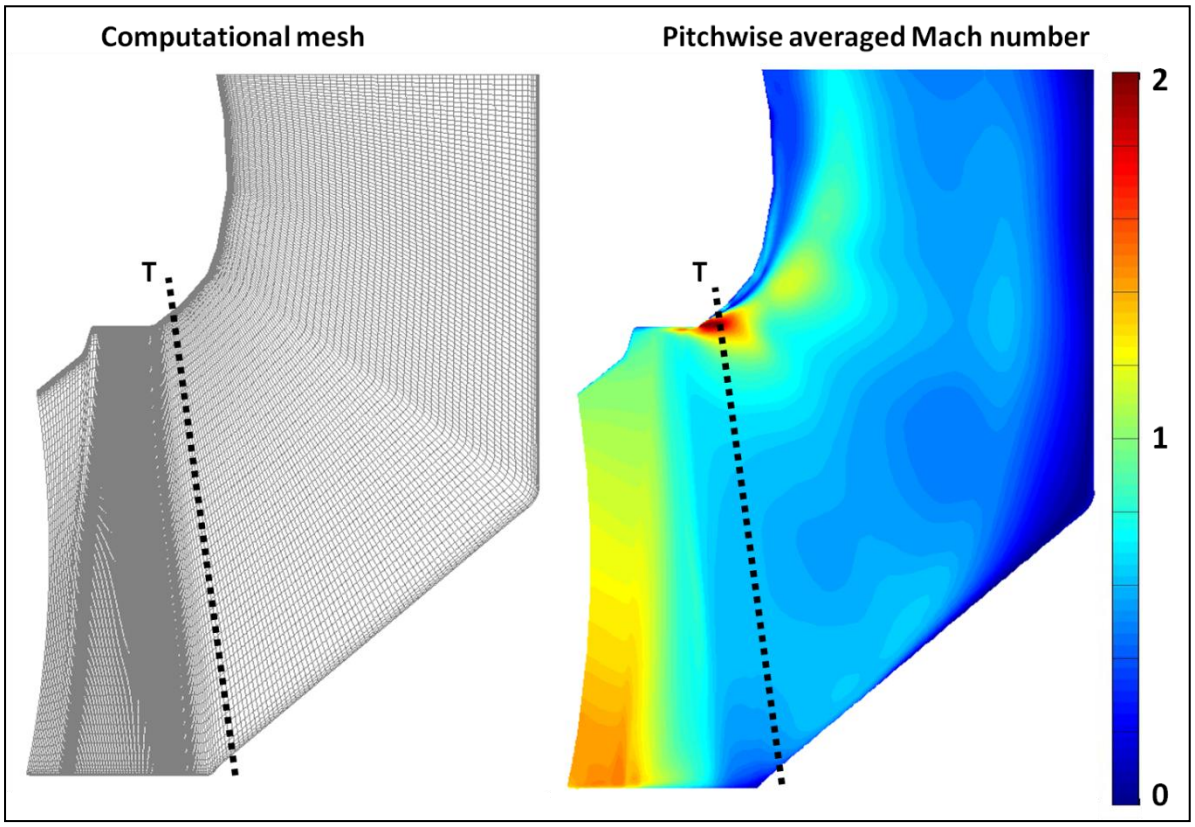

FIGURE 3.14. MESHING USED FOR ROTOR-DIFFUSER FLOW DOMAIN AND PITCHWISE MASS AVERAGED ABSOLUTE MACH NUMBER COMPUTED (USING SA MODEL) IN THE MERIDIONAL PLANE

Figure 3.14 plots the computational mesh for the industrial test case along with the pitchwise mass averaged Mach number within the flow domain. As pointed out in the chapter 2, the loss production within a diffuser has a direct impact on its performance. Thus, looking at the large flow separations on casing side, must constitute a major source of loss in the diffuser flow. The data reflects that efforts must be made to reduce the flow separations on the diffuser casing. The plot also shows the presence of high energy fluid leaking out from the rotor tip gap region. This flow mixes out with the primary flow and helps supersonic flow expand over the diffuser casing. Chapters 4-6 will discuss these concepts in detail.

Figure 3.15 and Figure 3.16 gives the computed rotor exit pitchwise mass averaged results against rig test results along the traverse plane T and Figure 3.17 provides the diffuser casing results against the circumferential probe positions shown in Figure 3.12.

Figure 3.15 plots the rotor exit relative Mach number distribution along the span against the experimental results (i.e. along plane 1 and 8 described earlier). Here, two sets of computational results are plotted, from simulations using a mixing-length (labelled as "TBlock ML") model and a Spalart-Allmaras (labelled as "TBlock SA") turbulence model. Both models predict the relative Mach number values near to the measuring plane 8 with SA model in general closely matching the data over the majority of the span. Close to the casing, the SA model appears to over-predict the Mach number, as compared to the experimental data; this is likely due to an under prediction of the rate of mixing of the tip leakage flow in this region. The mixing length model prediction falls between the plane 1 and plane 8 values. It should be noted here that differences in relative Mach number between plane 1 and plane 8 measurements is around 0.2; the data suggests the presence of a highly three dimensional flow within the diffuser region or a stator wake along plane 1. Figure 3.16 plots the rotor exit relative yaw and pitch angles. Here, as described earlier, yaw (swirl) angle is referenced with respect to flow axial velocity and pitch angle is referenced with respect to the meridional velocity. The CFD results and experimental data are in good agreement over most of the span. Between 80-100% span there appears to be an over prediction of swirl and under prediction of pitch which can be explained from large separations predicted by CFD due to the presence of discontinuities along diffuser casing.

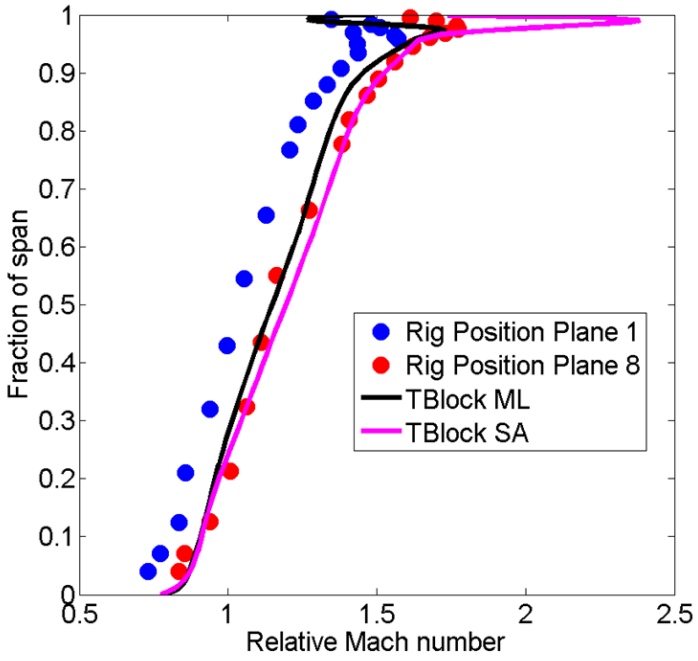

FIGURE 3.15. ROTOR EXIT PITCHWISE AVERAGED RELATIVE MACH NUMBER

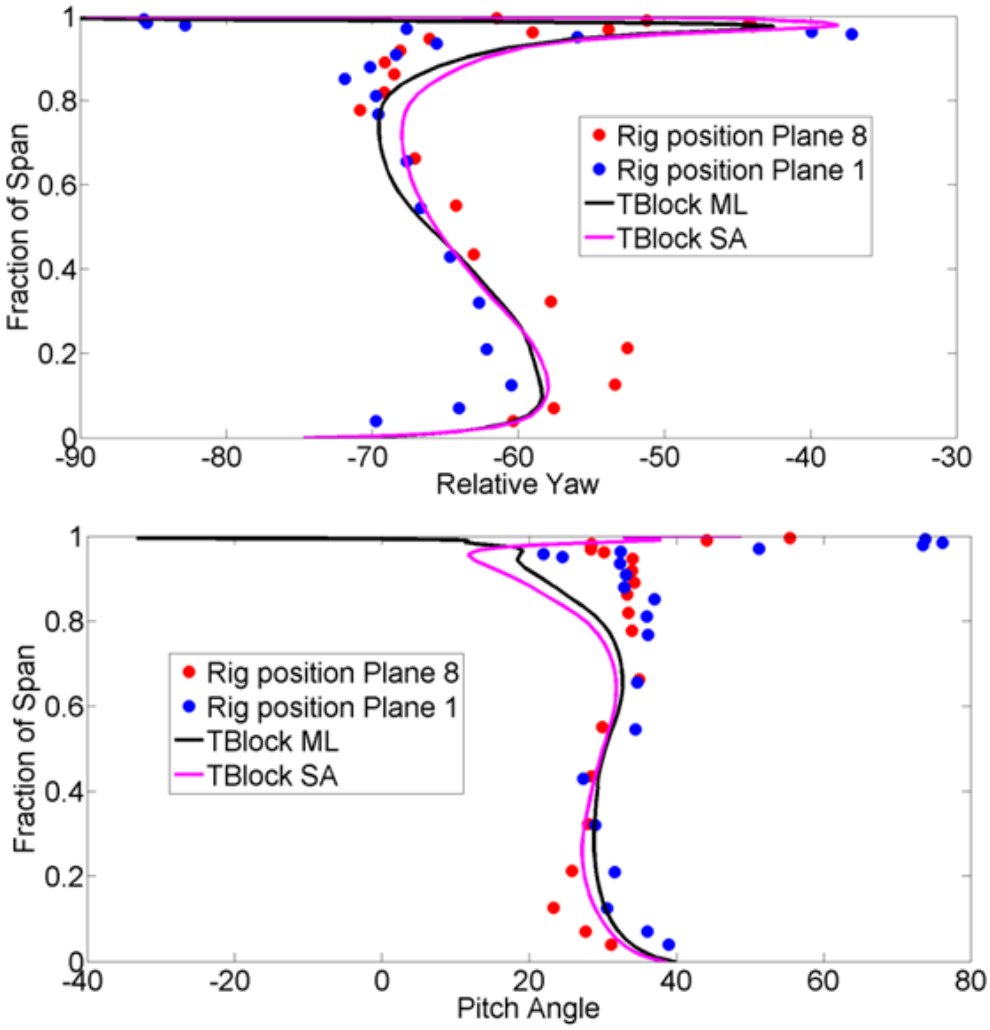

FIGURE 3.16. ROTOR EXIT PITCHWISE AVERAGED RELATIVE YAW ANGLE AND PITCH ANGLE

Figure 3.17 shows the variation on the casing of the diffuser over the lip surface. The rig position of planes 1 and 8 and pressure probe positions are consistent with their description in Figure 3.12. The results show a good agreement between experimental and SA turbulence model data for the majority of the surface length. The mixing length model in contrast fails to predict lip static pressure accurately. It was communicated by (J. Denton, Personal communication 2015) that the TBlock-11.9 mixing length model does not work well with low values of YPLUS because it assumes that only the first two grid points are in the viscous sub-layer and treats all other points as turbulent. It is possible to improve mixing length predictions by assigning YPLUS about 30 at the second grid point. However, such mesh distortion won't provide a true one-to-one comparison between these cases. In general the agreement between the CFD and experiment is very encouraging, and the following

chapters simulations are presented using the SA model, since this appears to predict more accurately the flow within the diffuser.

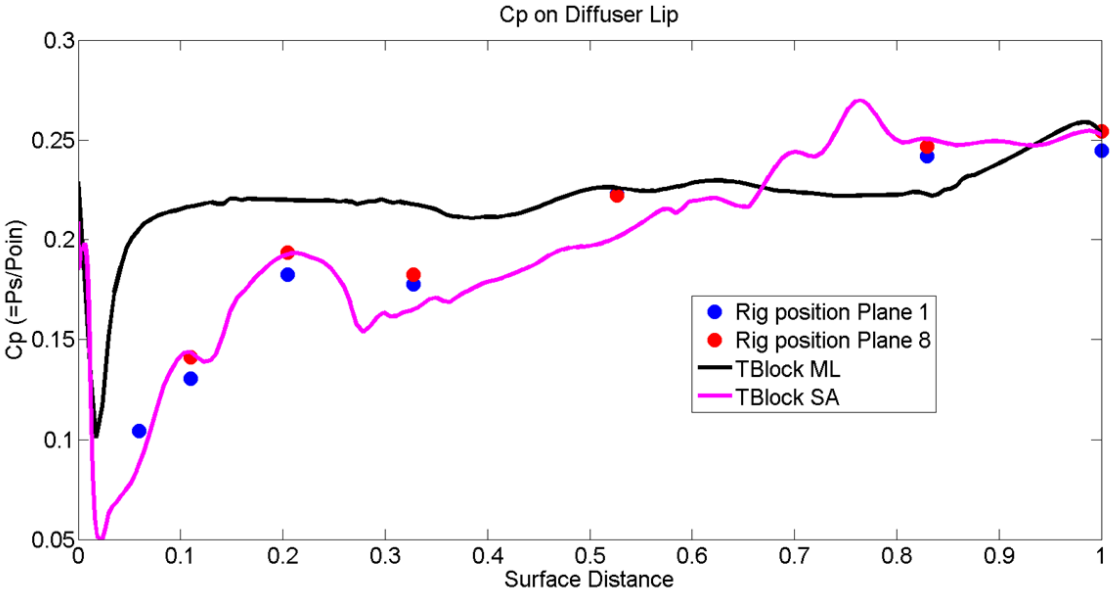

FIGURE 3.17. PRESSURE RISE ON DIFFUSER CASING (LIP)

3.7 Conclusions

This chapter described the flow solver and the usage of Spalart-Allmaras (SA) turbulence model in the present study. An industrial test case using which the flow solver predictions have been validated in view of the scope of results in the subsequent result chapters. The design and meshing of rotor, diffuser and tip gap blocks have been explained in detailed and a mesh dependence study has been provided. This chapter also covered the flow averaging methods based on which all 1D performance factors and pitchwise averaged results have been derived throughout this thesis.

4: Flow physics of interactions within LSB-Diffuser

Chapter Outline:

This chapter will investigate the interaction mechanisms between the rotor and diffuser. The understanding gained in this chapter will form the basis of design configurations explored in the subsequent chapters of this thesis. By varying the type of interface applied between the rotor and diffuser, and varying the tip gap, certain flow features will be studied in isolation, and their effect on the rotor and diffuser performance factors will be determined.

4.1 Introduction

The rotor-diffuser working geometry was generated as described within chapter 3 and the diffuser area ratio was set to 1.75, with L/H = 1.617 and S/H = 0.8 (refer to section 5.0 in chapter 3). Eight test cases were investigated in order to determine the effects of the rotor/diffuser interactions on diffuser performance, as described in Table 5. The test cases with and without a mixing plane (MP) interface between the rotor and diffuser blocks were investigated; this comparison will determine the influence of circumferential non-uniformity on the diffuser and rotor/diffuser system. Also test cases were investigated with and without a rotor tip gap for both with and without mixing-planes. These test cases were also configured to run at two system pressure ratios of 3.92 and 4.40 such that a realistic diffuser inlet absolute Mach number of 0.6 - 0.8 can be obtained. Such values indicate a typical leaving loss exiting the rotor unless recovered by the diffuser.

Figure 4.1 plots the rotor and system efficiencies for the eight test cases described in Table 5. The system efficiency is based on the total-to-static isentropic efficiency across the rotor-diffuser, where the exit static pressure is determined from the area-average static pressure over the diffuser exit plane. The rotor total-to-total efficiency is determined based on a constant area mixed-out (in circumferential and spanwise directions) average at the rotor exit plane (as defined in Chapter 3, Section 3.0). For the idealized case where an isentropic diffuser is able to diffuse the flow to a stagnation condition at diffuser exit, the system and rotor efficiencies would be equal. The difference between rotor and system efficiencies is thus a measure of the diffuser performance, while the rotor total-to-total

efficiency is a measure of the rotor performance only. This is due to the use of mixed-out quantities to determine the rotor efficiency, which account for any downstream loss which would have been generated if the rotor was coupled to a constant area duct; in practice, the mixing of the rotor flow in the three-dimensional pressure field of the diffuser will affect the mixing loss, and this will be explored later in this chapter

	No TipGap MP	**No TipGap**	**with TipGap MP**	**with TipGap**
SysPr = 3.92	A1	B1	C1	D1
SysPr = 4.40	A2	B2	C2	D2

TABLE 5. TESTS CASES FOR ROTOR/DIFFUSER INTERACTIONS

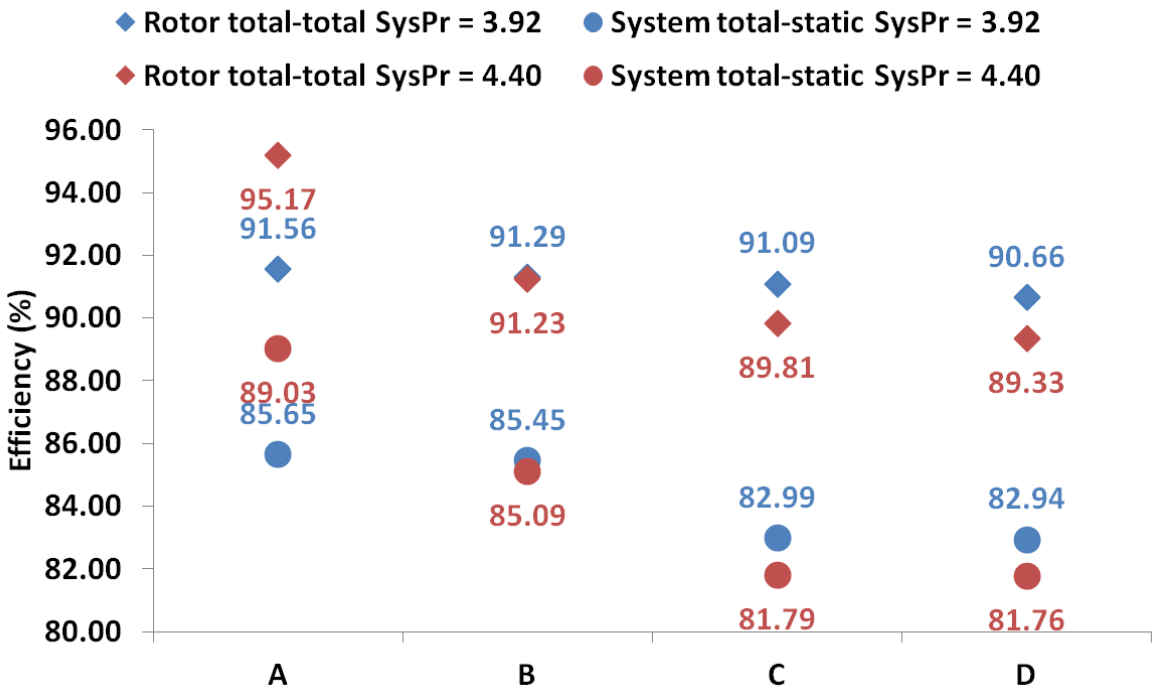

FIGURE 4.1. ROTOR AND SYSTEM EFFICIENCIES FOR DIFFERENT TEST CASES AS IDENTIFIED IN TABLE 5

At a system pressure ratio of 3.92, Figure 4.1 shows that the effect on rotor performance due to circumferential non-uniformities (comparing A1 to B1 or C1 to D1) is to reduce rotor

efficiency by about 0.35% on average. The addition of a leakage flow (comparing B1 and D1) reduces rotor efficiency further by about 0.6%. The effect on the system due to the addition of a leakage flow is much larger (comparing A1 and C1 or B1 and D1), reducing the system efficiency by 2.6% on average. This suggests that the diffuser pressure recovery is being reduced as a result of the interaction of the leakage flow. At the higher pressure ratio of 4.40, the effects of both circumferential non-uniformity and leakage flow appear to have a much greater influence on the rotor performance. In the absence of a leakage flow, circumferential non-uniformity reduces the rotor efficiency by 4% (comparing A2 and B2), while the leakage flow reduces rotor efficiency by roughly 2% (comparing B2 and D2). The system efficiency follows the same trend as the rotor efficiency, although, as with the lower system pressure ratio, the difference between the system and rotor efficiencies is increased for the cases with leakage flow. Correspondingly, the rotor specific work output values (see Figure 4.2) follows a similar trend as depicted by the rotor total-to-total efficiency. Again, the work output reduces due to circumferential non-uniformities (A1 to B1 or C1 to D1) and this is exacerbated at higher system pressure ratios. Similarly, the rotor output reduces due to the presence of a leakage flow (A1 to C1).

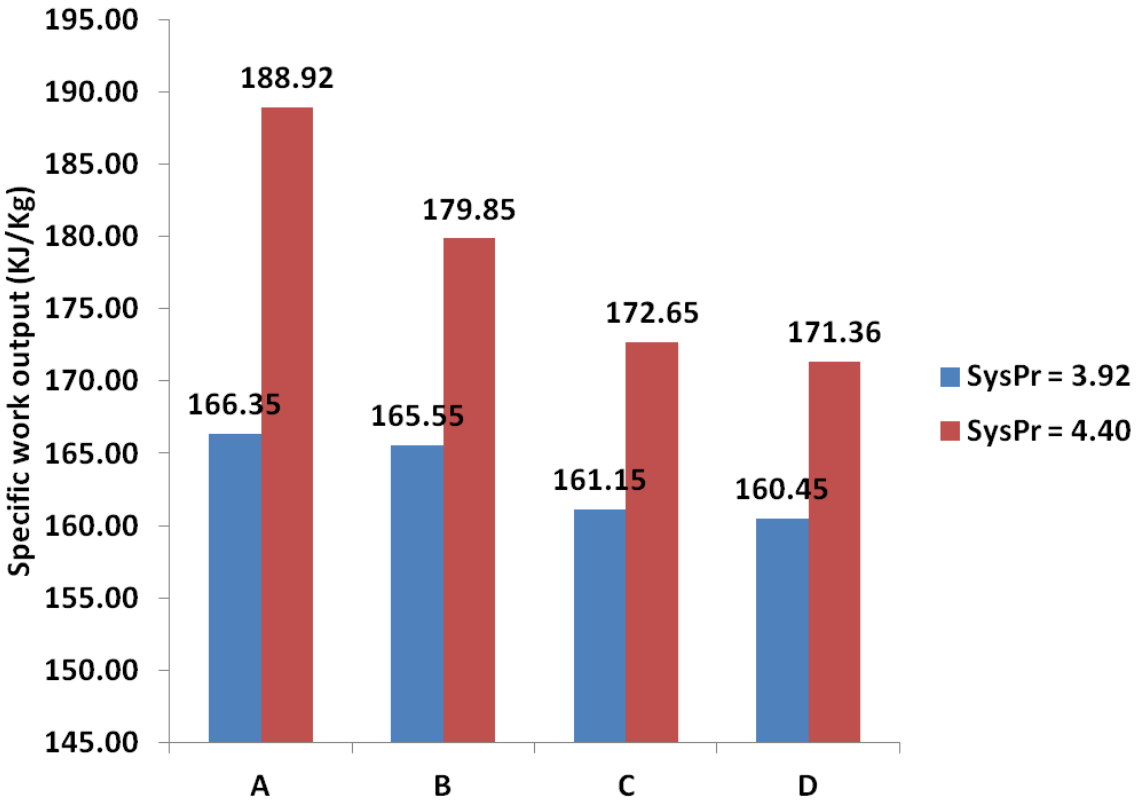

FIGURE 4.2. ROTOR SPECIFIC WORK OUTPUT FOR DIFFERENT TEST CASES IDENTIFIED

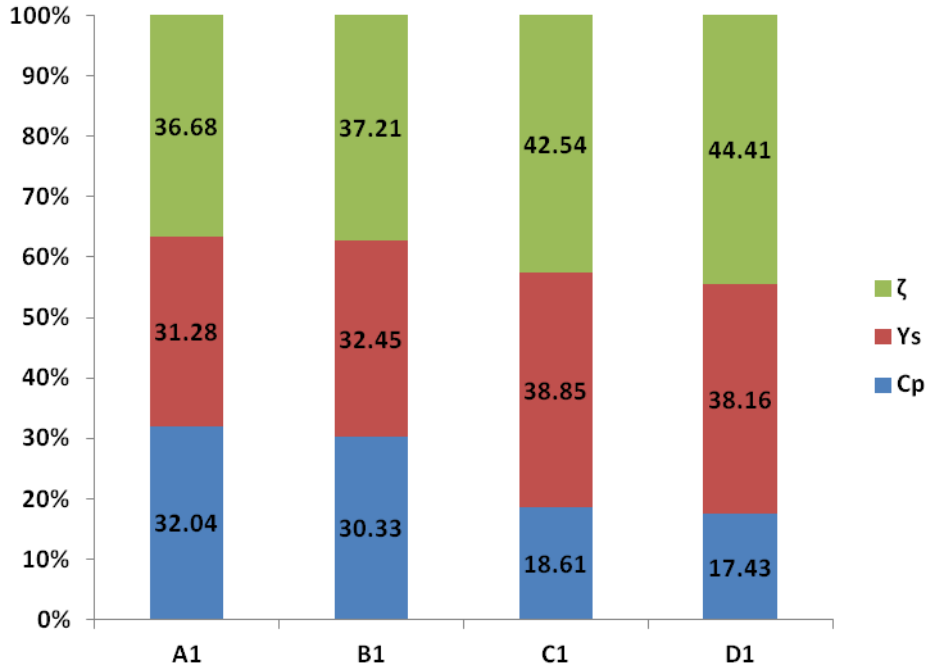

Figure 4.3. DIFFUSER PERFORMANCE FACTORS AT SYSPR = 3.92 FOR FOUR TEST CASES

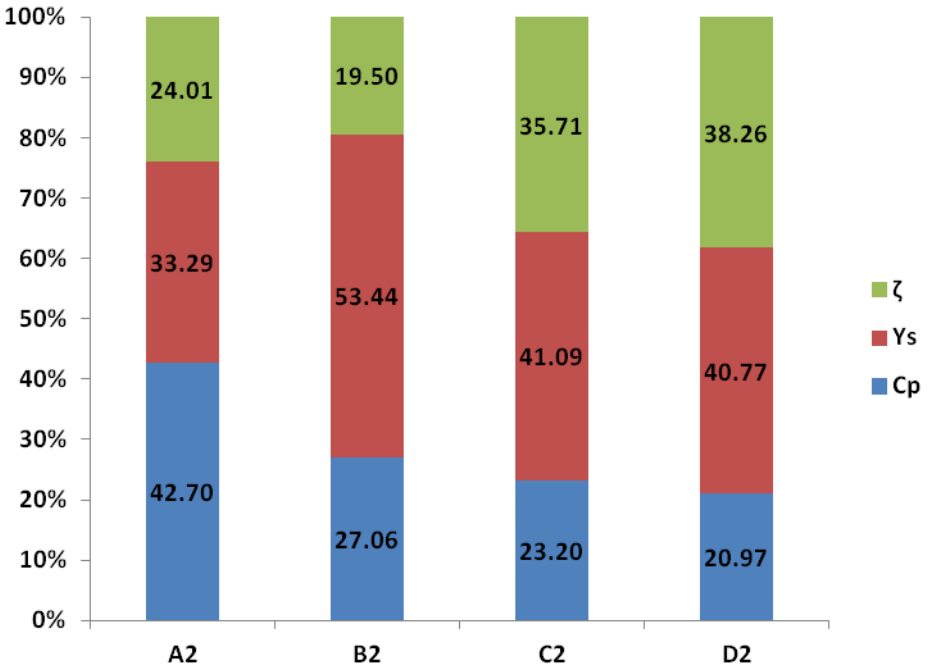

FIGURE 4.4. DIFFUSER PERFORMANCE FACTORS AT SYSPR = 4.40 FOR FOUR TEST CASES

The results suggest that the importance and nature of the rotor/diffuser interaction is strongly dependent on operating system pressure ratio, the presence of tip leakage flows and non-uniformities in the blade-to-blade plane. The following sections will first examine how the diffuser performance changes for these different test-cases; then the flows within the rotor casing region are examined; finally the effect of rotor casing shape on system performance will be explored.

4.2 The effect of rotor/diffuser interaction on diffuser performance

The reference plane used in the calculation of CP, ζ and Y_s was located upstream of the rotor/diffuser interface, so that for cases which contained a mixing-plane, the Y_s values contained the mixing-loss associated with the circumferential mixing of the flow which occurs across the mixing plane. The reference plane location is explained in section 5.0 of chapter 3.

The diffuser performance factors for the eight test cases are plotted in Figure 4.3 and Figure 4.4. Comparing cases with and without a mixing-plane, such as case A1 and B1, helps to determine the effect of circumferential non-uniformity on diffuser performance due to the presence of blade wakes and trailing-edge shocks. Similarly, comparison of the cases with a tip gap (C1 and D1) helps to understand the nature of loss production by a leakage flow as it moves within the diffuser flow.

At SysPr = 3.92 in Figure 4.3, the removal of the mixing plane leads to a 1.7% drop in CP (from A1 to B1) mostly due to an increase in total pressure loss. Thus circumferential non-uniformity appears to increase diffuser losses to a small extent; there is a 1.2% rise in loss when the mixing-plane is removed (comparing A1 and B1). Comparing the cases with and without tip-gap (i.e. A and C) in Figure 4.3 and Figure 4.4, shows that the leakage flow reduces the diffuser pressure recovery (CP) by increasing the diffuser loss (Y_s) and increasing blockage (ζ). Previous studies (discussed in chapter 2) have shown that in some cases the leakage flow can enhance CP, but this is normally associated with the effect of leakage flows in delaying separation and reducing blockage. For the case in this study, the diffuser does not exhibit a large-scale separation, and therefore this effect does not occur. For cases with a leakage flow (C and D) with and without mixing-plane at both pressure ratios, shows that the unmixed leakage flow appears to marginally reduce the diffuser loss,

but increase blockage (increase Y_s and ζ). Despite the reduction in loss, overall the increased blockage tends to reduce CP.

At the higher pressure ratio of 4.40, the increase in Y_s is much larger (see Figure 4.4), and there is a 20% increase in diffuser loss when the mixing plane is removed, which reduces the CP by 15.6%. Such a large increase in total pressure loss between A2 and B2 suggests the presence of additional loss mechanisms within the diffuser flow. The cause of this additional loss can be observed in Figure 4.5, which shows static pressure contours on a blade-to-blade plane at 97.50% of span. Identified on this figure are the positions of the mixing-plane, the diffuser inlet reference plane, and also the shocks emanating from the rotor trailing-edge. Between cases A1 and B1, the removal of the mixing-plane introduces shocks from the suction-side trailing-edge region (TE-SS) into the diffuser, but the pressure-side shock (TE-PS) which exists upstream of the mixing-plane remains relatively unaffected by the presence of the mixing-plane. At the higher pressure-ratio, the pressure-side trailing-edge shock (TE-PS) shifts downstream slightly due to the higher blade loading, such that now it crosses the diffuser/rotor interface when there is no mixing-plane (see B2) and is thus removed when the mixing-plane is present (see A2). It will be shown later that the increased diffuser loss observed between A2 and B2 (see Figure 4.1) is in-part due to the additional shock loss associated with the pressure-side arm of the trailing-edge shock entering the diffuser.

Figure 4.6 shows the pitchwise averaged absolute Mach number contours for the different tests cases discussed above. These contours are superimposed with very low (< 20m/s) absolute velocity contour lines (shown in red), thereby giving a sense of flow circulations near diffuser exit. Also, figures are superimposed with velocity vectors for pitchwise averaged diffuser meridional plane (shown in black), thereby giving sense of flow direction in the diffuser domain. Comparing A1 and A2 shows that increasing system pressure ratio increases the absolute Mach number near the diffuser casing. The casing side flow becomes transonic at the higher system pressure ratio, but remains relatively unchanged away from the casing, where the flow is subsonic. At the higher pressure ratio, normal shocks are observed near the casing (labelled X). Comparing A2 and B2 shows that the removal of the mixing-plane in B2 leads to a shift of this normal shock further downstream.

A casing normal shock (labelled as X) can be observed in C2 and D2 where a leakage flow is introduced. Again the removal of the mixing-plane leads to an increase in the normal shock strength; in D2 the shock causes a thicker boundary-layer and lower Mach number over the diffuser lip as compared to the mixing-plane case C2. The increased blockage can also be observed in the rise of ζ between the cases seen in Figure 4.4. It is interesting to note that the total loss in this case is not greatly affected by the mixing-plane (see Figure 4.4). It is possible that the increased shock loss is offset by a reduction in boundary-layer loss because of the reduction in casing lip Mach number, since viscous losses are highly dependent on the boundary-layer edge Mach number, and will increase with boundary-layer edge velocity cubed (J. Denton, 1993).

Comparing the corresponding values for test cases A, C and D between Figure 4.3 and Figure 4.4, it can be observed that the loss rises when the system pressure ratio is increased. Despite the increase in the loss, the pressure recovery (CP) increases due to the reduction in the blockage ζ. The effects of the interactions between the rotor and diffuser on the diffuser performance as discussed next.

In order to demonstrate the effect of the rotor/diffuser interactions on the diffuser lip surface static pressure, Figure 4.7 plots the local diffuser pressure recovery coefficient on the diffuser casing for the eight test-cases. Here, the local CP is computed as:

$$CP = \frac{P_{local} - P_{in}}{P_{o,in} - P_{in}}$$

Superimposed on the contours of pressure coefficient are contours lines of isentropic Mach number = 1, which identifies regions of supersonic and subsonic free-stream flow. Similarly, the trajectories of rotor blade wakes, trailing edge shock propagation and leakage flow traces are superimposed as shown in Figure 4.7. Looking at the mixing-plane cases A1 and A2, shows the effect of increased pressure ratio, which raises the lip loading and leads to a normal shock at X. When the mixing plane interface is removed, as shown in B1 and B2, the regions of supersonic flow extend much further into the diffuser (as identified by black contour lines). Very large fluctuations in the lip static pressure are observed and these are caused by the rotor trailing-edge shocks (labelled Y) as they propagate into the diffuser, creating a moving pressure field. The interaction of these shocks with the diffuser boundary-layer are likely to lead to additional losses, which can also contribute to the additional loss observed between cases with and without a mixing-plane.

The introduction of a tip leakage flow greatly diminishes the effect of the rotor trailing-edge shocks on the lip surface static pressure (comparing B1 with D1 and B2 with D2). When the leakage flow is present, the fluctuations in lip-surface pressure are largely due to the propagation of the leakage flow within the diffuser. Since the leakage flow tends to reduce the effect of trailing-edge shocks on the lip surface boundary-layer this may in-part explain why the presence of the mixing-plane has less effect on losses when there is a leakage flow present, as compared to the no tip-gap cases at the higher system pressure ratio.

Further insight into the variation in performance along the diffuser length can be gained from Figure 4.8. Here, the diffuser CP and Y_s are plotted using 1D averaged values along the diffuser surface length. At SysPr = 3.92, the CP tends to increase continuously along the diffuser length for the cases without a leakage flow. The primary rise in CP occurs within the first 40% of the diffuser length which is the region of highest curvature change along the diffuser length. CP values in A2 quickly rise due to the presence of a stronger pressure side arm of the trailing edge shock (shown in Figure 4.5). Since, the pitchwise non-uniformities are already mixed-out for cases A1 and A2, which include a mixing plane at s/So=0.01, the values of Y_s are nearly constant along the length of the diffuser. When the mixing-plane is removed, the mixing of the rotor wakes in case B1 creates a total pressure loss within the diffuser which is similar to the rise in total pressure loss across the mixing plane seen in A1. Thus, the effect of mixing the flow within the diffuser does not appear to greatly affect loss for this case.

The variation in CP and Y_s follows a similar trend to cases without tip gap when a leakage flow is introduced at SysPr = 3.92 in Figure 4.8. But the CP rise is not monotonic, especially near the diffuser inlet where the leakage flow undergoes a rapid expansion along the highly curved diffuser casing. Again, at the lower system pressure ratio, the mixing of the leakage flow within the diffuser appears to create a similar level of loss as the loss rise across the mixing interface.

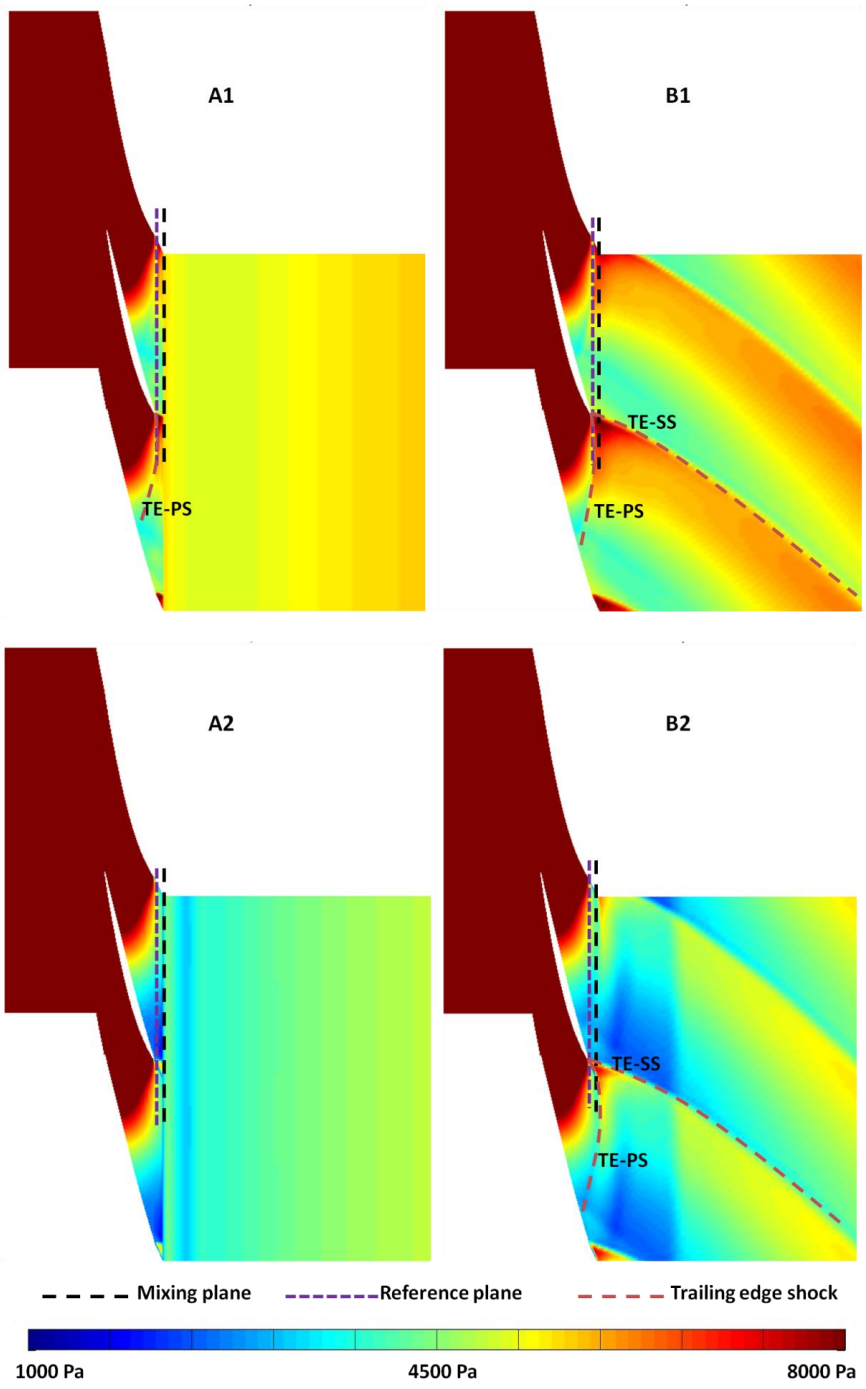

FIGURE 4.5. SLICE PLANE OF STATIC PRESSURE CONTOUR AT 97.50% SPAN

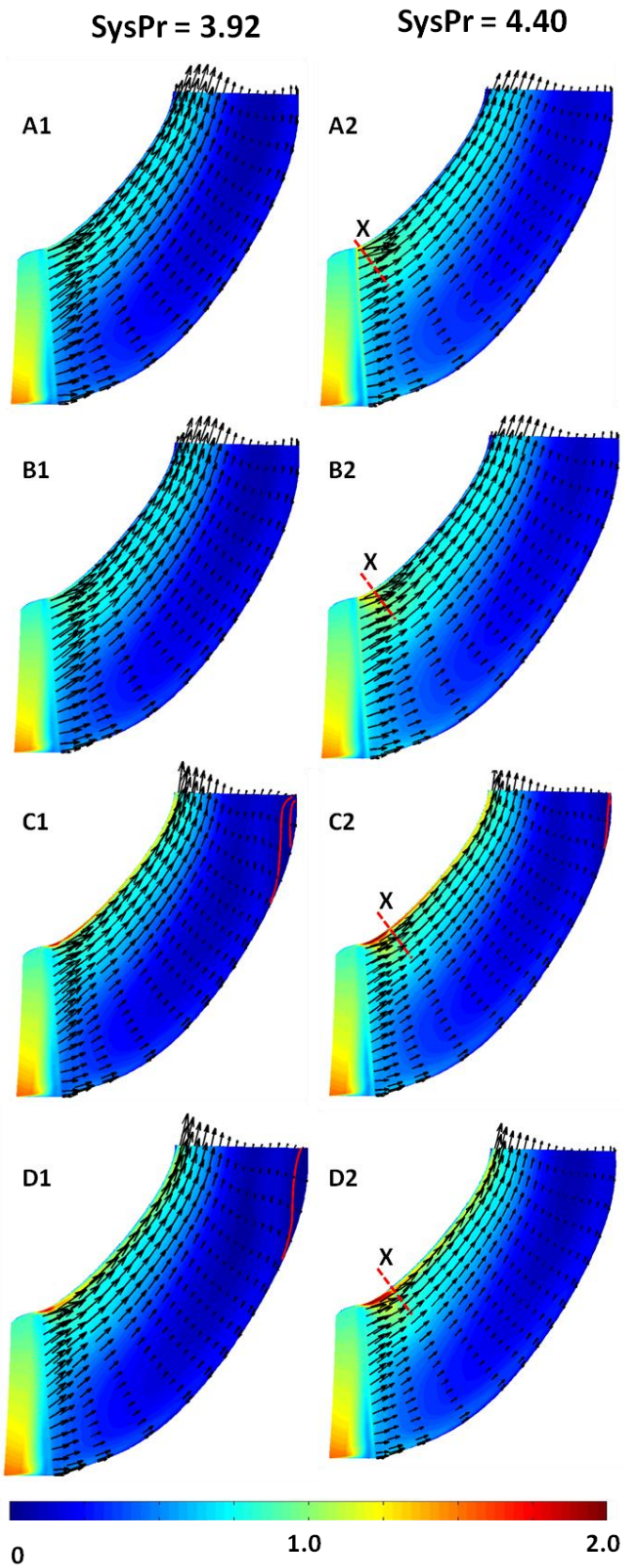

FIGURE 4.6. PITCHWISE AVERAGE ABSOLUTE MACH NUMBER FOR DIFFERENT TEST CASES

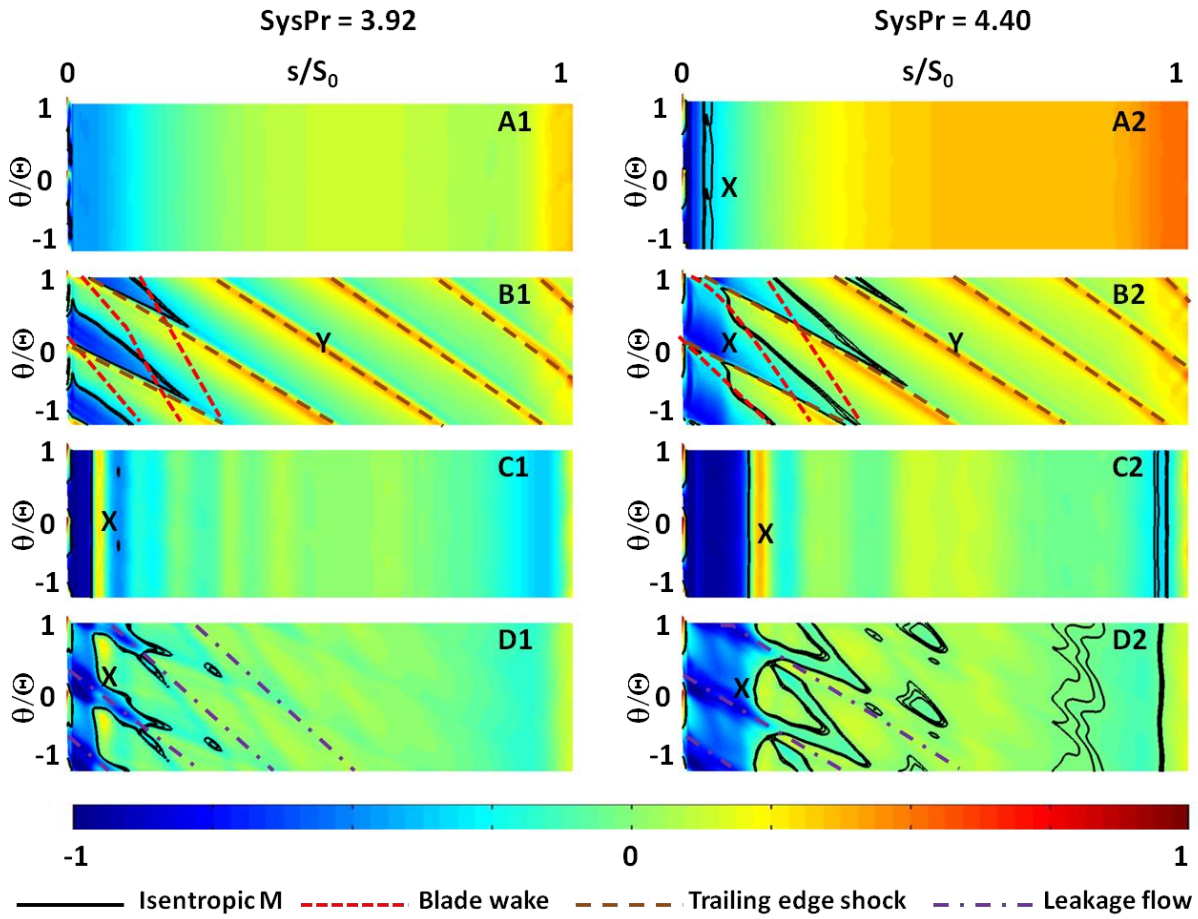

Figure 4.7. LOCAL CP VALUES COMPUTED ON DIFFUSER CASING

At the higher system pressure ratio (SysPr = 4.40), the cases without a leakage flow (A2 and B2) show very different losses and pressure recovery. In the mixing-plane case (A2), the loss remains roughly constant after the mixing-plane since there is little additional loss created in the diffuser. The removal of the mixing-plane in B2 shows a much larger rise in loss and this occurs within the first 1% of the diffuser due to the additional shock loss from the pressure-side arm of the rotor trailing-edge shock (as discussed earlier). Previously, a casing side normal shock development was seen for higher system pressure ratio, SysPr = 4.40. For these cases, the CP values initially drop due to the rapid flow expansion (at high flow turning) prior to the normal shock wave on the diffuser casing. The position of the casing shock (marked as K) in Figure 4.8, and this shows the shock strength increases significantly with the introduction of the leakage flow.

Having established the flow features that affect the flow interactions between rotor and the diffuser, a detailed look into the propagation of the leakage flow, blade wakes and trailing edge shocks into the diffuser is made. Figure 4.9 depicts the slice planes (A to E)

along which diffuser casing side flow features will be visualised. Figure 4.10 plots the entropy and meridional Mach number contours along slice planes A to E for test-case D1 (i.e. at SysPr = 3.92). At slice plane A, the blade wakes (labelled as 'W') and the leakage flow jet (labelled as 'L') can be clearly observed as regions of high entropy. The leakage jet (L) can also be seen as a region of high meridional Mach number plot. The generation of entropy in the shearing on both (above and below) side of the leakage flow can be observed. The trailing edge shock (labelled as red dotted line) can be seen in the meridional Mach number plot and its location is very close to the corresponding location of the blade wake on entropy generation plot. Moving downstream into the slice plane B, the blade wake (seen in the entropy generation plot) starts to move towards the negative pitchwise direction due to the presence of swirl. At the same time, the wake structure becomes more diffused due to the mixing of the wake.

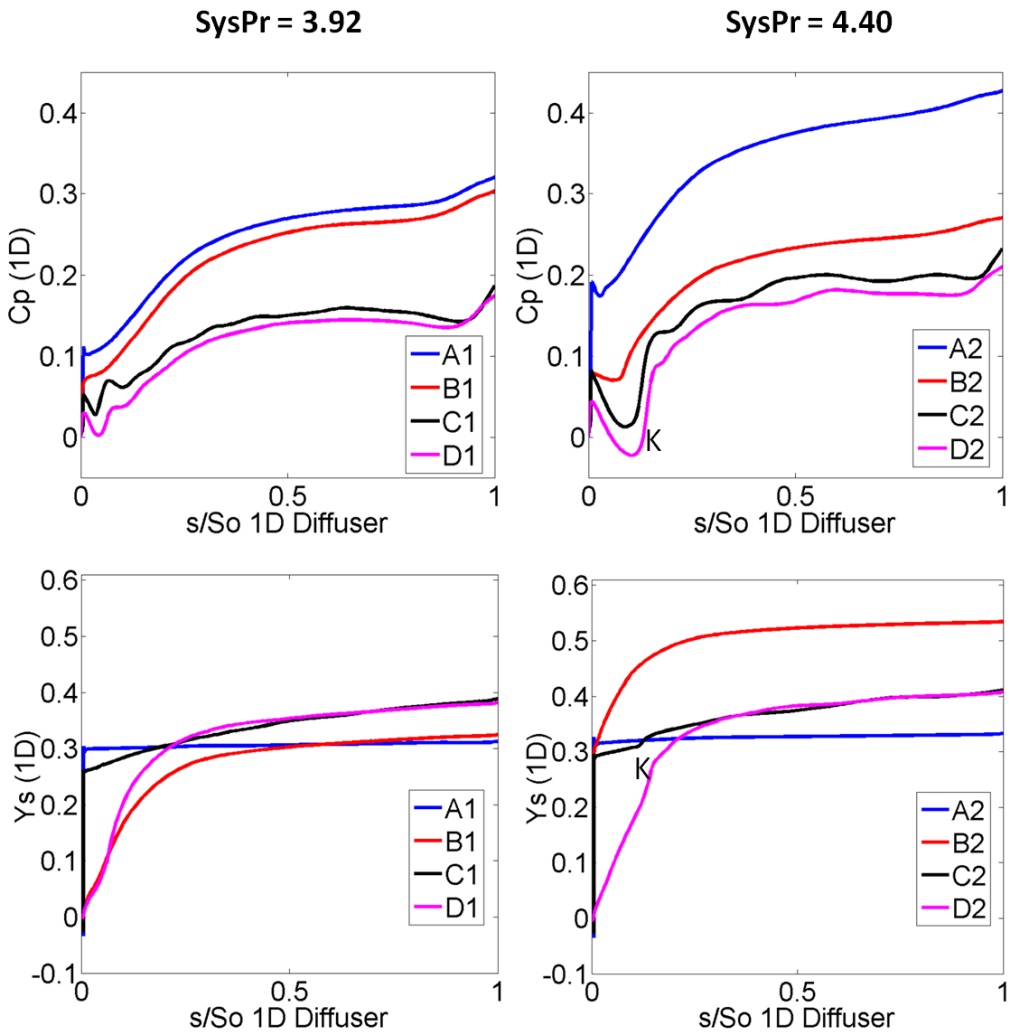

Figure 4.8. 1D PERFORMANCE FACTORS ALONG DIFFUSER LENGTH

By the time the flow reaches the slice plane C, the wake (W) has nearly mixed out. Keeping a note of the different orientation of the leakage flow shearing on top and bottom sides, the flow starts to develop into a leakage vortex at plane C. At the same time, the leakage flow starts to move closer to the trailing edge shock thereby reducing its strength near the diffuser casing. The strength of the leakage flow is reduced considerably (as indicated by the meridional Mach number); this is possibly due to the mild casing side normal shock which exists in between slice planes B and C (refer to Figure 4.6 for details). It can noticed that the wake mixing occurs rapidly whereas the leakage flow and trailing edge shocks have an influence over a much larger length of the diffuser casing side flow.

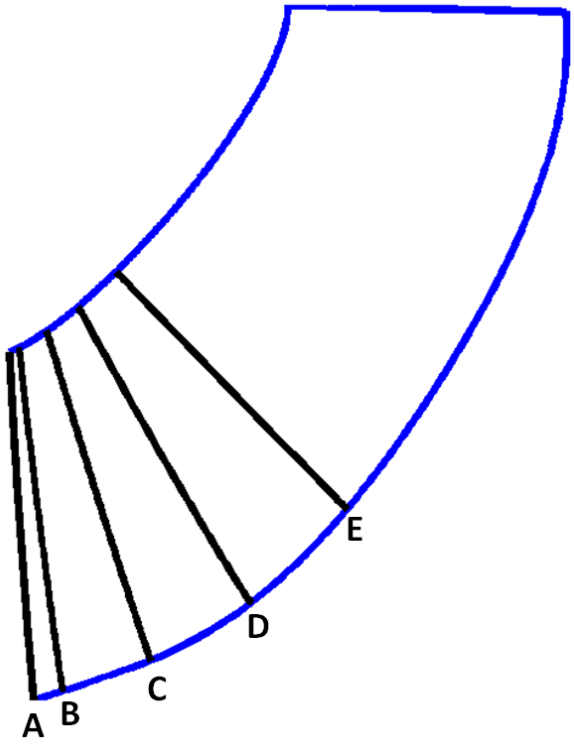

FIGURE 4.9. POSITION OF SLICE PLANES ALONG THE DIFFUSER FLOW

Moving further downstream into the slice plane D, the blade wakes are barely visible in the entropy generation contours. At slice plane E, the leakage flow (now a vortex) has crossed the diffuser passage width and reaches above the adjacent trailing edge shock wave. This second overlap further reduces the strength of the trailing edge shock near the casing wall. Figure 4.11 plots the similar normalized entropy generation and meridional Mach number contour plot along slice planes A to E for test-case D2 (SysPr = 4.40). Comparing the corresponding flow features in Figure 4.10 and Figure 4.11, it can observe that the

development and mixing of the rotor flow features is relatively unchanged when the pressure ratio is increased.

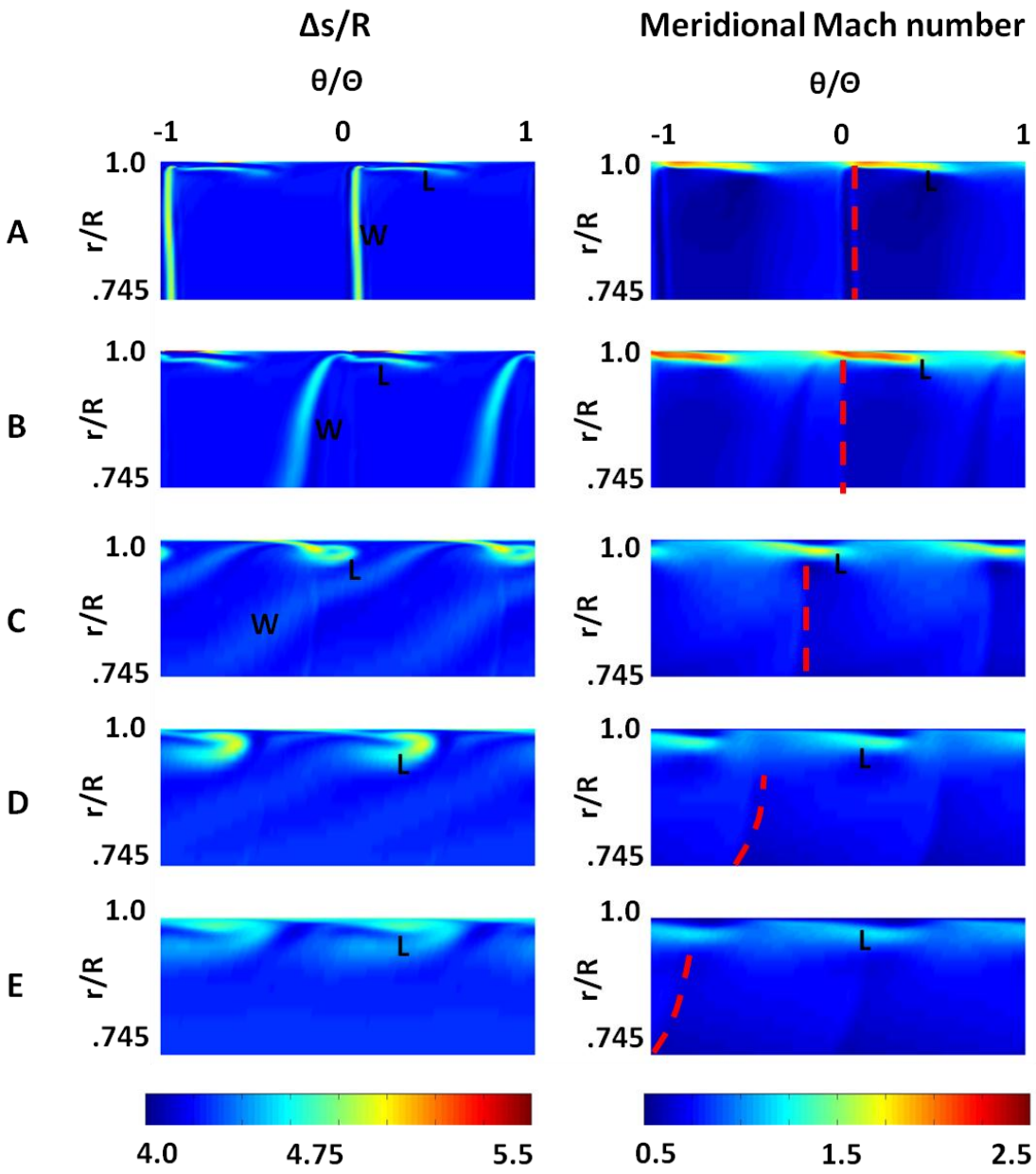

FIGURE 4.10. SLICE PLANES OF NORMALIZED ENTROPY AND MERIDIONAL MACH NUMBER FOR TEST-CASE D1 (SYSPR = 3.92)

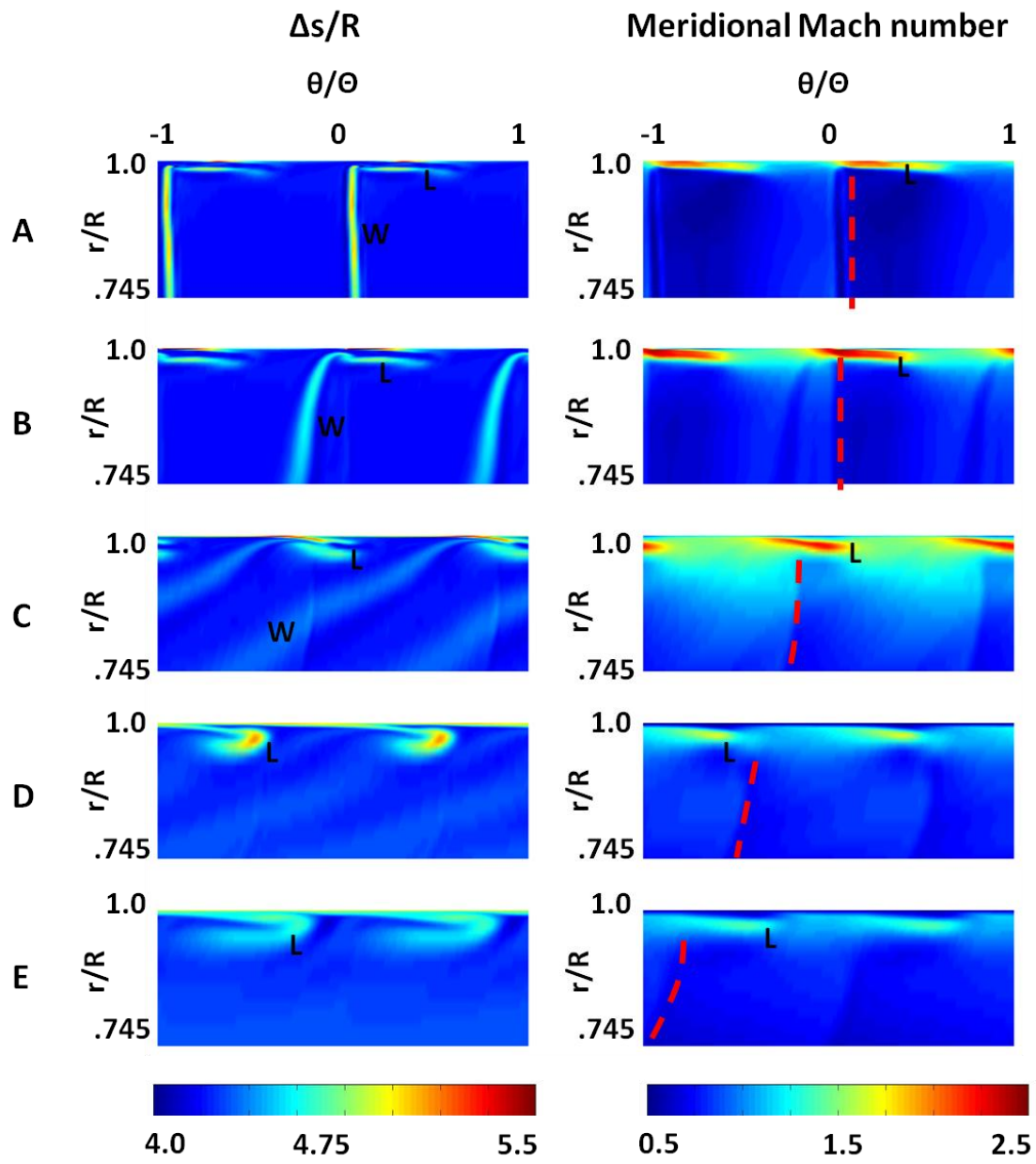

FIGURE 4.11. SLICE PLANES OF NORMALIZED ENTROPY AND MERIDIONAL MACH NUMBER FOR TEST-CASE D2 (SYSPR = 4.40)

4.3 Conclusions

Different sources of coupling between rotor and its axial-radial exhaust diffuser have been listed and their individual contribution towards the coupling has been discussed in detail. It has been shown that both the rotor and the diffuser are highly coupled such that the performance of one component is dependent on the other. The following flow features have been found to contribute to the coupling between the two components:

- Circumferential flow non-uniformities in the rotor exit flow

- Rotor trailing edge shocks
- Presence of a tip leakage flow

The study revealed that the majority of the entropy rise across the diffuser is a result of trailing-edge shocks and the mixing loss incurred due to non-uniformities in the rotor exit flow (such as from wakes and tip leakage flows). For cases without a leakage flow, trailing-edge shocks were found to greatly influence the unsteady pressure field on the diffuser casing. The presence of a leakage flow virtually eliminated this effect, by off-loading the rotor tip and reducing the trailing-edge shock strength. In most cases, mixing of flow features in the diffuser generated similar losses if mixed upstream of the diffuser across a mixing-plane, or within the diffuser.

5: Investigation of casing side flow interactions

Chapter Outline:

This chapter discusses an investigation of tip leakage flows within the LSB passage and diffuser. The interaction of leakage flows with flow features such as blade wakes, rotor trailing edge shocks, passage shock has been explored in chapter 4. This chapter further investigates the phenomena that lead to an increase in stagnation temperature of the leakage flow. The chapter ends by exploring the design space of these flow features while modifying the rotor 'hade' angle and determines the changes in the rotor-diffuser performance factors at different rotor hade angles.

5.1 Introduction

Fluid elements passing through the rotor tip gap will experience an unsteady pressure field which tends to increase their stagnation temperature in the absolute frame of reference, as observed by (Thorpe, et al. 2007) in HP gas turbine blades. This is referred to as a local 'pumping effect', and is responsible for the depletion of the work extraction capability of the rotor. A similar phenomenon was observed in this project, and this will be discussed in the first part of this chapter.

The present chapter investigates the effect on diffuser and rotor performance factors by modifying the basic over-tip casing shape. Since the reverse cambered LP turbine rotor blades tip are thin, there is little scope for using a sophisticated tip gap shape such as squealer fins employed within high pressure turbine rotor tips. With reducing hub to tip ratios, the only possible way to explore the design is to vary the tip gap size or change the casing shape such as through variations in flare angle (or 'hade angle'). Changes in casing shape are dealt with in more detail in the next chapter and the present chapter focuses only on the effects of hade angle.

5.2 Temperature rise within tip leakage flow

It is useful to determine how the presence of a leakage flow affects the rotor work output directly. Using test-case D1 from chapter 4, consider a plane within the rotor passage flow at 99.50% spanwise location (tip gap = 1% span) in Figure 5.1. The contours of relative yaw

give the sense of direction of the leakage flow with respect to the main passage flow. By tracking the relative yaw angle of flow near to the suction side of rotor trailing edge, the leakage flow can be identified. This flow is being ejected out of the tip gap at a relative yaw angle close to 0^o. Correspondingly the local absolute stagnation temperature values are also reaching high values in the same region signifying the high energy of the leakage flow. However, these values of stagnation temperature are far above the rotor inlet stagnation temperature of 340K. Therefore, additional work processes are acting within the tip gap that are acting as an additional energy source for the tip gap flow.

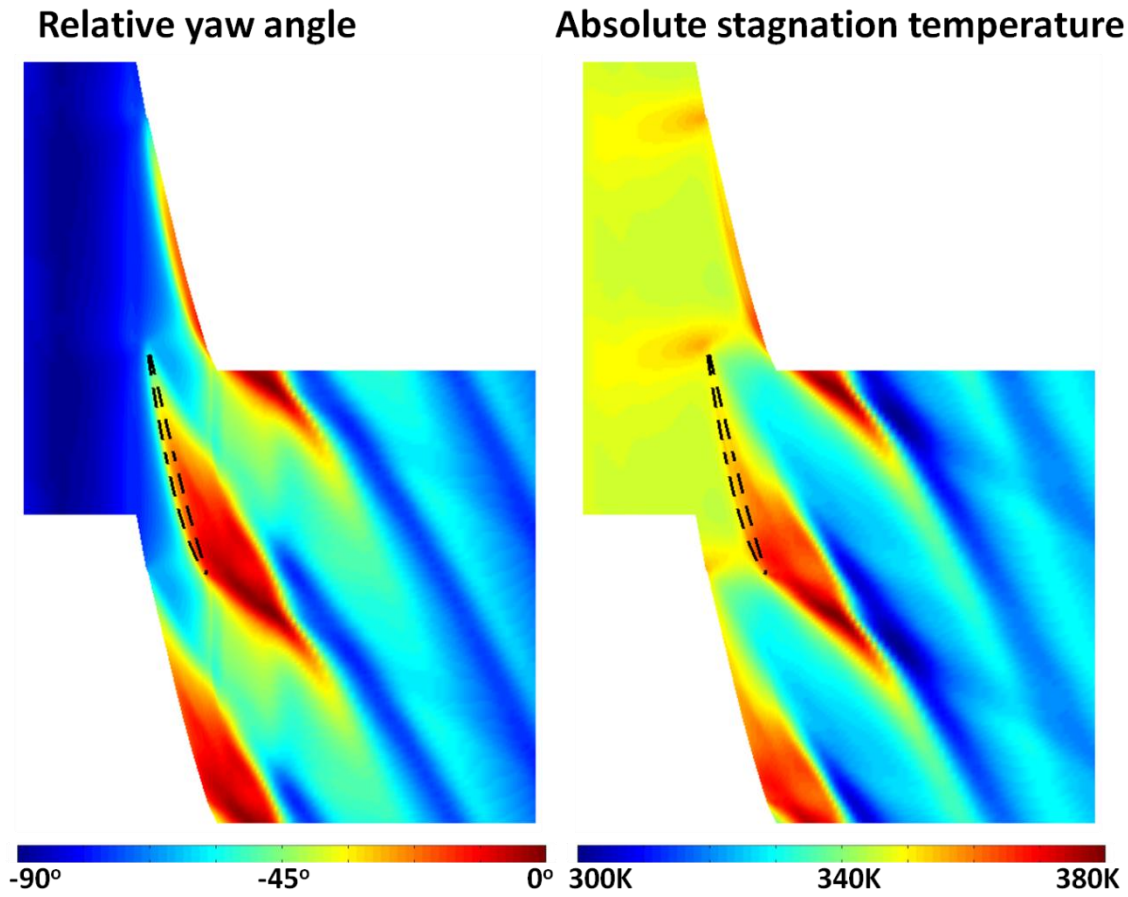

FIGURE 5.1. ROTOR PASSAGE SLICE PLANES OF RELATIVE YAW ANGLE AND ABSOLUTE STAGNATION TEMPERATURE AT 99.50% SPAN

Figure 5.2 depicts the velocity triangles within a rotor tip gap for the last stage LP turbine. Near inlet (labelled as 1), the flow enters at a very high incidence as directed by the nearby primary passage flow. Moving along the blade chord, the pressure difference between suction and pressure side increases which directly affects the velocity triangle at a position t (see Figure 5.2). The absolute flow velocity at position 't' can reach high values

depending on various factors such as radii of streamlines, tip gap shape and viscous dissipation inside the tip gap.

Considering an inviscid flow with no heat conduction for a fluid element travelling within the rotor tip gap. Looking at this particle in an absolute frame of reference, the rate of change of its stagnation enthalpy is dependent on the rate of change of static pressure and density at a fixed position (say t) as shown below:

$$\frac{\mathrm{Dho}}{\mathrm{Dt}} = \frac{1}{\rho}\frac{\partial \mathrm{P}}{\partial \mathrm{t}} \qquad \textbf{(5.1)}$$

Since the flow calculations are steady in relation to the moving blade row, the rate of change of static pressure can be defined in terms of temporal (spatial) pressure gradient in absolute frame as:

$$\frac{\partial \mathrm{P}}{\partial \mathrm{t}} = \omega\frac{\partial \mathrm{P}}{\partial \theta} = \omega \mathrm{r}\frac{\partial \mathrm{P}}{\mathrm{r}\,\partial \theta} \qquad \textbf{(5.2)}$$

where ω is the rotational speed of the rotor and direction of θ is specified in Figure 5.2. Balancing angular momentum of the fluid particle (and neglecting viscous stresses) passing through a tip gap:

$$\omega\frac{\mathrm{r}}{\rho}\frac{\partial \mathrm{P}}{\mathrm{r}\,\partial \theta} = \omega\frac{\mathrm{d}(\mathrm{r}\mathrm{V}_\theta)}{\mathrm{dt}} \qquad \textbf{(5.3)}$$

Combining above three equations:

$$\frac{\mathrm{dho}}{\mathrm{dt}} = \omega\frac{\mathrm{d}(\mathrm{r}\mathrm{V}_\theta)}{\mathrm{dt}} = \frac{\mathrm{d}(\omega \mathrm{r}\mathrm{V}_\theta)}{\mathrm{dt}} = \frac{\mathrm{d}(\mathrm{u}\mathrm{V}_\theta)}{\mathrm{dt}} \qquad \textbf{(5.4)}$$

which is essentially a rothalpy equation for the fluid particle. Thus,

$$\Delta \mathrm{ho} = \int \frac{\mathrm{dho}}{\mathrm{dt}}\,\mathrm{dt} = \Delta(\mathrm{u}\mathrm{V}_\theta) \qquad \textbf{(5.5)}$$

And stagnation temperature rise across a tip gap can be calculated by:

$$\Delta \mathrm{To} = \frac{\Delta \mathrm{ho}}{\mathrm{c_p}} = \frac{\Delta(\mathrm{u}\mathrm{V}_\theta)}{\mathrm{c_p}} = \frac{\Delta(\mathrm{ua}\mathrm{M}_\theta)}{\mathrm{c_p}} \qquad \textbf{(5.6)}$$

where a is the sonic speed and Mθ is the tangential Mach number of the fluid particle. Although this derivation gives the isentropic change in stagnation temperature, the viscous effects do not have a significant effect on temperature change (Miller and Denton 2012) and (Thorpe, et al. 2007).

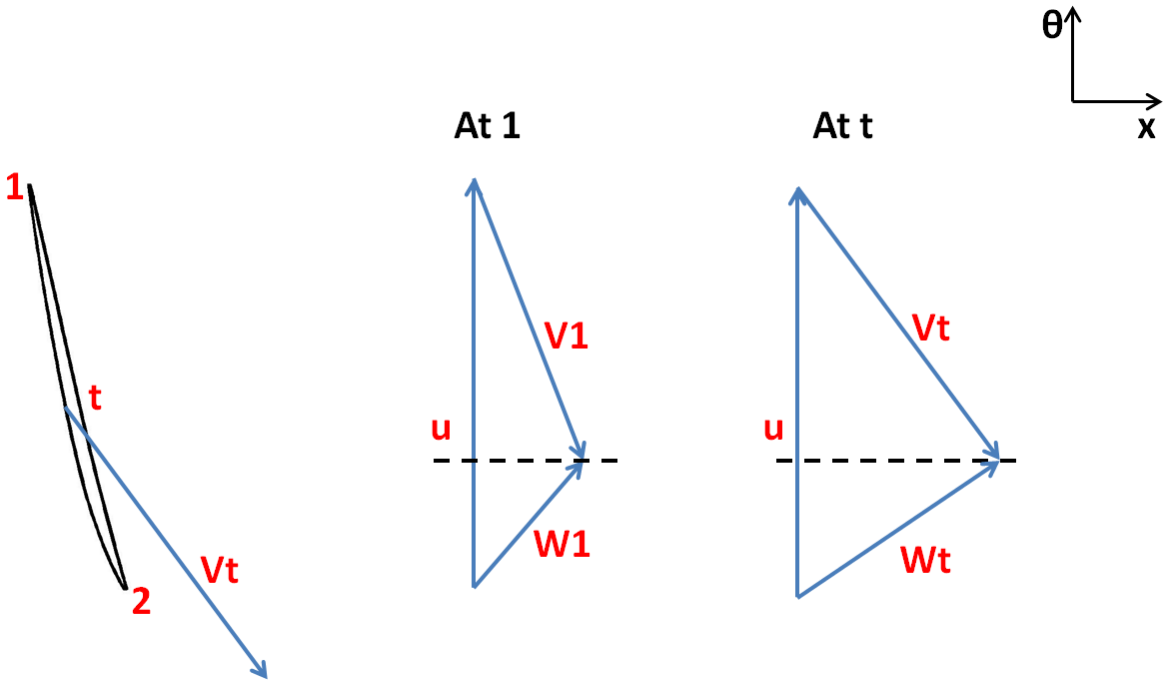

FIGURE 5.2. VELOCITY TRIANGLES INSIDE THE ROTOR TIP GAP

Figure 5.3 plots the change in stagnation temperature of fluid particles along the mid-gap camber line. For simplicity, rather than computing the change in total temperature along a particle path line, the change in total temperature is calculated with respect to a pitchwise average absolute total temperature at the rotor inlet. Thus, an increasing difference in predictions can be seen between values calculated using the rothalpy equation and CFD predictions. Here, three observations can be made: first, the change in stagnation temperature is similar for both methods throughout the blade chord. It means that the primary work process causing the increase in tip gap temperature is the work done by the rotor on the tip gap flow (referred to as 'pumping effect'); second, the change in stagnation temperature is nearly the same at both tested system pressure ratios. This means that the work processes are dependent only on the change in particle whirl and its radii of rotation. Third, the peak of the graph lies close to 85% of the blade chord, signifying a region of high tangential Mach number. It means that any effort to reduce the rise in tip gap temperature should focus on reducing the tangential Mach number in the tip gap. If the rotor blade

profile is fixed, the tangential Mach number can be modified by varying the tip gap radii (modify the rotor casing shape) or by changing the tip gap height. The following section describes the effects of change in the rotor casing shape.

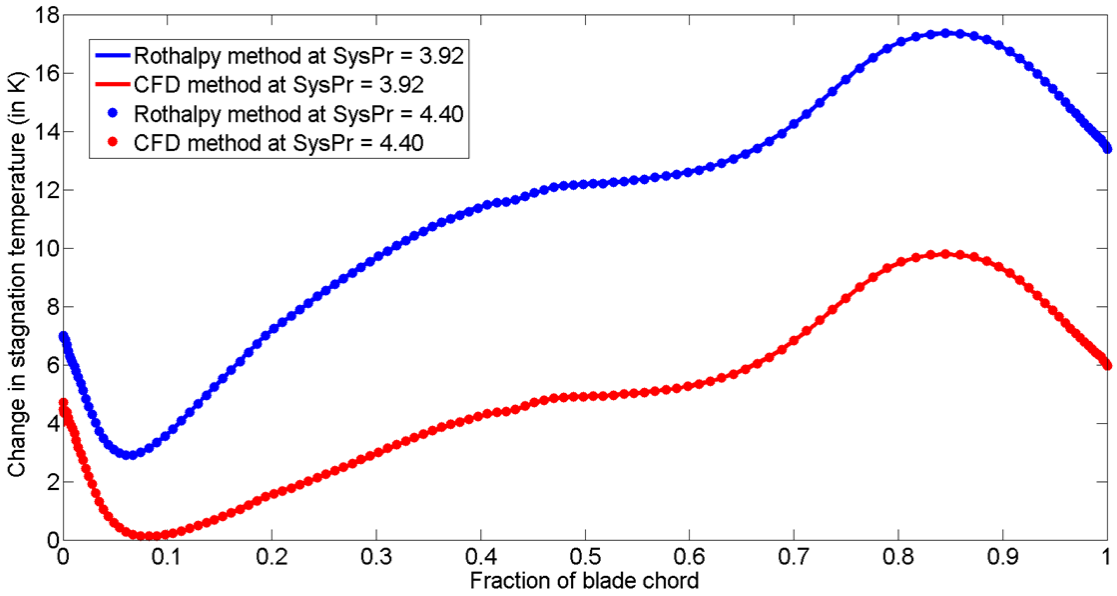

Figure 5.3. RISE IN ABSOLUTE STAGNATION TEMPERATURE OF THE TIP GAP FLOW ALONG ITS CHORD

5.3 Hade angle variation

The effect of casing hade was investigated to gather knowledge of its effects on the rotor and diffuser performance. The casing above the rotor blade was modified as depicted in Figure 5.4. The casing point above the rotor trailing edge was fixed, and the hade was varied by moving the radial position of the leading-edge point. The diffuser casing was kept fixed in order to create a discontinuity in curvature at the junction of the rotor-diffuser casing line, with the aim of producing a Prandtl-Meyer compression in this region. The rotor blade tip was modified to match the required tip gap of 1% of the span (fraction of radii) at each chord-wise position ensuring a fixed leakage area along the chord. All tests cases were run with and without tip gap flow.

Figure 5.5 plots the diffuser performance factors for different hade angles. It reveals that the diffuser CP is highly enhanced with an increase in the hade angle. Also, the total pressure loss (Y_s) is relatively unaffected by hade. The changes in CP are therefore a consequence of changes in diffuser inviscid loading ($1-\zeta$).

Figure 5.9 plots the pitchwise averaged radial profiles of static and total pressure and stagnation temperature from 60-100% span at the diffuser inlet, for the cases with and without leakage flow. For simplicity, only three hade angles are provided. The results show that the effect of hade is to greatly reduce the static pressure in the upper portion of the span, increasing the work-output in this region significantly. For cases with a tip gap, the results show a large reduction in the stagnation pressure and temperature in the region of the leakage flow ~99% span with the rise in the hade angle. Figure 5.10 plots the pitchwise average Mach number for two different hade angles and reveals the reduction in the casing side flow Mach number as hade angle is increased. The presence of the compression corner introduced with high hade angles reduces the casing side Mach number and aids the diffusion of the flow, thus raising the diffuser pressure recovery.

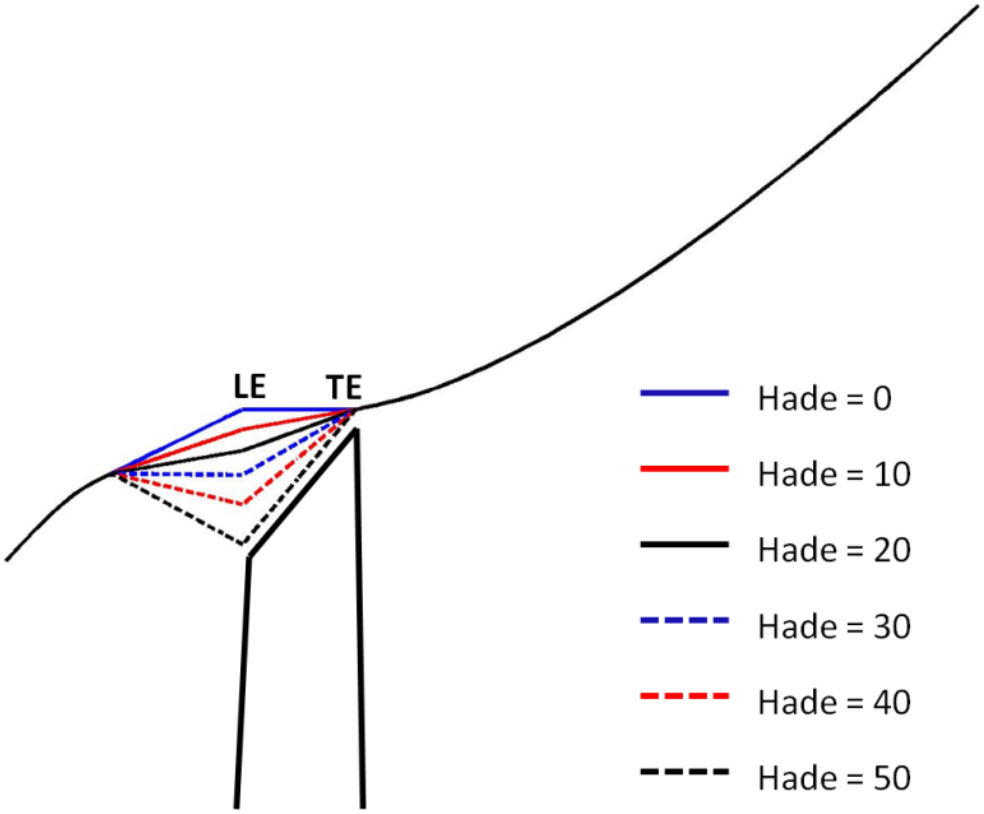

Figure 5.4. ROTOR HADE ANGLES CONFIGURATIONS

Figure 5.5. DIFFUSER PERFORMANCE FACTORS FOR HADE ANGLE VARIATION

Figure 5.11 plots the stagnation temperature within the tip gap. The data shows that increasing the hade angle also reduces the leakage flow 'pumping effect', as identified by a reduction in tip-flow temperature and tangential Mach number.

Figure 5.12 shows the variation in rotor total-to-total efficiency and system total-to-static efficiency (as defined previously in Section 2.0 of Chapter 2). For cases with a leakage flow the overall system performance is significantly improved as hade increases; from 0-40^{o} hade, the system efficiency rises by 0.65% for the case without tip leakage and by 2% for

the case with tip leakage. It is interesting to note that hade has a greater benefit on the system when there is a leakage flow present, and this is a likely result of the twin effects of the increased pressure recovery and increased rotor work output due to the reduction in tip pumping as hade angle increases. For hade angles greater than about 40^o the performance benefit is much less apparent, and indeed there will likely be a practical limits (blade axial movement, vibrations, water droplet erosion, etc) which will determine the optimum hade. Superimposed on the same plot are system total-to-static efficiencies, for cases both with and without tip gap, for calculations with a mixing plane (MP) interface between rotor and diffuser. For simplicity, values up to hade = 40^o are plotted. The system efficiency values remain unchanged when the rotor exit flow (with or without leakage flow) is mixed out completely. The results are in line with the results from chapter 4 where the system total-to-static efficiency is not greatly affected by the circumferential non-uniformities in the flow. This means that the tip pumping has a negligible effect on the diffuser performance. Hence, by introducing a hade angle to the rotor casing, the diffuser performance in the present case is enhanced only due to the presence of a compression corner at the diffuser inlet.

Figure 5.6 plots the fraction of leakage mass flow passing through a rotor tip clearance at different hade angles. The results reveal a drop in the leakage mass flow from hade = 0^o to 50^o. Figure 5.7 gives the leakage flow mass flux for two hade angles in the meridional plane. The data shows that at hade = 0^o , leakage flow is mainly passing close to the rotor trailing edge area. However, at hade = 50^o, the mass flux reduces considerably and redistributes towards the leading edge. Apart from changing the leakage flow structure, hade angle must be modifying the blade loading distribution as well. Figure 5.8 plots the blade loading as difference in static pressure between blade pressure and suction surfaces for both without and with tip gap cases at hade angles 0^o, 30^o and 50^o. Two trends can be observed in this plot: first, increase in hade angle redistributes the blade loading where trailing edge near casing is off-loaded while away from casing is loaded more; second, increase in hade angle gives higher blade loading. The results show that hade has a big influence on the flow structure with the rotor, but surprisingly, it will be shown soon that the rotor performance remains same.

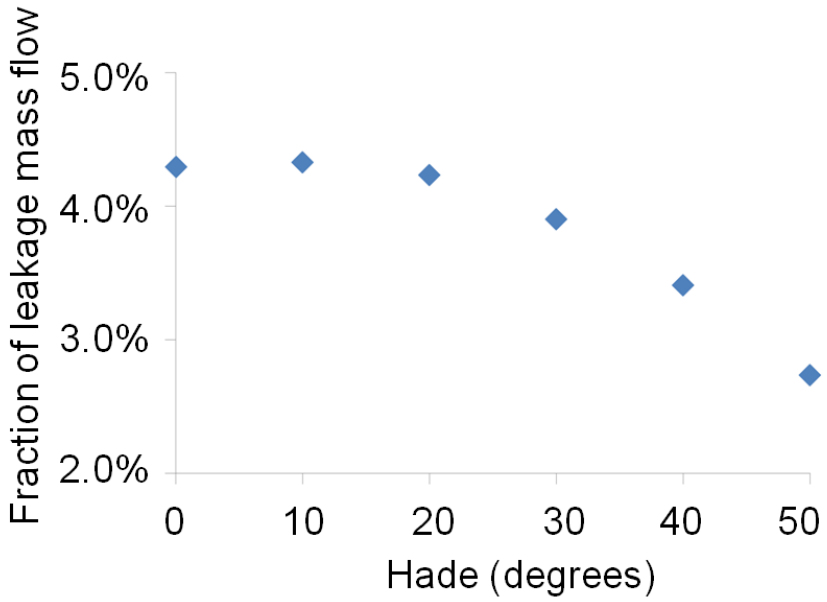

Figure 5.6. FRACTION OF LEAKAGE MASS FLOW PLOTTED AGAINST DIFFERENT HADE ANGLES SIGNIFYING HADE REDUCES LEAKAGE MASS FLOW

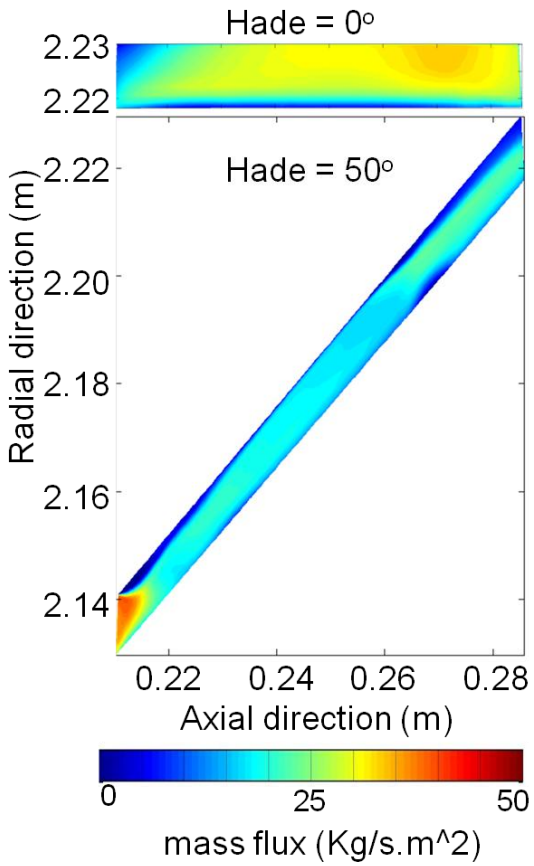

Figure 5.7. ROTOR TIP CLEARANCE LEAKAGE MASS FLUX IN THE MERIDIONAL PLANE FOR HADE ANGLES OF 0^o and 50^o

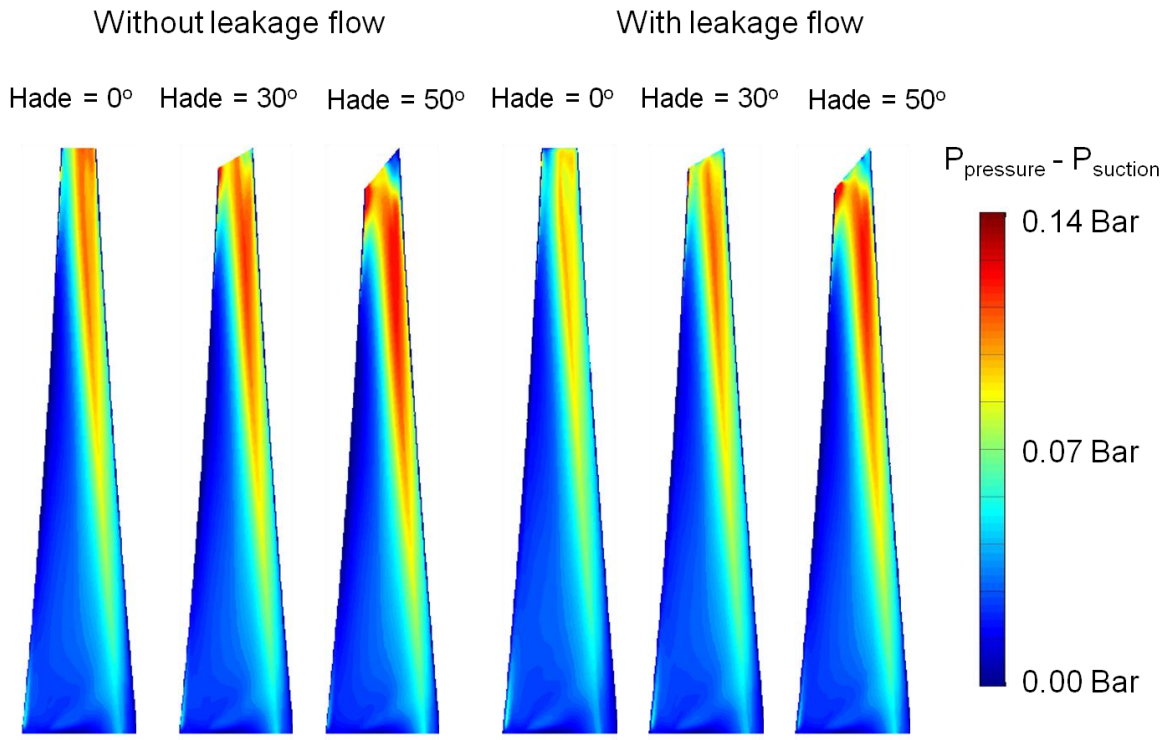

Figure 5.8. BLADE LOADING PLOTTED AS PRESSURE DIFFERENCE BETWEEN BLADE PRESSURE AND SUCTION SURFACES FOR WITH AND WITHOUT LEAKAGE FLOW AT DIFFERENT HADE ANGLES

Until now, a high stagnation temperature regions of tip leakage flow were observed (in Figure 5.1) and such localized stagnation temperature region forms due to the unsteady pressure field which can be affected by employing a haded rotor casing. Looking into the details of the flow features (namely tip leakage flow, blade wakes and trailing edge shocks) developing into the diffuser flow regime. The interaction mechanism between these flow features has been described earlier in the chapter 4. Figure 5.13 plots the stagnation temperature contour plot for two hade angles (0^o and 50^o) along various slice planes in a diffuser (as defined in Figure 9 of chapter 4). Comparing the two hade angles at slice plane A, the stagnation temperature of the leakage flow (labelled as 'L') is reduced well below 340K for hade angle 50^o. Moving along the slice planes B to E, the region of high stagnation temperature mixes out quickly in both cases where hade = 50^o yields a nearly uniform stagnation temperature flow field at slice plane E. The plots suggest that casing side compression corner at high hade angle helps to reduce the pumping effect on the leakage flow, and thus reduces the non-uniformity of stagnation temperature entering the diffuser.

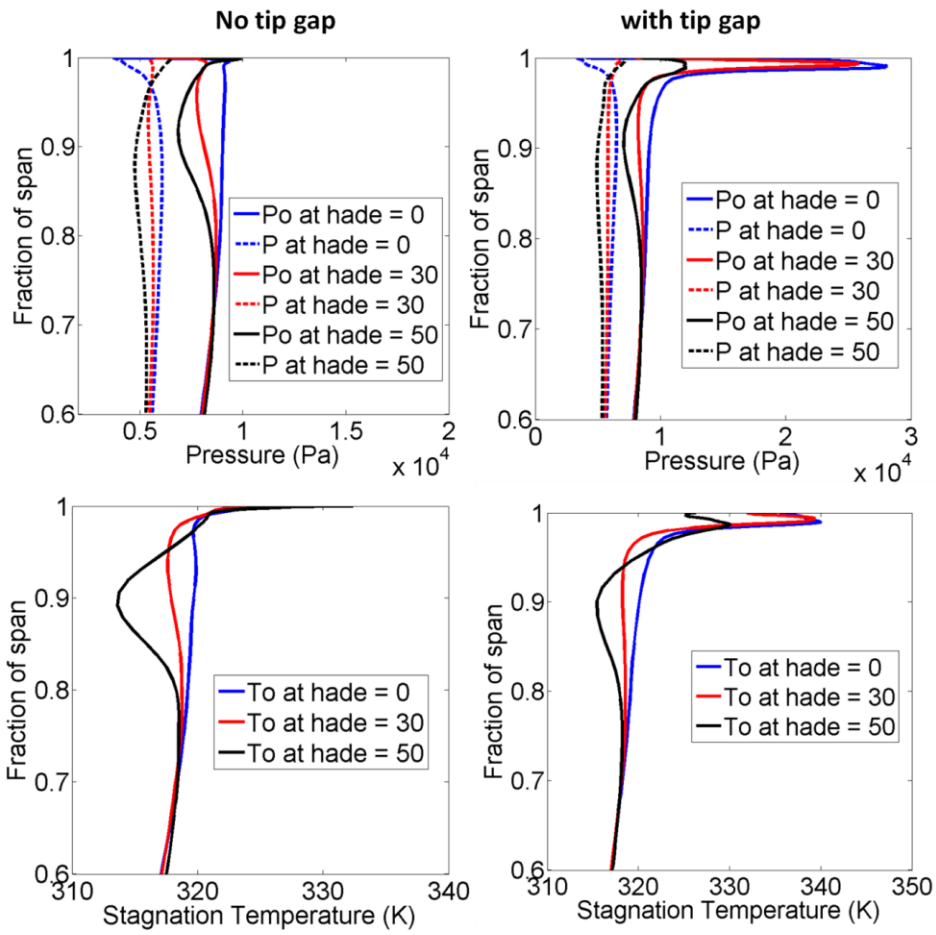

Figure 5.9. SPANWISE PRESSURE AND TEMPERATURE DISTRIBUTION AT ROTOR EXIT/DIFFUSER INLET

Figure 5.14 plots the normalized entropy (Δs/R) contour plot for two hade angles (0^o and 50^o) along various slice planes in a diffuser (as defined in Figure 9 of chapter 4). At slice plane A, the effects of haded rotor can be seen clearly. The inlet leakage flow has already developed into a clockwise rotating vortex. In contrast to the leakage jet for hade = 0^o case, the leakage flow at hade = 50^o quickly develops into a vortex and starts to interact with the nearby blade wake (labelled as 'W'). Moving downstream into the diffuser flow, the vortex mixes out rapidly producing entropy over a wider area near the diffuser casing walls. The leakage flow for hade = 0^o forms a vortex near slice plane D due to the mechanism explained earlier in the chapter 4. Thus, at slice plane D, while hade = 0^o leakage still develops into a vortex, the leakage vortex for hade = 50^o starts to diffuse further producing a more uniform flow field at slice plane E.

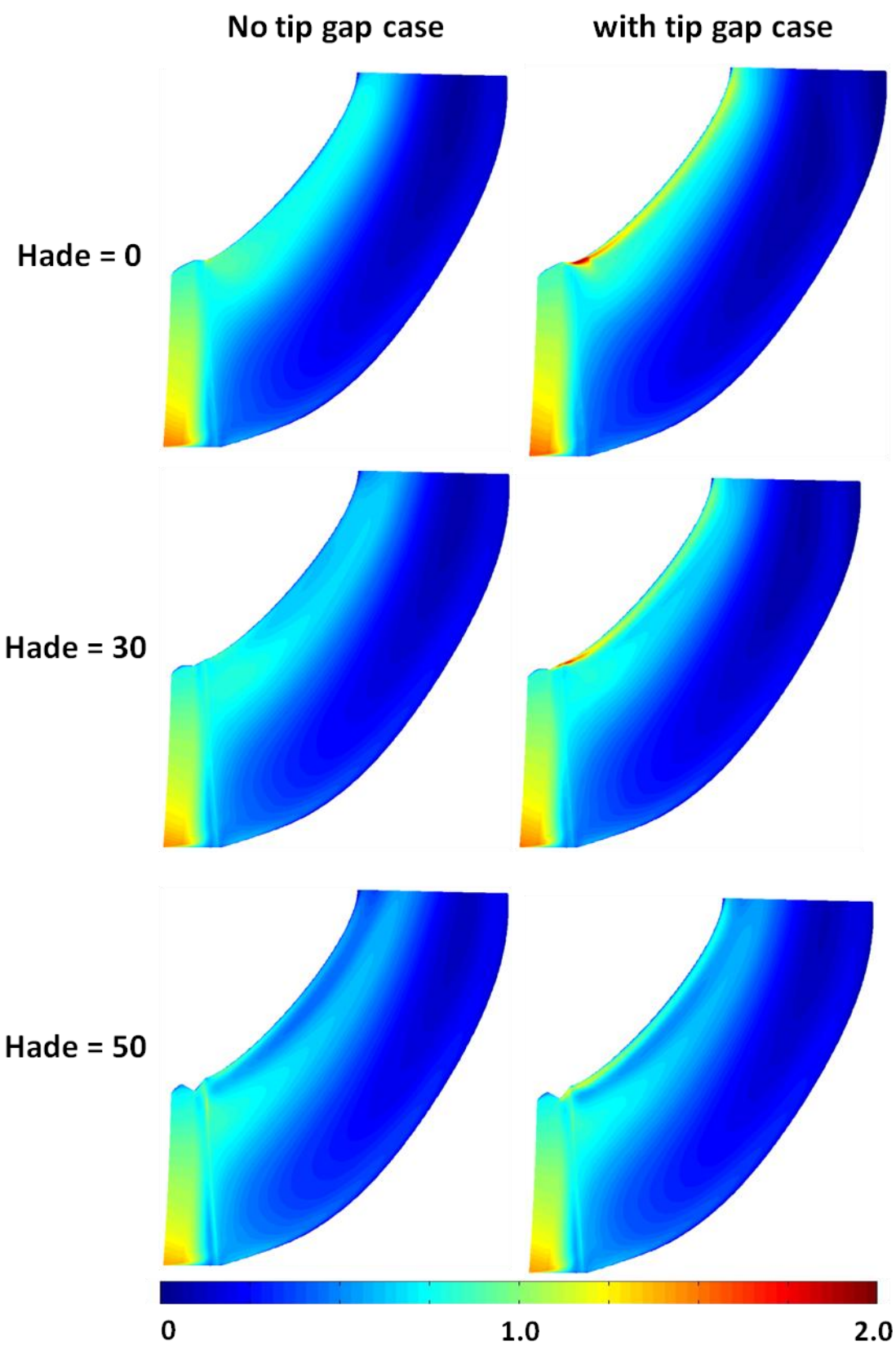

Figure 5.10. PITCHWISE ABSOLUTE MACH NUMBER FOR DIFFERENT HADE AND LEAKAGE FLOW CONFIGURATIONS

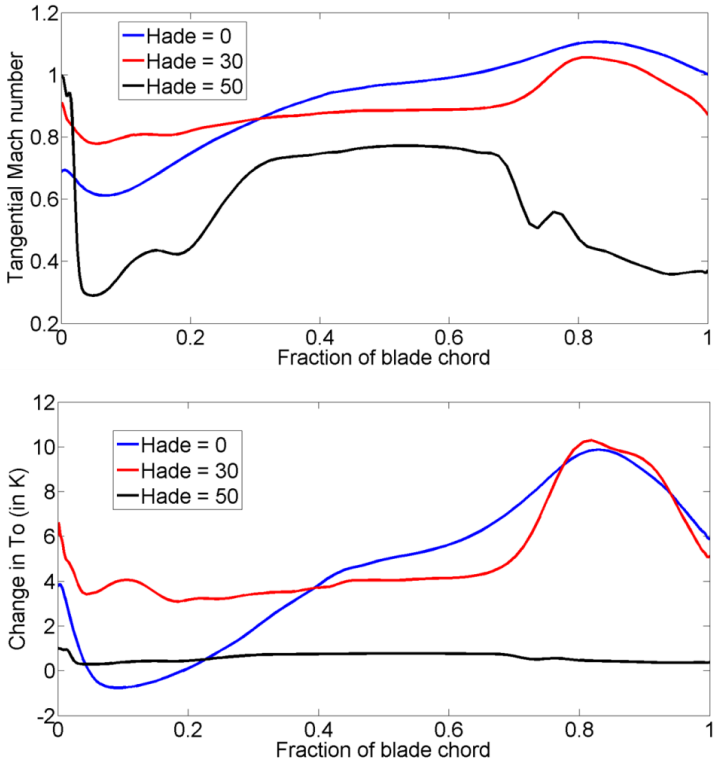

Figure 5.11. TANGETIAL MACH NUMBER AND RISE IN STAGNATION TEMPERATURE INSIDE BLADE TIP GAP

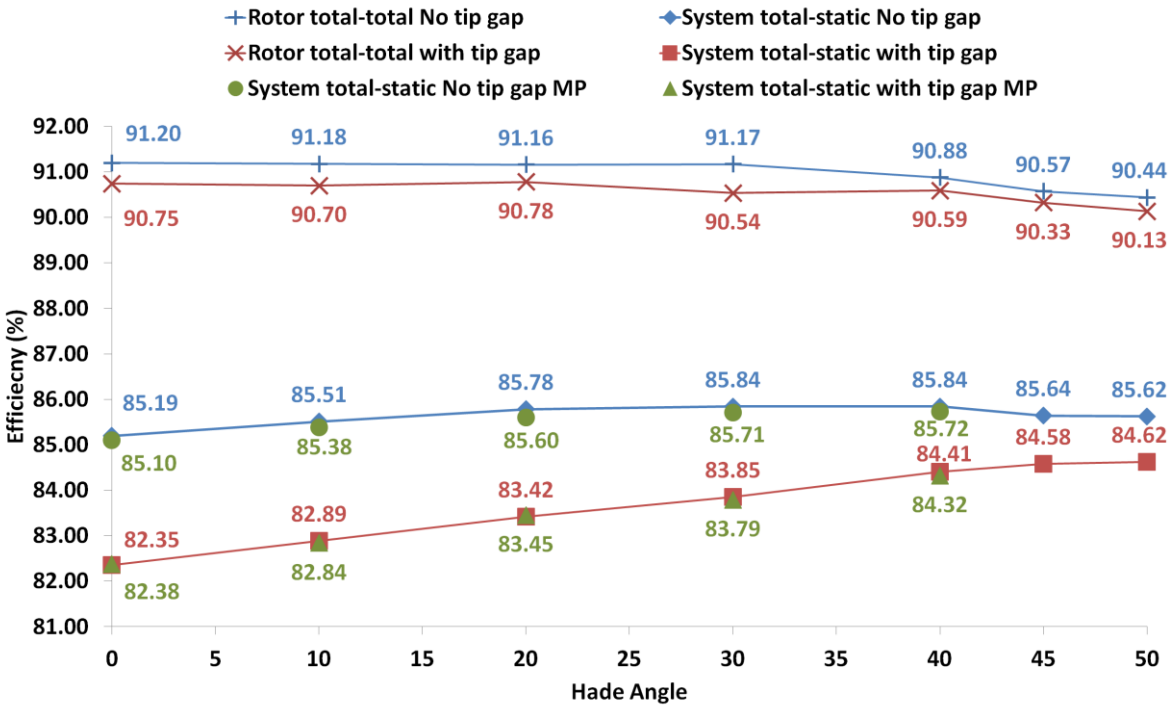

Figure 5.12. ROTOR AND SYSTEM EFFICIENCIES FOR VARIOUS HADE AND LEAKAGE FLOW CONFIGURATIONS

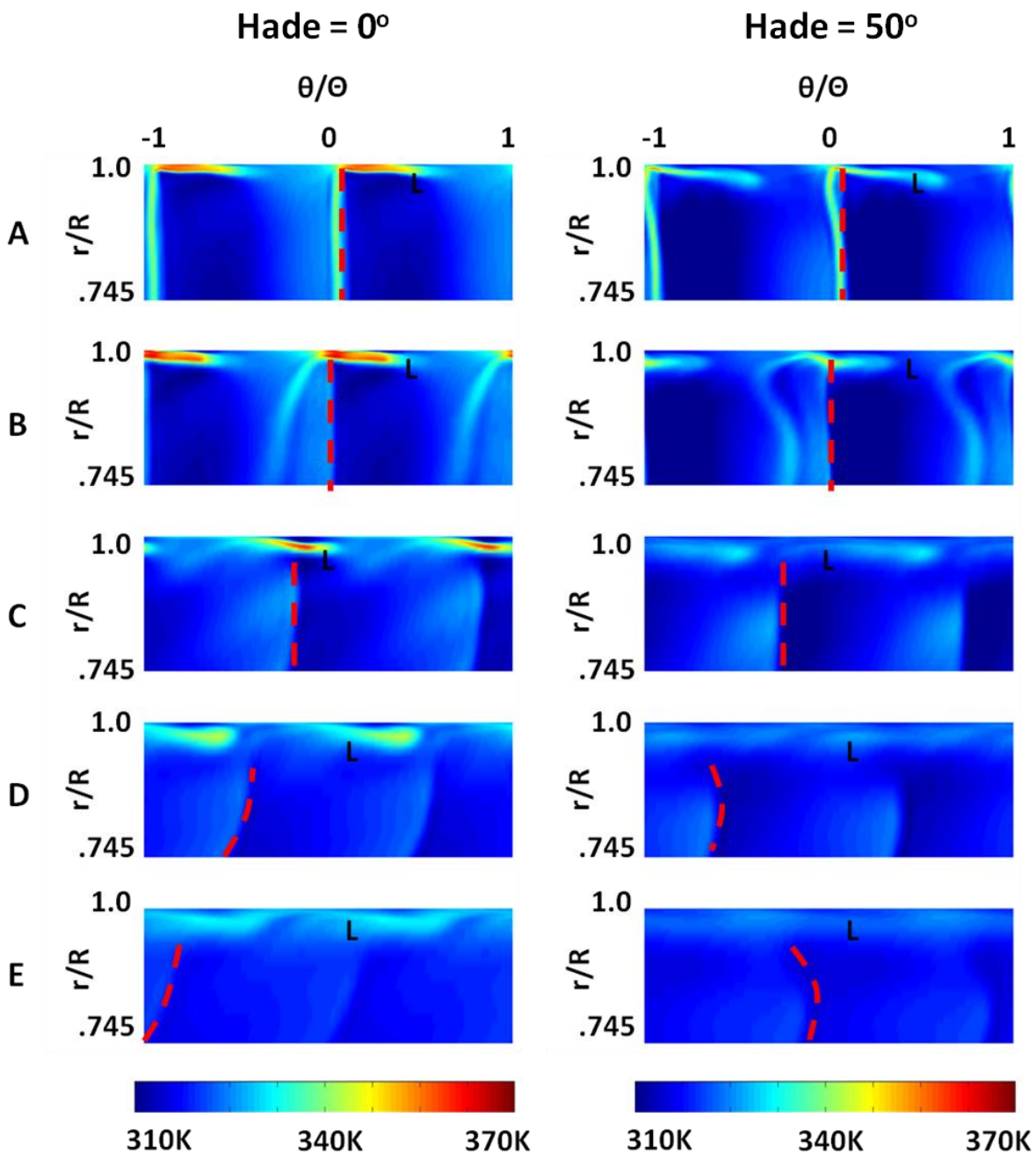

FIGURE 5.13. STAGNATION TEMPERATURE CONTOUR PLOT FOR DIFFERENT HADE ANGLES

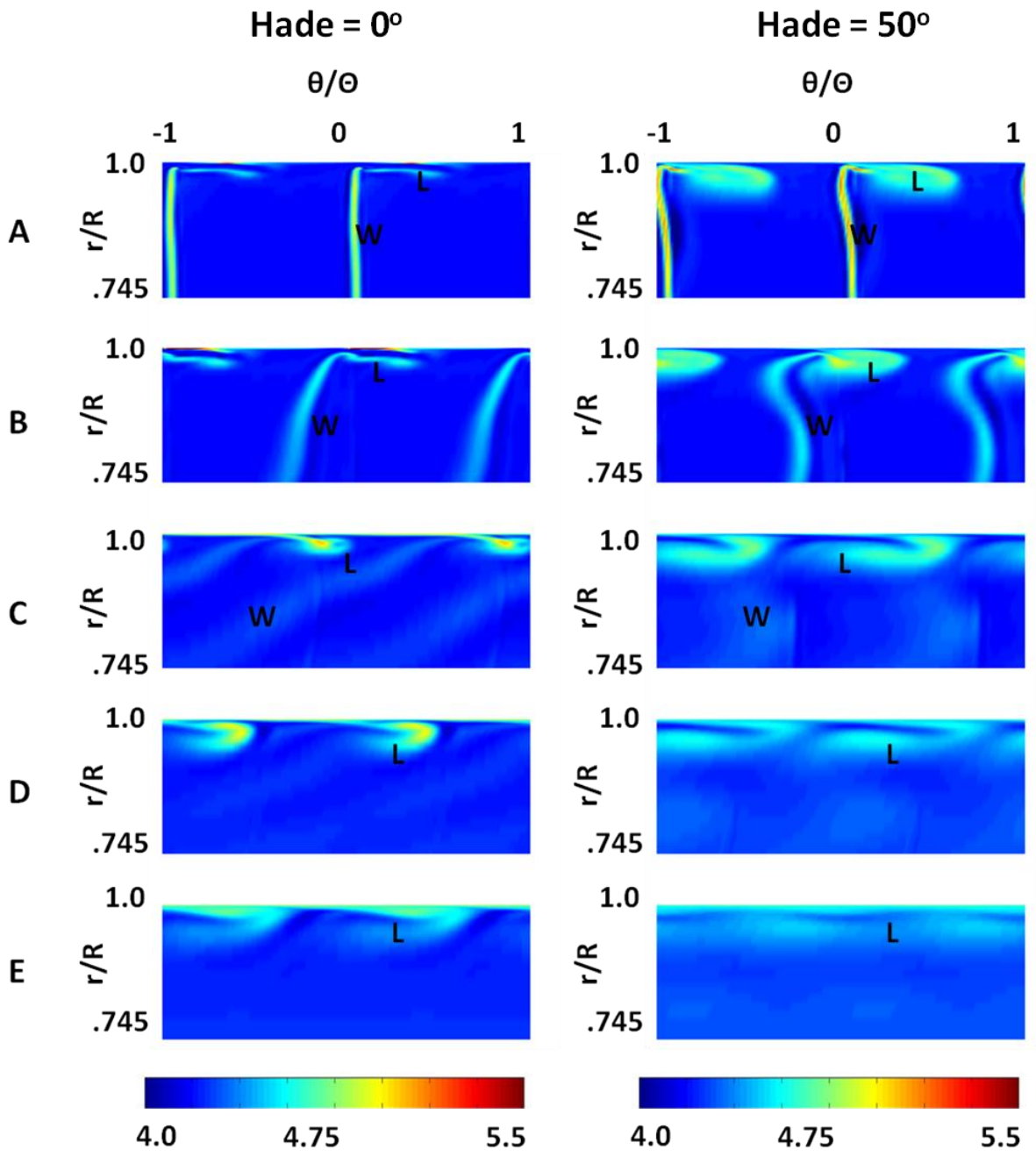

FIGURE 5.14. NORMALIZED ENTROPY (ΔS/R) CONTOUR PLOT FOR DIFFERENT HADE ANGLES

5.4 Conclusions

This chapter focused on the effects of leakage flows on the coupled rotor/diffuser performance and the effect of rotor casing shape (namely hade angle) on the coupled system performance. Significant stagnation temperature rises within the tip gap were observed due to the work done by the rotor on the leakage flow (‘pumping effect’). This mechanism reduced the work extraction capability of the rotor. The 'pumping effect' was reduced by

using a haded casing around the rotor. The study revealed that the diffuser pressure recovery can be enhanced by increasing the rotor casing hade angle without significant increases in the diffuser loss for hade angles up to ~40deg. Increasing hade angle also significantly increased the diffuser pressure recovery due to the influence of hade on the local pressure field at the exit of the rotor, and the combined effects led to large increases in overall system performance for cases with a leakage flow.

6: The effect of diffuser shape on system performance

Chapter Outline:

This chapter continues to investigate the effects of casing on LSB and diffuser performance while taking into account various possible diffuser shapes. The study starts with an investigation of the effects of several geometrical area ratios and aspect ratios on both the diffuser and system performance. This chapter further examines the effect of tip leakage flow on diffuser casing side flow by studying system performance factors under different tip gaps. The chapter ends by exploring how modifications in the rotor 'hade' angle changes the rotor-diffuser performance factors at different levels of overtip leakage flows.

6.1 Introduction

Previous chapters described the underlying flow features that affect the performance of the rotor and diffuser through various interactions. Up to now these studies have been examined only for a fixed diffuser geometry. This chapter explores how these interactions are affected by the choice of diffuser shape, and over-tip casing shape. The effects of area ratio (AR) and diffuser casing aspect ratio (S/H), as defined in chapter 3, on rotor-diffuser performance factors are discussed in the following section.

6.2 Effects of diffuser geometry

Figure 6.1 plots the diffuser performance factors for various diffuser geometrical configurations. Here, the diffuser casing aspect ratio (S/H) is varied between 0.4 (‘tight’ diffuser) to 1.2 (‘long’ diffuser). Each of these casing side configurations are tested at three geometrical area ratios (AR) of 1.0, 1.5 and 2.0. The attempt is to simulate the broad range of rotor exit flow conditions and flow diffusion rates that might occur within typical steam-turbine exhausts. It should be noted that geometrical area ratios will not be same as the flow diffusion area ratio due to the presence of highly non-uniform flow from hub to casing and changes in the blockage (ζ). These diffusers are tested at a fixed rotor tip gap of 1% span.

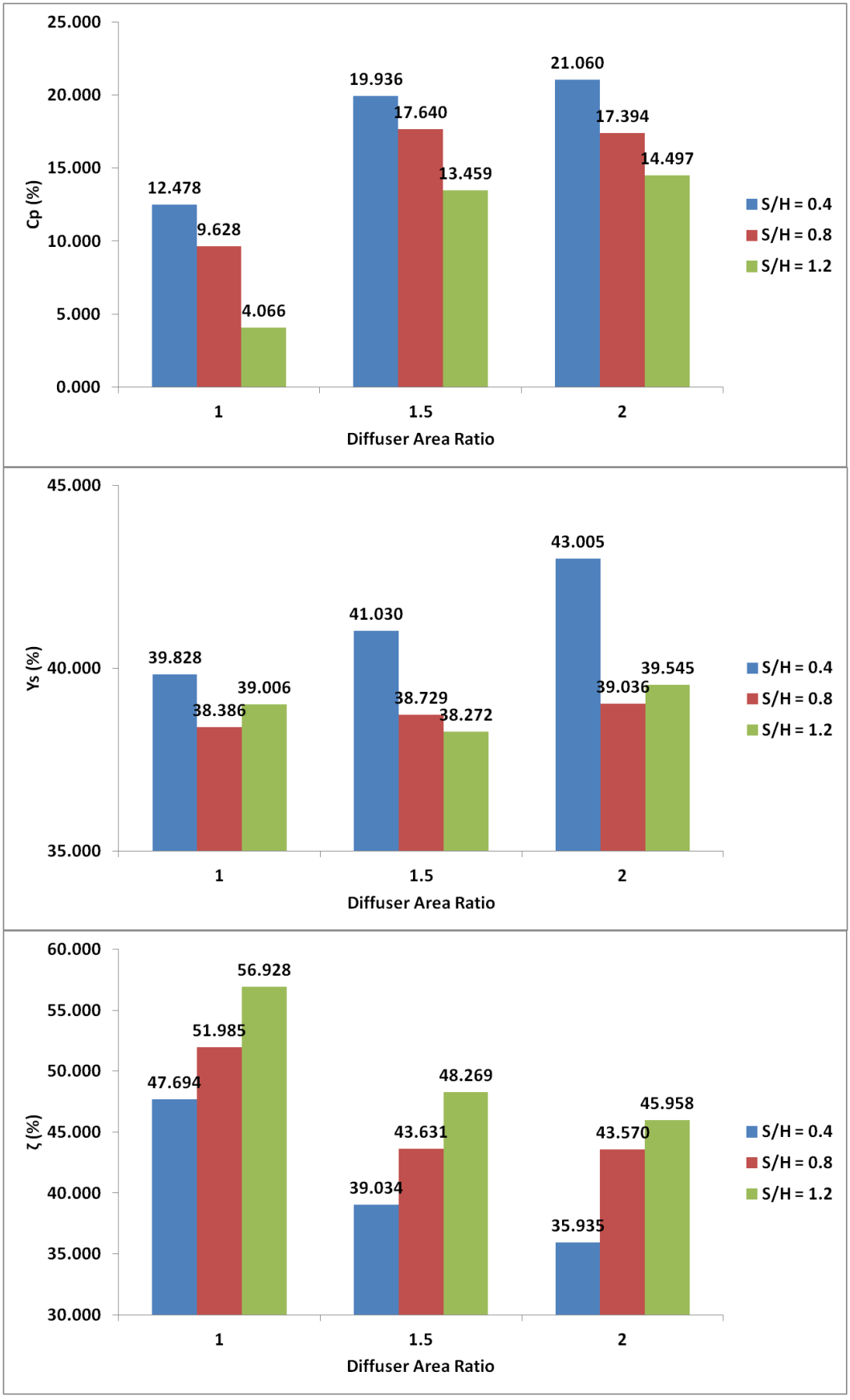

FIGURE 6.1. DIFFUSER PERFORMANCE FACTORS FOR VARIOUS S/H AND AREA RATIOS

Figure 6.1 shows the predicted diffuser CP values as the diffuser area ratio and aspect ratio is varied. At AR = 1.0 the diffuser pressure recovery increases as aspect ratio is reduced (i.e. reducing S/H from 1.2 to 0.4). The diffuser performs better despite increased stagnation pressure loss (Y_s) at S/H = 0.4 due to the net reduction in the flow blockage (ζ). This trend continues for higher area ratios (of 1.5 and 2.0) suggesting that, at a given area ratio, a tight diffuser configuration can be an effective method of increasing the static pressure recovery. Figure 6.2 plots the diffuser blockage and pressure recovery along mean diffuser length values at an area ratio of 1.5 and different S/H values tested. With reduction in the diffuser S/H to 0.4, blockage values are higher for the initial diffuser length due to the presence of high momentum flow enhanced by the presence of a supersonic flow expansion around the diffuser casing. Once flow has passed the region of high curvature (20% diffuser length), the flow undergoes a high diffusion phase due to the presence of both high momentum and rapid change in the area. Thus, blockage values above 20% diffuser length starts to fall down steeply which contributes equivalently to the pressure recovery values shown in the same plot. Diffusers with S/H = 0.8 and 1.2, undergo same but less prominent phenomena thereby producing lower pressure recovery at the diffuser exit. It is however, essential to note that such effects can swap at low system pressure ratios where flow becomes less supersonic.

Figure 6.3 shows the pitchwise average Mach number for each diffuser geometry. A patch of supersonic flow develops over the initial part of the lip, and this is terminated by a normal shock wave (labelled 'X' for S/H = 0.4). As the diffuser length is reduced, the curvature of the lip is increased and there is a subsequent increase in Mach number in the supersonic region of the diffuser, and thus an increase in strength of the normal shock. Thus, the rise in CP as the diffuser S/H ratio is reduced, is largely due to the increased streamline curvature which raises the diffuser lip loading. The presence of higher loss (Y_s) at S/H = 0.4 can therefore be attributed to the increased shock loss present in these cases.

Figure 6.4 plots rotor total-to-total and system total-to-static efficiencies for the rotor-diffuser system tested. At AR = 1.0, the differences in rotor total-to-total efficiency between cases with different S/H values are very small (roughly 0.1% change on average). The pattern continues at higher diffuser area ratios; cases with S/H = 1.2 are predicted to have rotor efficiencies which are slightly higher than cases with S/H=0.4 and 0.8. Since the effects of diffuser aspect ratio on rotor efficiency are small, the changes in system efficiency

are therefore predominantly affected by the changes in diffuser CP. The system total-to-static efficiency values follow a similar trend with S/H as observed in the diffuser pressure recovery (CP) seen in Figure 6.1 at any given area ratio.

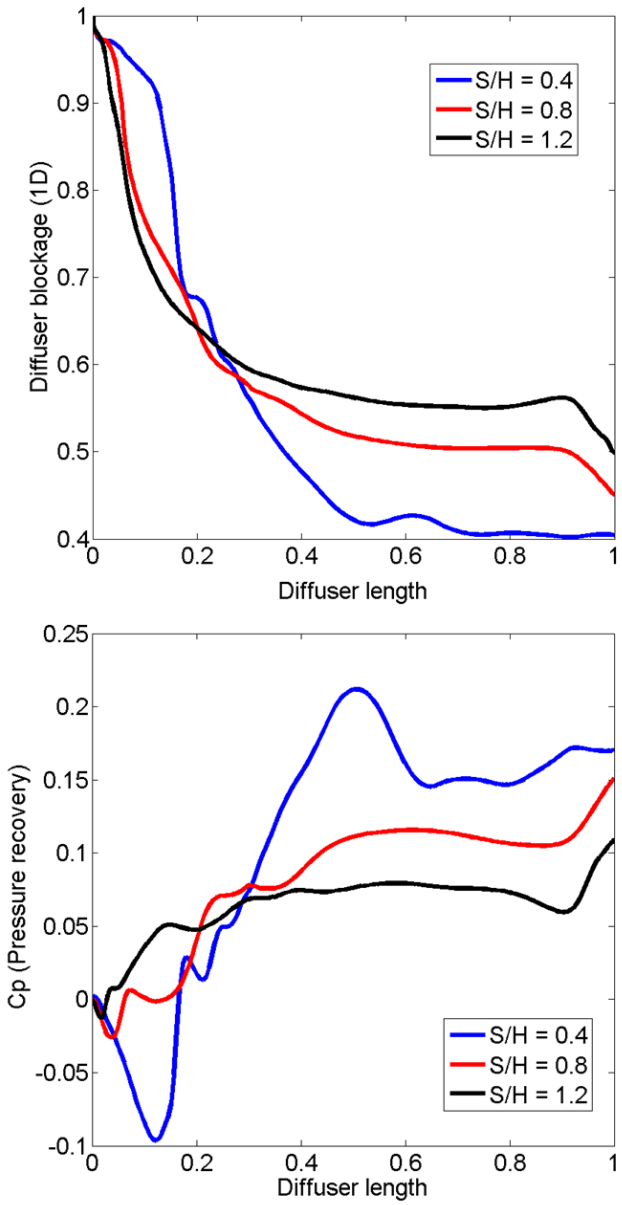

FIGURE 6.2. DIFFUSER ζ AND CP ALONG MEAN DIFFUSER LENGTH AT AREA RATO = 1.5 AND THREE S/H VALUES

Going back to the Figure 6.1 again and scrutinize the changes in pressure recovery values (CP) at S/H = 0.8. A large (roughly 8%) change in the CP can be observed as area ratio is increased from AR = 1.0 to AR = 1.5. Increasing AR to 2, leads to a further improvement in CP however the changes become marginal (about 0.25%). Looking at the

corresponding values of stagnation pressure loss (Y_s), these remain nearly constant and thus the rise in CP is largely due to a drop in the blockage (ζ). The trends are similar at S/H = 0.4 and S/H = 1.2 with slightly increased (roughly 1.6% on average) stagnation pressure losses (Y_s) at S/H = 0.4. This pattern can be observed in the system total-to-static efficiency change for S/H = 0.8 in Figure 6.4 where the system undergoes approximately 2.28% increase in the efficiency from AR = 1.0 to AR = 1.5, while 0.015% change in efficiency as area ratio is increased further up to 2. Similarly, the system total-to-static efficiency follows the same trend for different S/H values.

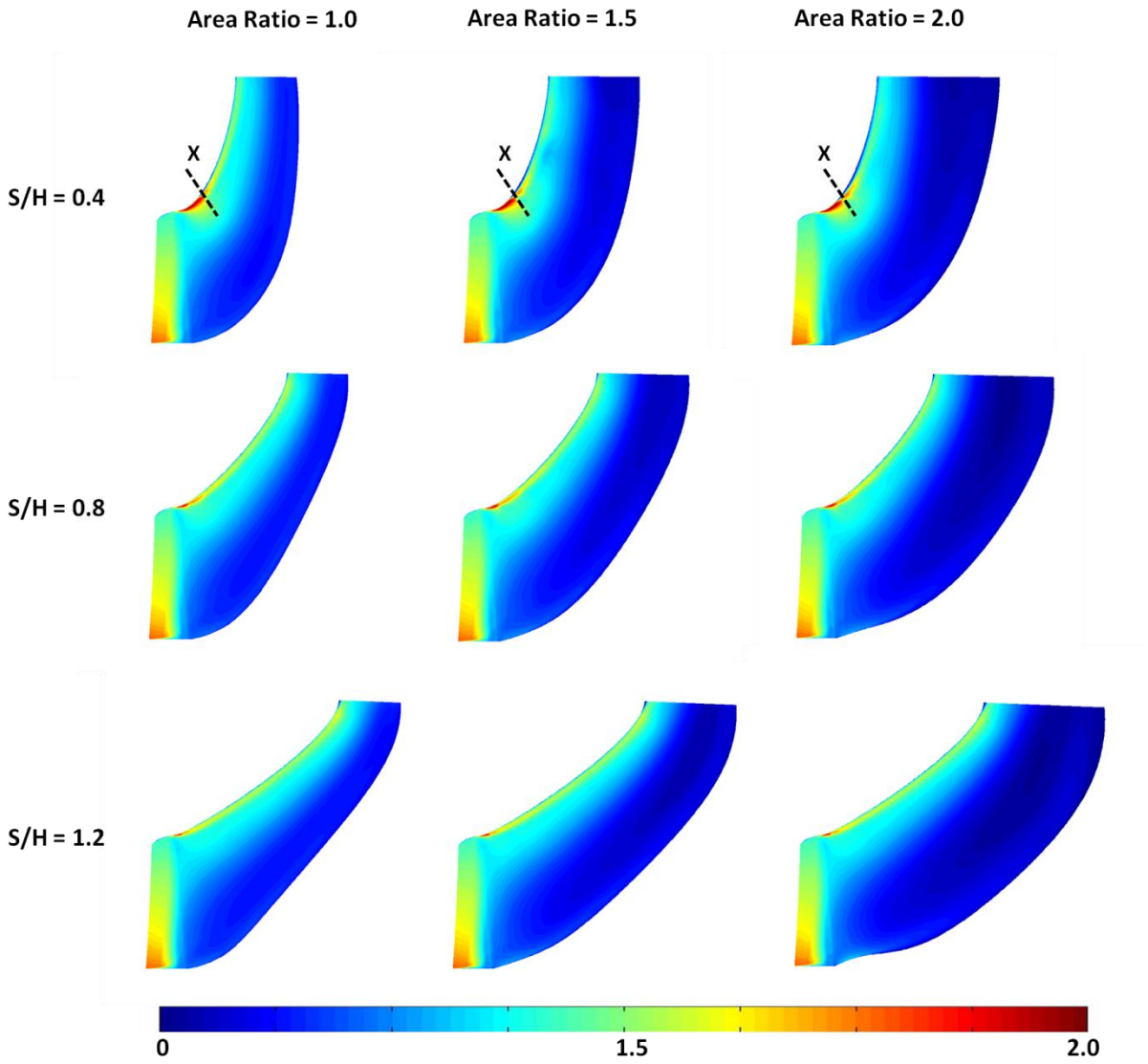

FIGURE 6.3. PITCHWISE AVERAGE ABSOLUTE MACH NUMBER WITH TIP GAP OF 1% SPAN

Figure 6.5 plots the local diffuser pressure recovery (CP) on the diffuser casing for the nine test cases and is computed as:

$$CP = \frac{P_{local} - P_{in}}{P_{o,in} - P_{in}}$$

Superimposed on this plot are contour lines of isentropic Mach number of 1 that determines the regions of subsonic and supersonic flow over the diffuser lip. Similarly, the trajectories of trailing edge shock propagation and leakage flow traces are superimposed. Here, the leakage flow trace line is obtained by tracking the region of high stagnation pressure in the near wall freestream flow. As seen earlier in Figure 6.3, the high curvature change of the casing at S/H = 0.4 gives rise to strong casing side normal shock (note Isentropic Mach = 1 lines) due to an expansion of supersonic flow exiting the rotor. Following the leakage flow trace lines for each S/H value, it can observed that the leakage flow ejects out with smaller swirl at S/H = 0.4 and the presence of a supersonic flow expansion increases its strength further, thereby reducing casing surface static pressure. Thus the rotor tip leakage flow remains the dominating feature at low S/H (= 0.4) values due to the changes in streamline curvature of casing side flow. As the diffuser aspect ratio is increased, the influence of the leakage flow on the lip surface static pressure reduces and reveals the trailing edge shock present in the flow near to casing.

In general, a region of high casing side curvature at the diffuser inlet will produce an increasing pressure gradient away from the casing. This local pressure gradient modifies and reduces the spanwise pressure gradient due to the rotor-exit swirl. Thus, a local reduction in the static pressure will occur at the casing as S/H ratio is reduced that in-turn generates strong rotor trailing edge shocks. However, as mentioned earlier in Chapter 4 that the leakage flow has a large influence on the lip surface static pressure, and this further modifies the lip-surface static pressure. Section 6.3 will expand this study on the effect of different tip clearances on diffuser flow.

The diffuser tested up to now were designed using linearly increasing area ratio (AR). By varying the local area ratio along the flow path length the effect of local area ratio on diffuser performance can be made. This is achieved by varying the diffuser hub curvature along the diffuser length while keeping its casing fixed. Figure 6.6 plots such a diffuser with S/H = 0.4 and global area ratio (AR) = 1.5. The performance factors for these diffusers are plotted in Figure 6.7. It can be noted down that the diffuser pressure recovery (CP) increases by 1.83% from 'Frontal loaded' to 'Linearly loaded' diffuser and 0.53% from 'Linearly

loaded' to 'Aft loaded' diffuser. Figure 6.8 shows that the predicted Mach number within these diffusers is not greatly affected by these changes in hub shape. Thus, performance changes in these diffusers must be arising from the small differences in the streamline curvature of the flow which modify overall changes in the diffuser loss (Y_s) and blockage (ζ). The results indicate that small improvements in pressure recovery may be achieved by shaping the hub to achieve a more 'Aft loaded' diffuser.

From current understanding of the diffusers, it can be stated that the diffuser flow field around the casing can experience large supersonic flow expansions which should make this flow highly sensitive to the changes in the casing curvature. Such sensitivity can be examined by changes in the casing side curvature of the diffuser casing along its flow path length. Figure 6.9 plots three diffusers with identical S/H (=0.4) and global area ratio (AR) of 1.5 where the local area ratio is increasing linearly along the flow path length. Here, diffuser 'A', 'B' and 'C' are designed to have a curvature distribution which is increasingly less aggressive (lower curvature) near its inlet , such that case 'A' has the highest inlet curvature, while case 'C' has the lowest inlet curvature. It should be noted that under the constraint of a fixed area distribution, modification in the casing side curvature will equally modify the hub curvature as shown in the figure. It should also be noted that there is a small difference in the flow path length for these diffusers.

Figure 6.10 plots the one-dimensional performance factors for the diffusers shown in Figure 6.9. Overall, the effect of casing curvature does not appear to greatly affect the pressure recovery; changes in loss tend to be offset by the effect of curvature on blockage. These changes become more apparent when the diffuser flow is visualized in its pitchwise average Mach number plot shown in Figure 6.11. For aggressive diffuser 'A', it can note a casing side normal shock (labelled as 'X') which subsequently induces a flow separation. The shock strength is reduced as the diffuser inlet curvature becomes less aggressive which thus produces less stagnation pressure loss (Y_s).

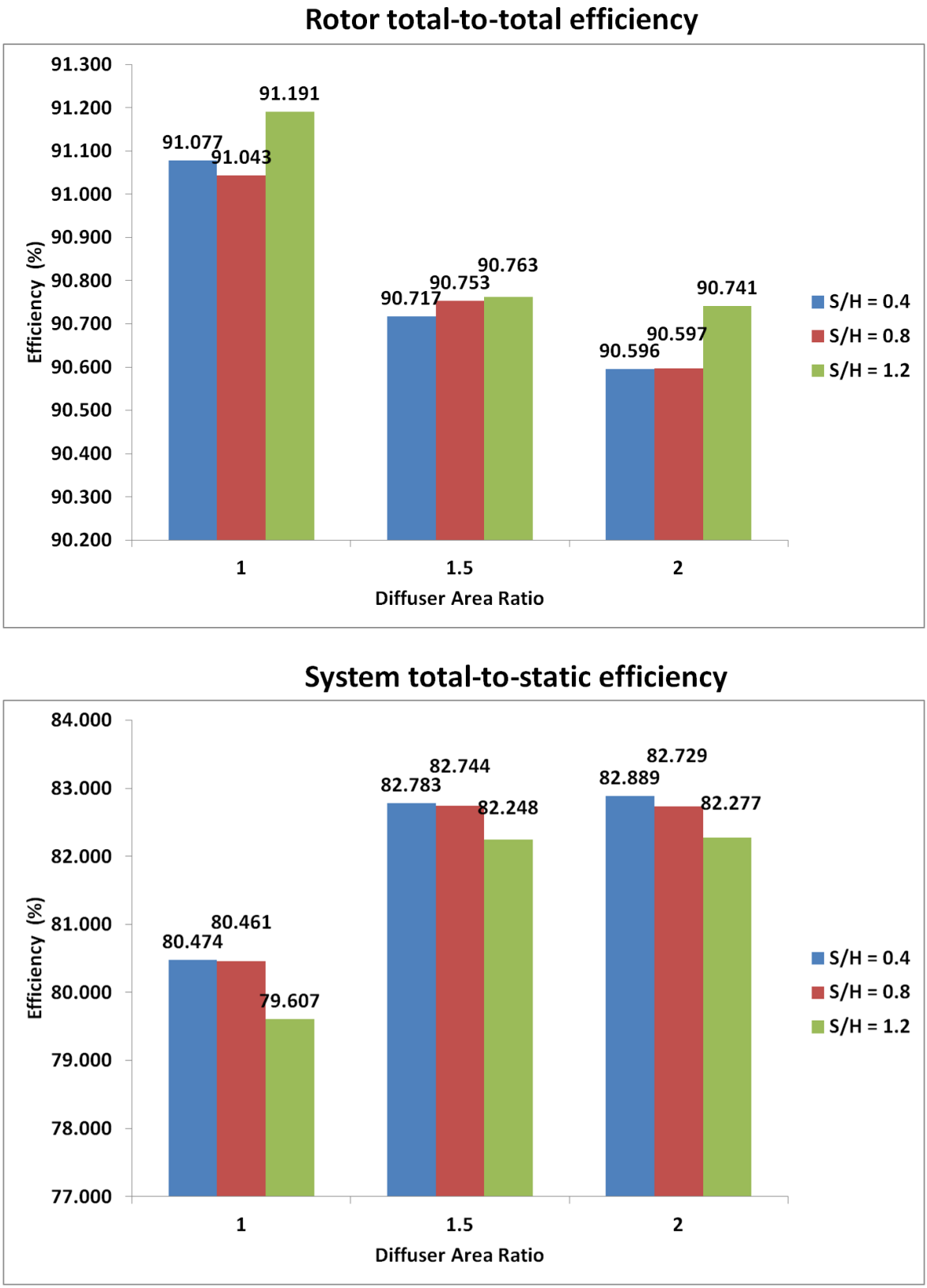

FIGURE 6.4. ROTOR AND SYSTEM EFFICIENCIES (TIP GAP = 1% SPAN)

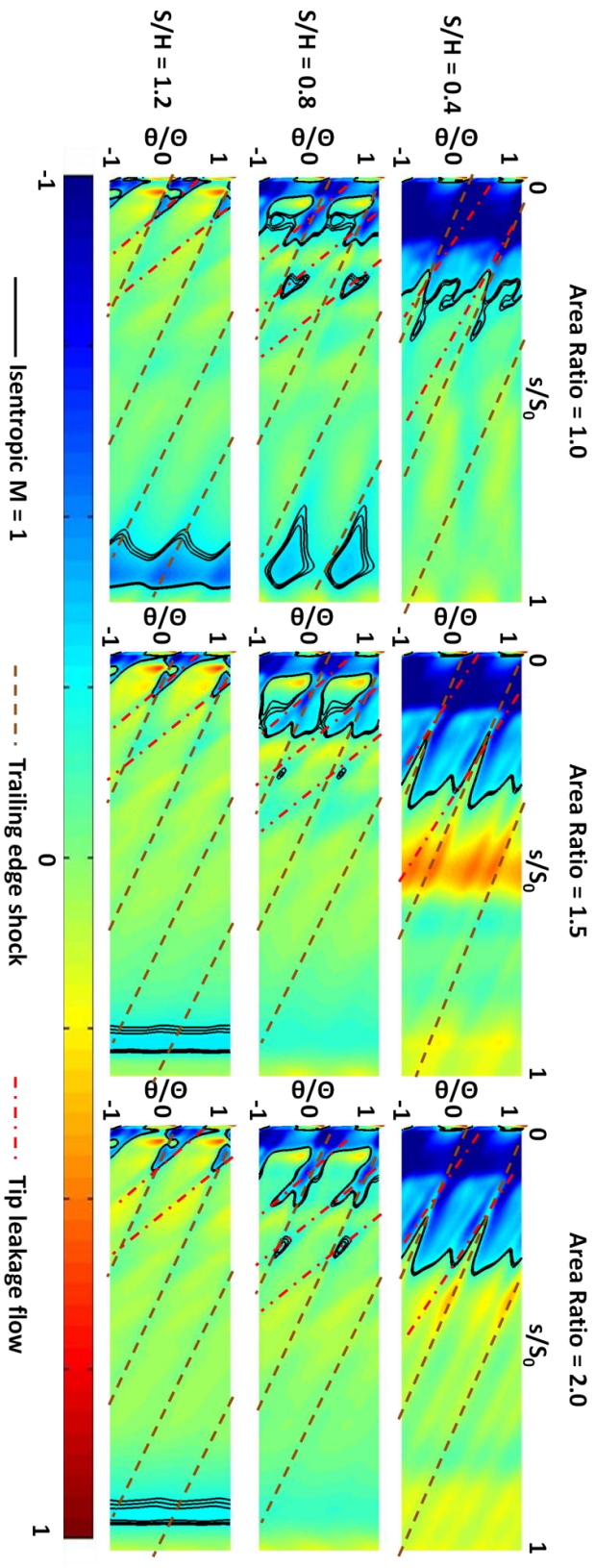

FIGURE 6.5. LOCAL CP VALUES COMPUTED ON DIFFUSER CASING (TIP GAP=1% SPAN)

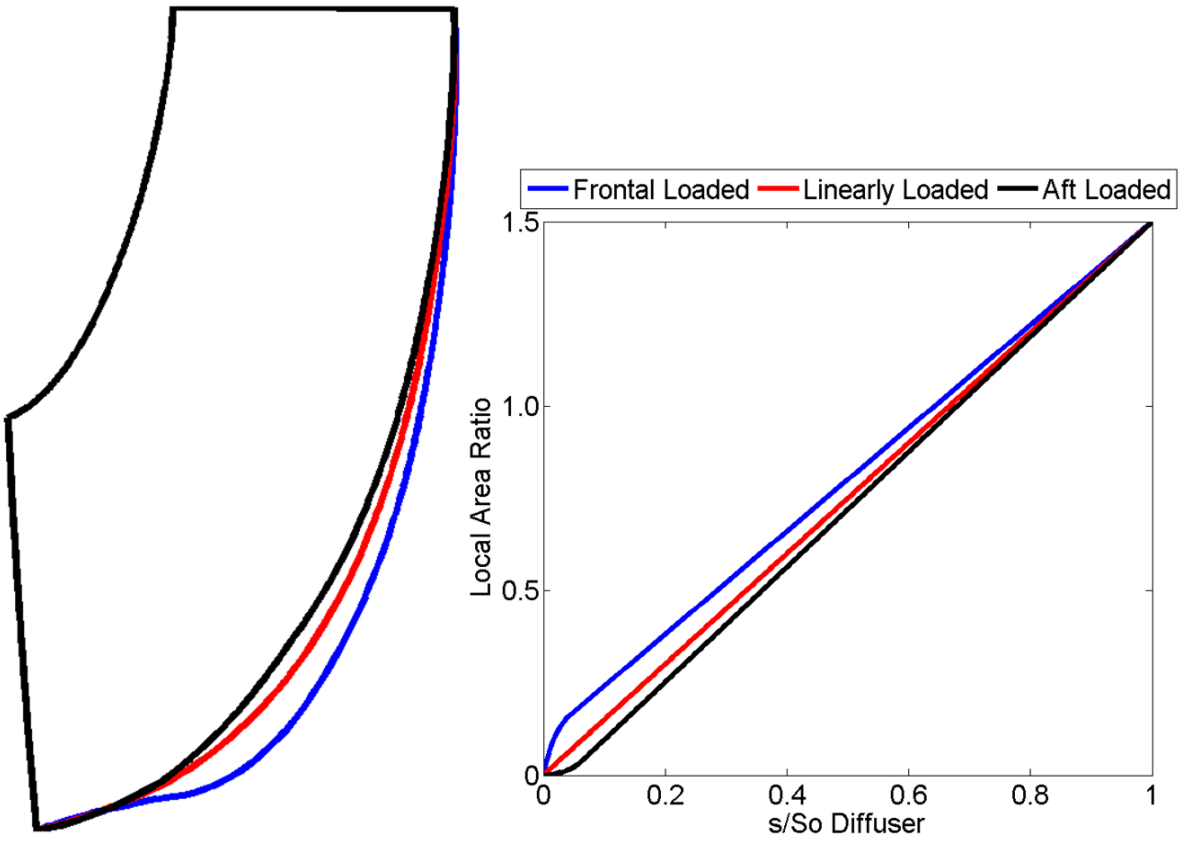

FIGURE 6.6. LOCAL AREA VARIATIONS ALONG DIFFUSER LENGTH

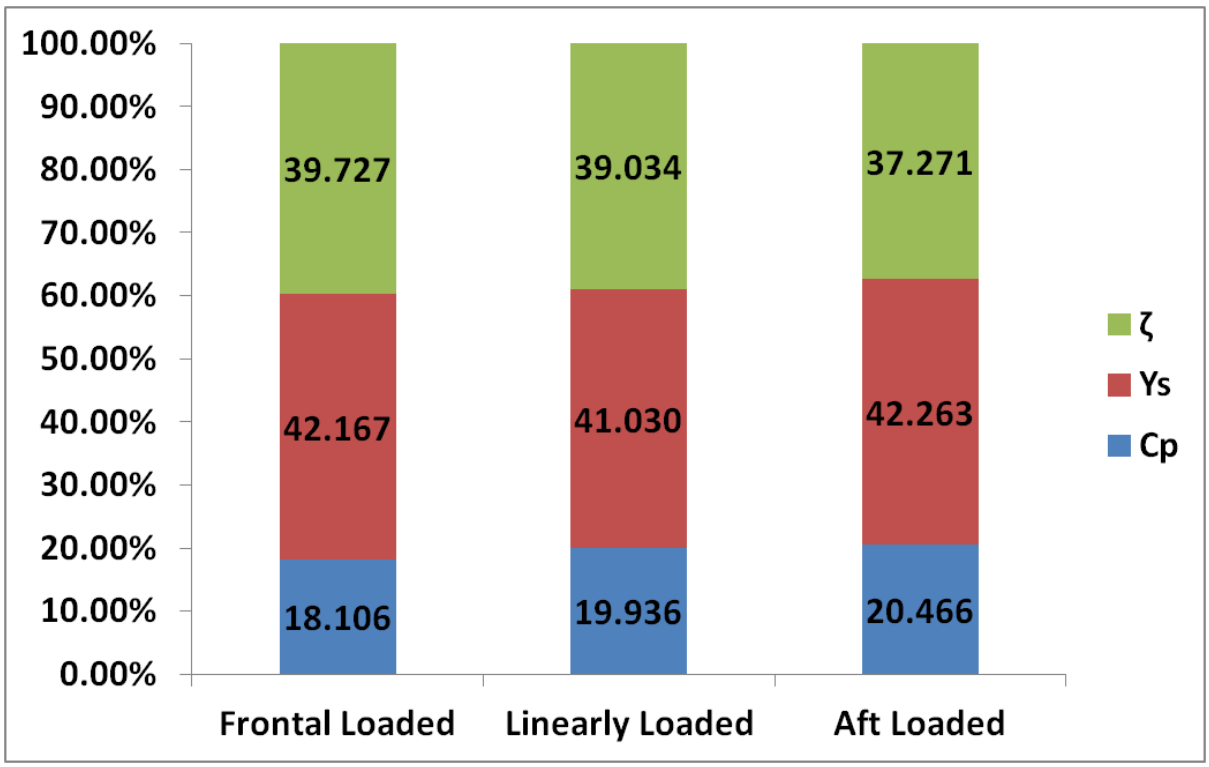

FIGURE 6.7. DIFFUSER PERFORMACE FACTORS

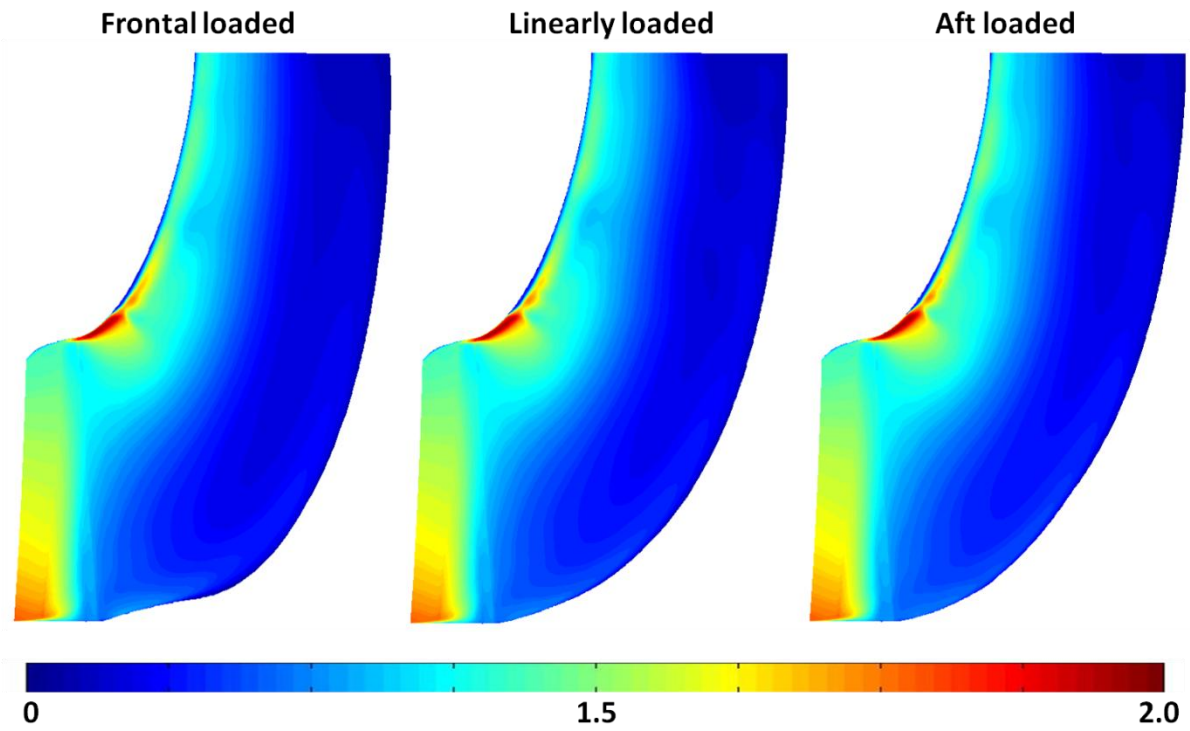

FIGURE 6.8. PITCHWISE AVERAGE MACH NUMBER

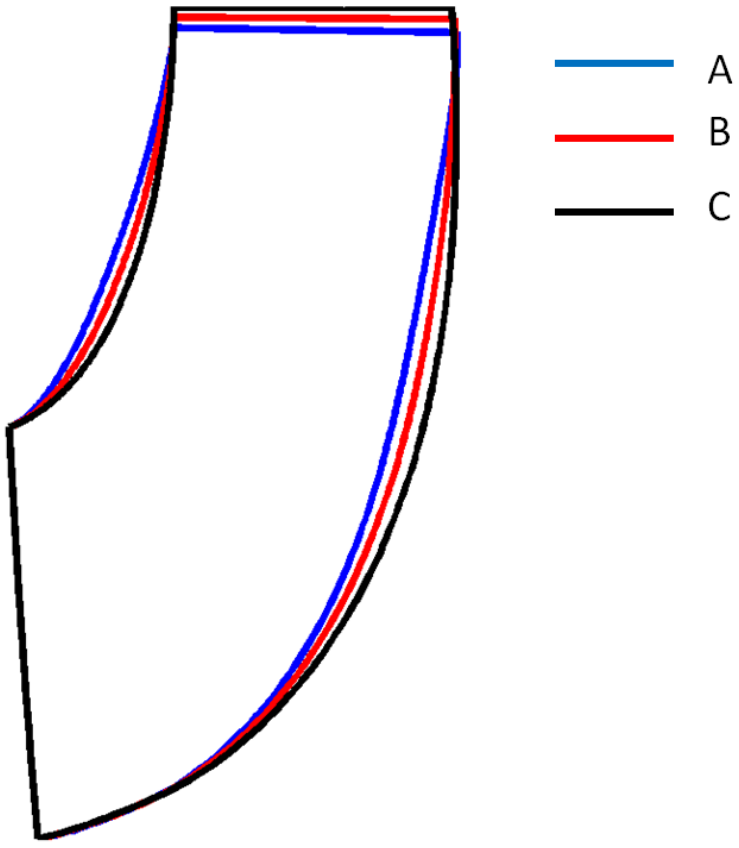

FIGURE 6.9. DIFFUSERS WITH VARIABLE CASING CURVATURE

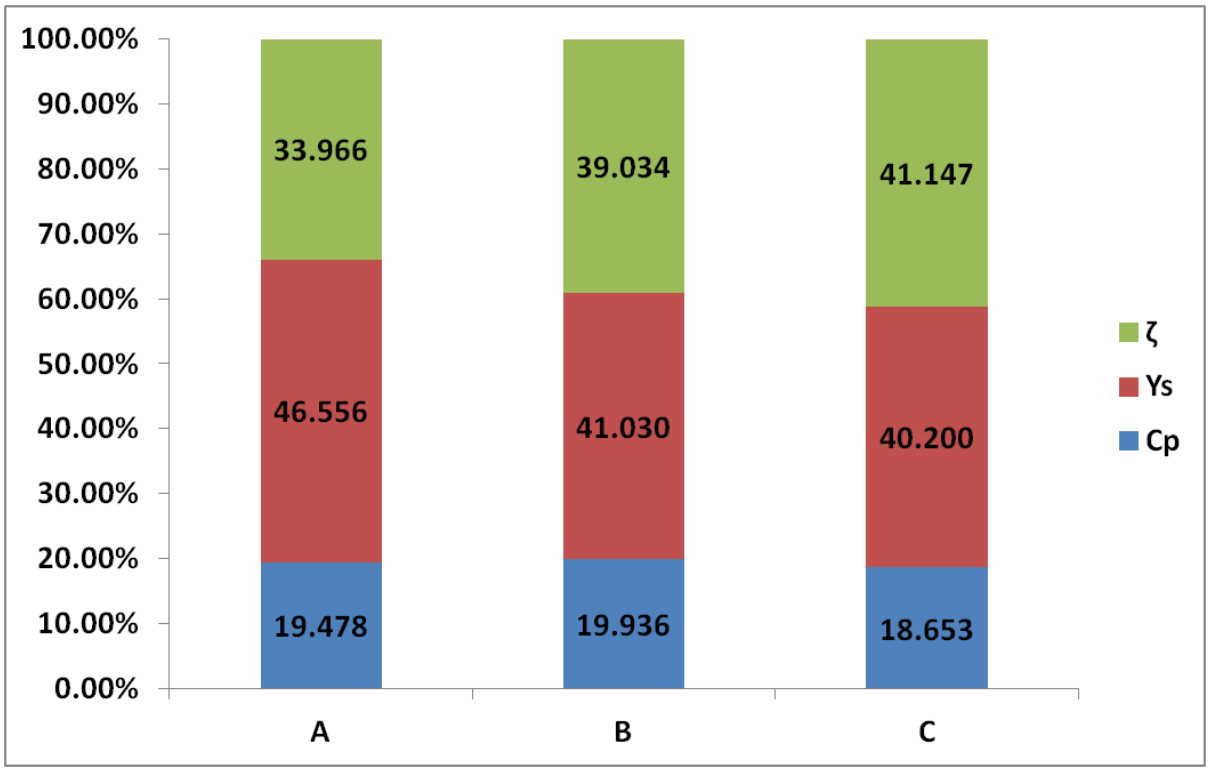

FIGURE 6.10. DIFFUSER PERFORMANCE FACTOR FOR DIFFUSERS WITH V ARIABLE CASING CURVATURE

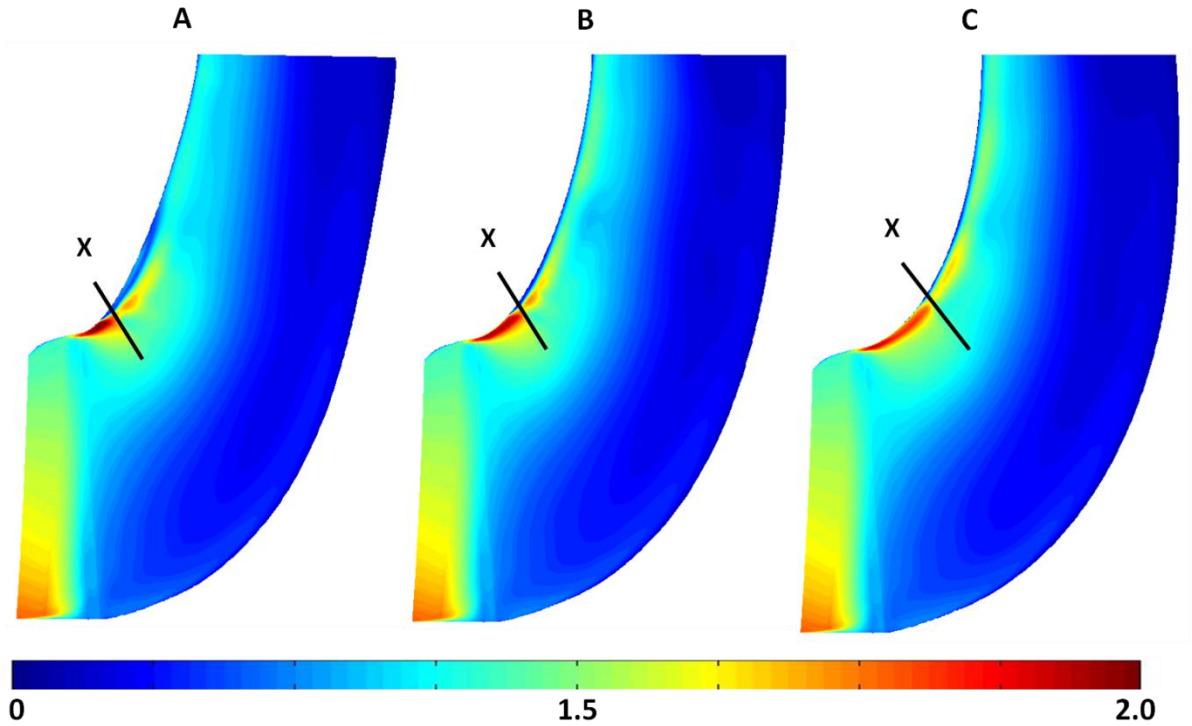

FIGURE 6.11. PITCHWISE AVERAGED MACH FOR DIFFUSERS WITH VARIABLE CASING CURVATURE

6.3 Effects of tip leakage flow and rotor hade angle

Similar to the previous section, the test cases were designed with diffuser casing aspect ratios of S/H=0.4, 0.8 and 1.2; where each of these casing side configurations are tested at three rotor casing hade angles, of 0^o, 25^o and 50^o (the hade is as defined in Chapter 5). As highlighted in Chapter 5, the rotor tip side sections are thin and reversed cambered. These configurations are tested at four rotor tip gaps of 0%, 0.5%, 1.0% and 1.5% of span, to understand the effect of leakage flow on rotor-diffuser flow interactions. Such configurations help in simulating the broad range of rotor casing side flow conditions and inlet flow to a diffuser. These diffusers are tested at an area ratio (AR) of 1.5.

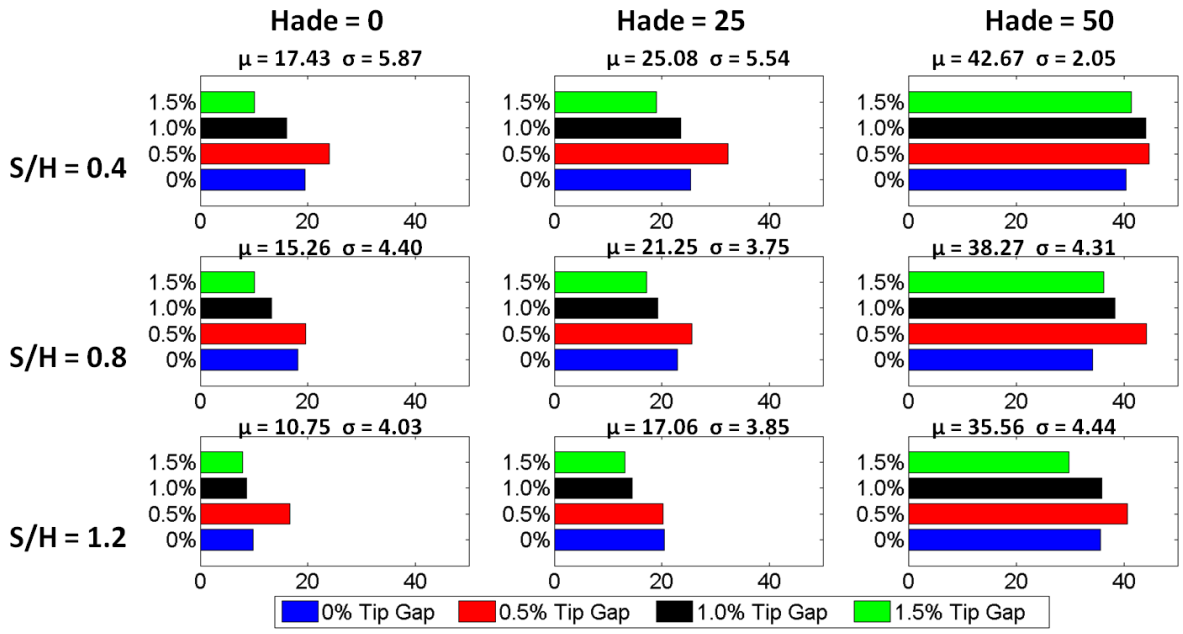

FIGURE 6.12. DIFFUSER PRESSURE RECOVERY (CP) VALUES

Figure 6.12 plots the diffuser static pressure recovery coefficient (CP) for various diffuser and rotor hade angle geometrical configurations. As mentioned in the findings of chapter 5, the diffuser pressure recovery increases with high hade angles due to the formation of a casing side supersonic flow compression corner near the rotor exit. Similar trends in improvement in CP can be seen for the corresponding higher hade angles for all S/H test cases at any tip gap value. Also, as discussed in the previous section, with increase in the S/H, a drop in the CP can be observed for all test cases. These results show that over a broad range of geometries, both hade angle (or the compression corner introduced by it) and low

S/H values (or the streamline curvature enhanced by it) are able to contribute significantly towards the diffuser static pressure recovery.

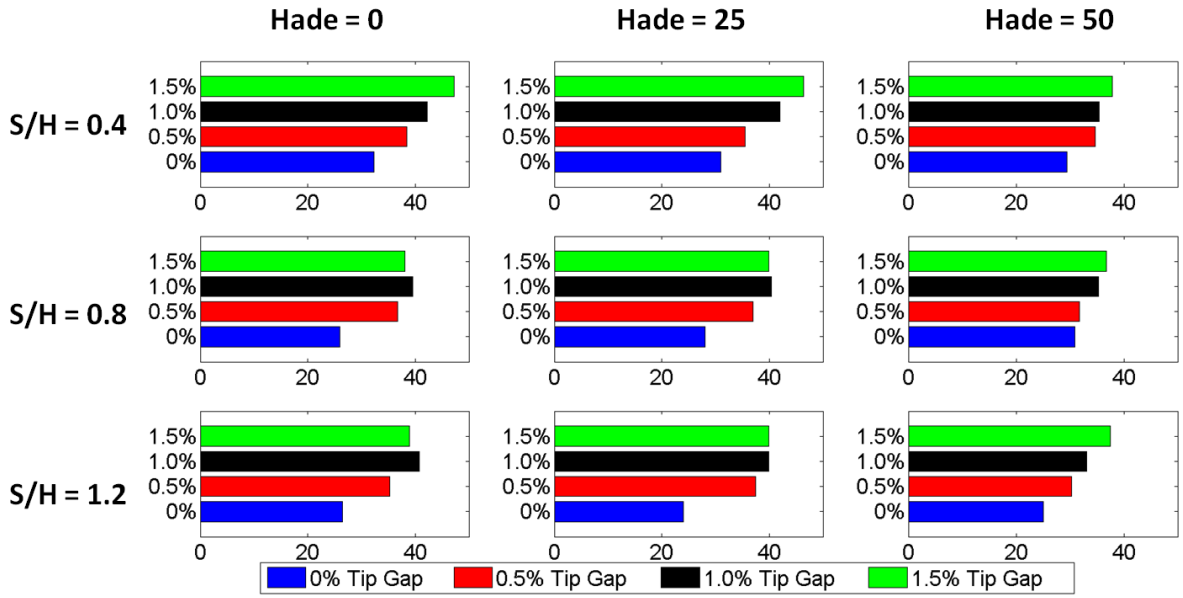

FIGURE 6.13. DIFFUSER STAGNATION PRESSURE LOSS (Y_S) VALUES

Figure 6.12 also shows that there tends to exist an optimum tip clearance at which the pressure recovery is maximized. For instance, for test cases with S/H = 0.4 and hade = 0^o, the changes in the CP with variation in rotor tip gap gives an optimum value of tip gap at 0.5% span. In fact, this optimum value (0.5% of span) exists for each of the diffuser and rotor hade angle configurations. In contrast, the stagnation pressure loss (Ys) shown in Figure 6.13 shows that the diffuser loss tends to be raised when the rotor tip gap is increased. The diffuser blockage (ζ) is plotted in Figure 6.14; the results show that the optimum value of CP and the influence of leakage flow on the diffuser pressure recovery are largely due to the effect of the leakage flow on blockage, since the leakage flow tends to minimize blockage at a clearance of 0.5% span. This is discussed in more detail later.

Figure 6.15 and Figure 6.16 plot the rotor total-to-total and system total-to-static efficiencies for all test cases. At S/H = 0.8 and hade = 25^o, the rotor total-to-total efficiency drops by 1.78% between zero tip gap case and 0.5% tip gap case. Similarly, rotor efficiency drops by 0.15% and 0.72% between each subsequent test case with increase tip gap (to 1.0% and 1.5% of span). Correspondingly, the system total-to-static efficiency drops by 2.58%, 0.877% and 0.901% between each subsequent test case with increased tip gap. The drop in efficiency trends are similar for each of the diffuser S/H and rotor hade angle tested. The

results show that, although there is an optimum clearance at which the diffuser pressure recovery is maximized, the benefit to the overall system is offset by the increased rotor losses which are incurred when the rotor clearance is increased from 0 to 0.5% span. For clearances above 0.5% span, both the rotor efficiency and diffuser pressure recovery tend to decrease. Thus, the overall effect of tip leakage for the cases tested here is detrimental to system performance.

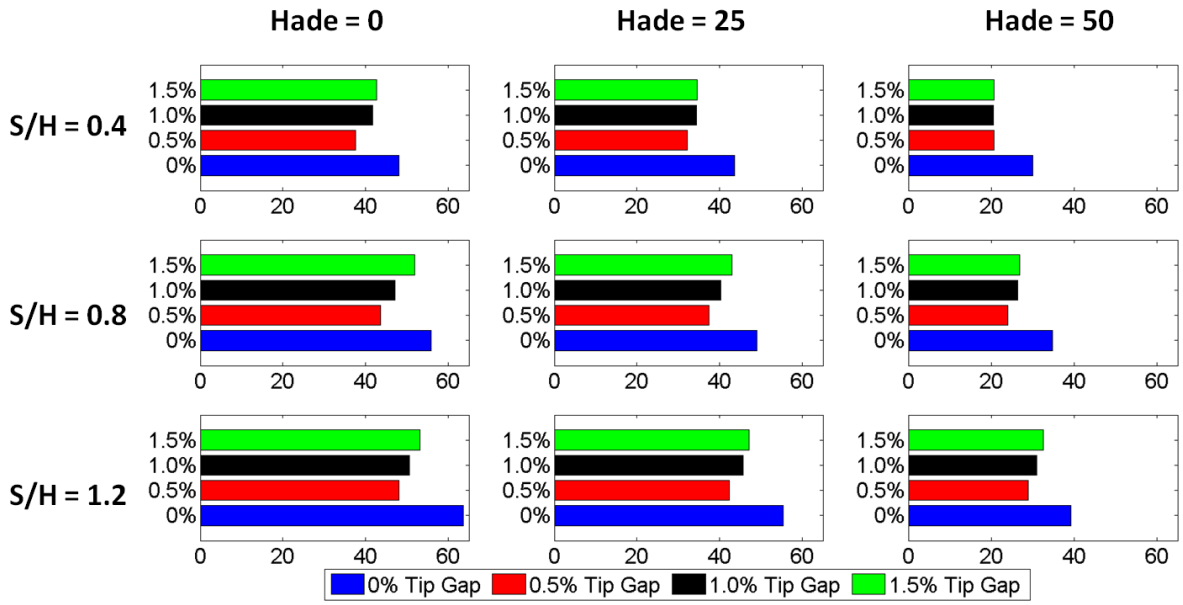

FIGURE 6.14. DIFFUSER FLOW BLOCKAGE (Z) VALUES

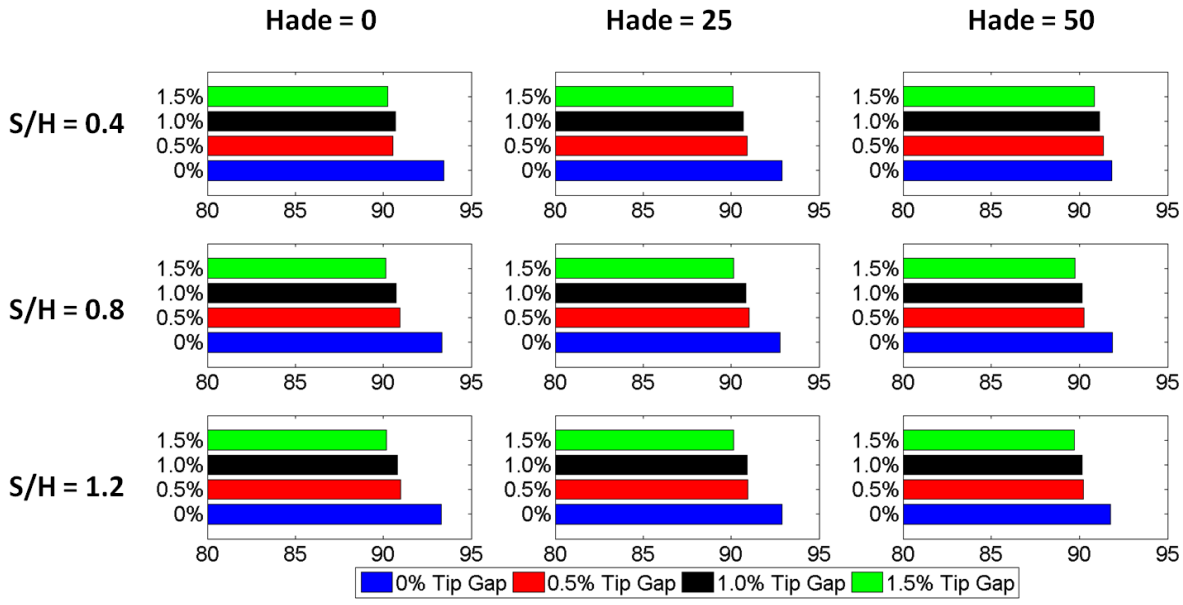

FIGURE 6.15. ROTOR TOTAL-TO-TOTAL EFFICIENCY

The existence of an optimum blockage value with a tip gap can be understood better by examining the flow within the diffuser. Thus, Figure 6.17 to Figure 6.19 show the pitchwise average absolute Mach number for test cases with tip gap 0%, 0.5% and 1.5%. At S/H = 0.4 and hade = 0^o, a large flow separation can be seen for the zero tip gap case, thus affecting the blockage in the diffuser (see Figure 6.17). When a small tip clearance of 0.5% span is introduced (see Figure 6.18) this separation is eliminated. However, increases tip gap tend to also raise the lip-surface static pressure (comparing Figure 6.17 to Figure 6.19) which will increase boundary layer losses (varying with V^3 (J. Denton, 1993)) and also leads to stronger casing side normal shocks. Thus, the amount of leakage flow along the diffuser casing drives the overall diffuser blockage (ζ) and in-turn affects its static pressure recovery (CP).

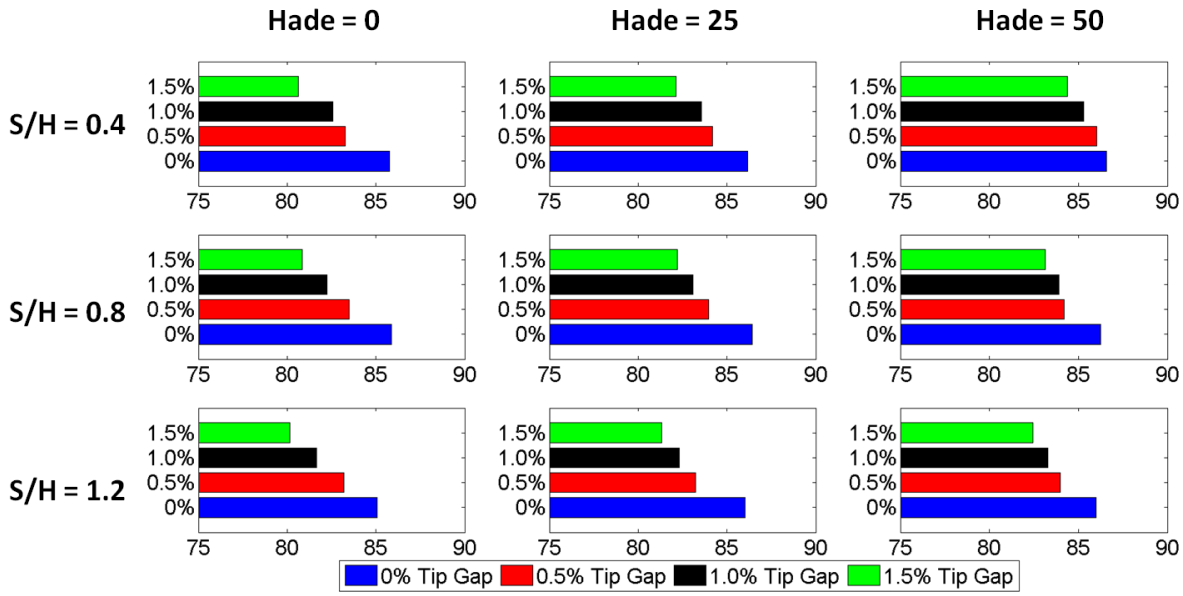

FIGURE 6.16. SYSTEM TOTAL-TO-STATIC EFFICIENCY

Again comparing the pitchwise absolute Mach numbers for S/H = 0.4 at different hade angles within Figure 6.17 reveals that the presence of a compression corner helps to redirect the flow towards the diffuser casing, thereby helping to keep the casing side flow attached for a longer surface length. The pattern continues for other S/H values in the Figure 6.17. Similar effects are seen when a leakage flow is introduced as shown in Figure 6.18 and Figure 6.19. As discussed in the chapter 5, the strength of the leakage flow is considerably reduced at high hade angles, as can be seen for all S/H test cases at different tip gap heights in Figure 6.20 (plotted with a same procedure as in Figure 6.5). It should however be noted that although hade angle helps to raise diffuser CP in a monotonic fashion with changes in

S/H and hade angles (see mean CP values inside Figure 6.12), its effects are non-linear across different tip gap cases (notice changes in the standard deviation of CP values in Figure 6.12). Thus, the presence of a hade angle improves the diffuser pressure differently for each tip gap case selected in this study.

6.4 Conclusions

The present chapter focused on the effects of diffuser area ratios on the coupled rotor/diffuser performance and along with the effect of diffuser casing side aspect ratio (S/H) on the coupled system performance. The results revealed that significant improvement in the diffuser pressure recovery can be made for the tight exhausts with an attached flow on its casing. However, after a certain geometrical area ratio (1.5) the performance improvements are marginal. A designer can improve diffuser design further by optimizing its geometrical area distribution or the curvature along its casing.

A diffuser performance mapping was made across a range of diffuser casing side aspect ratios (S/H), hade angles and tip leakage flow. The study revealed that the diffuser pressure recovery can be enhanced by employing an optimum value of the tip gap size, unfortunately the improvement in pressure recovery was offset by a reduction in rotor efficiency and the overall system performance was always detrimentally impacted by tip gap in the cases tested here. The changes in the hade angle helped in both suppressing the leakage flow and keeping diffuser casing attached at the same time. The usage of a hade angle (or a compression corner introduced by it) is found to be much more effective in improving the diffuser performance than usage of high diffusion area ratio, diffuser aspect ratio (S/H), lip curvature or an optimum tip gap flow.

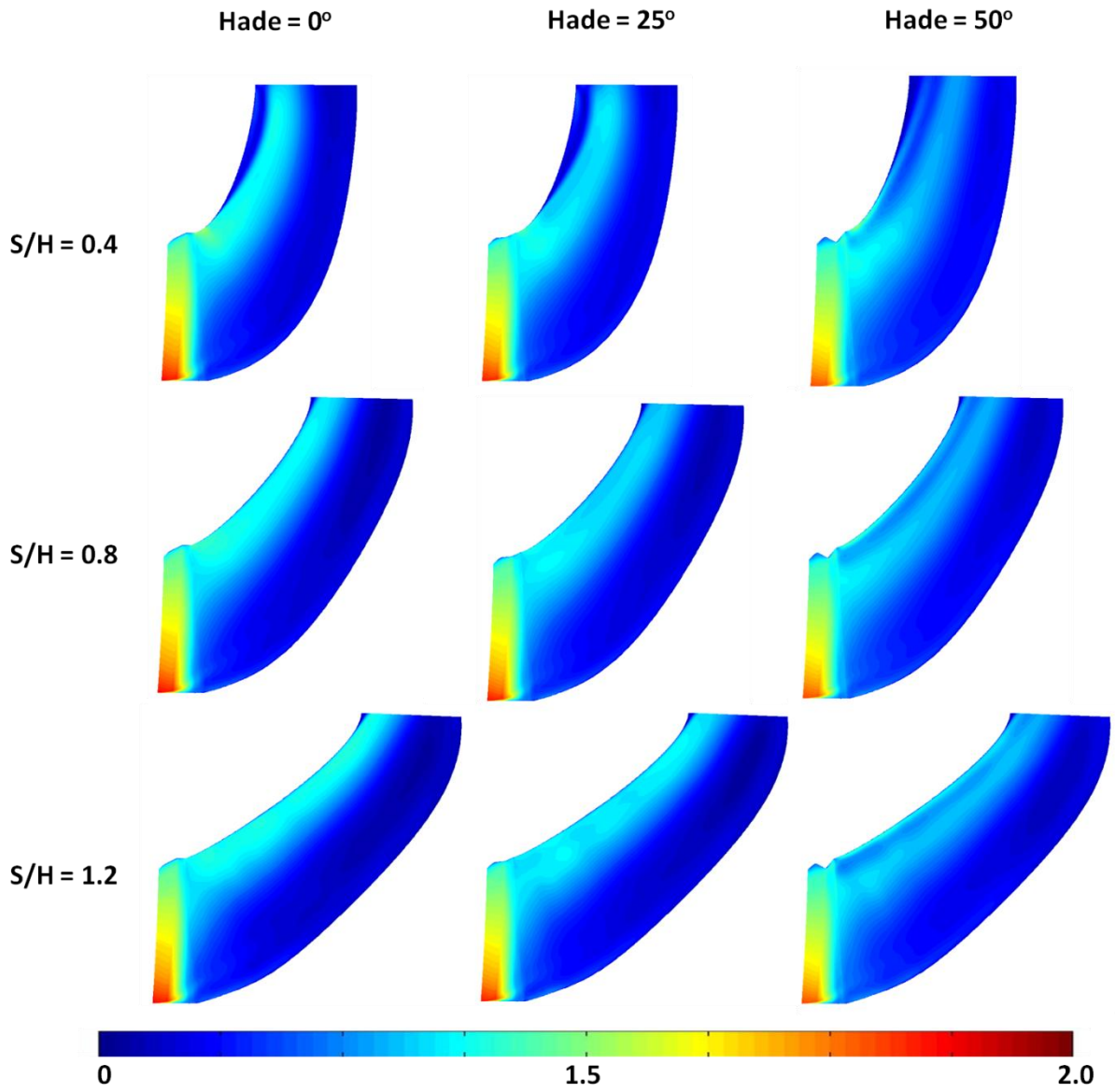

FIGURE 6.17. PITCHWISE AVERAGED ABSOLUTE MACH NUMBER AT TIP GAP OF 0% SPAN

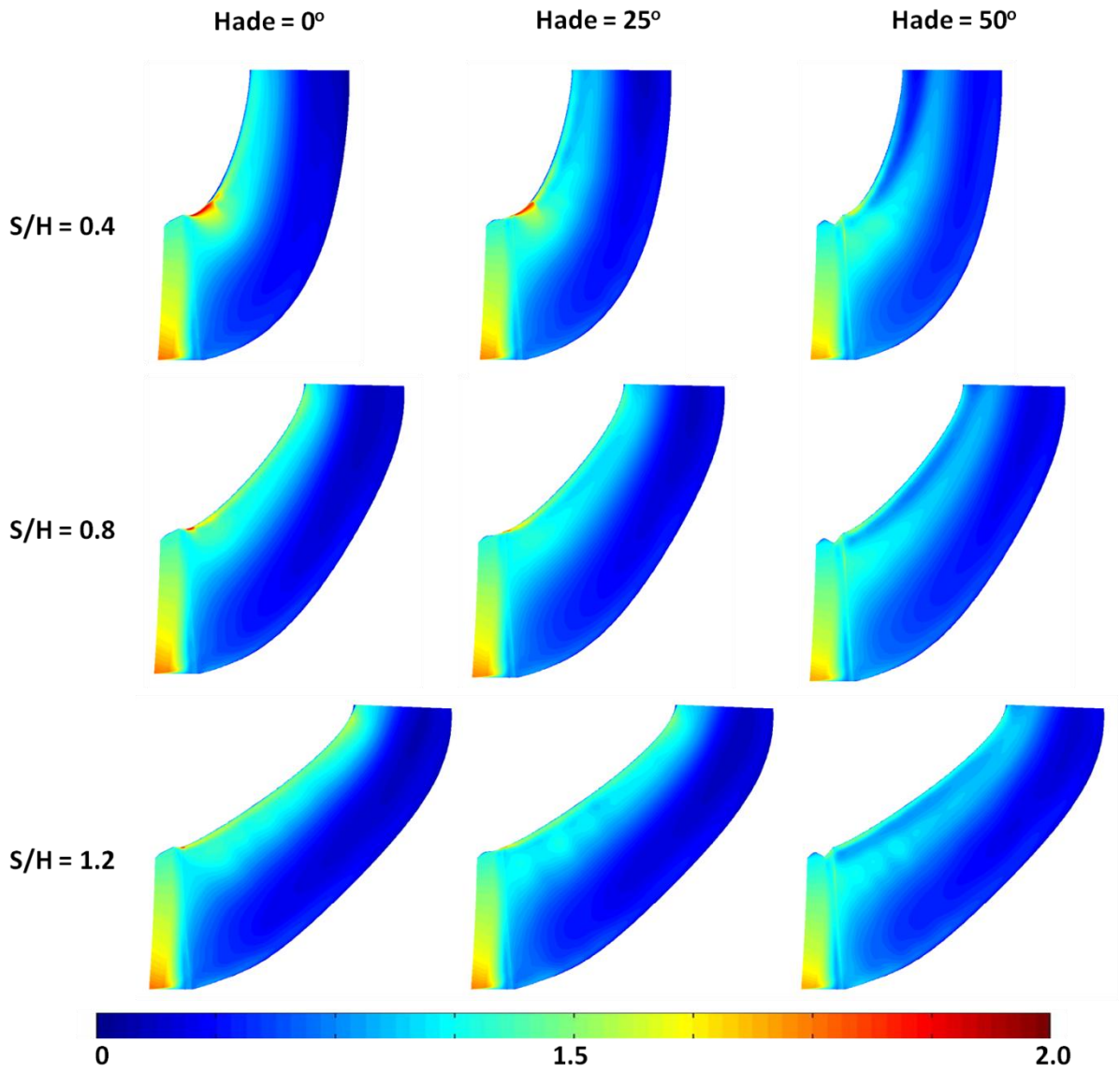

FIGURE 6.18. PITCHWISE AVERAGED ABSOLUTE MACH NUMBER AT TIP GAP OF 0.5% SPAN

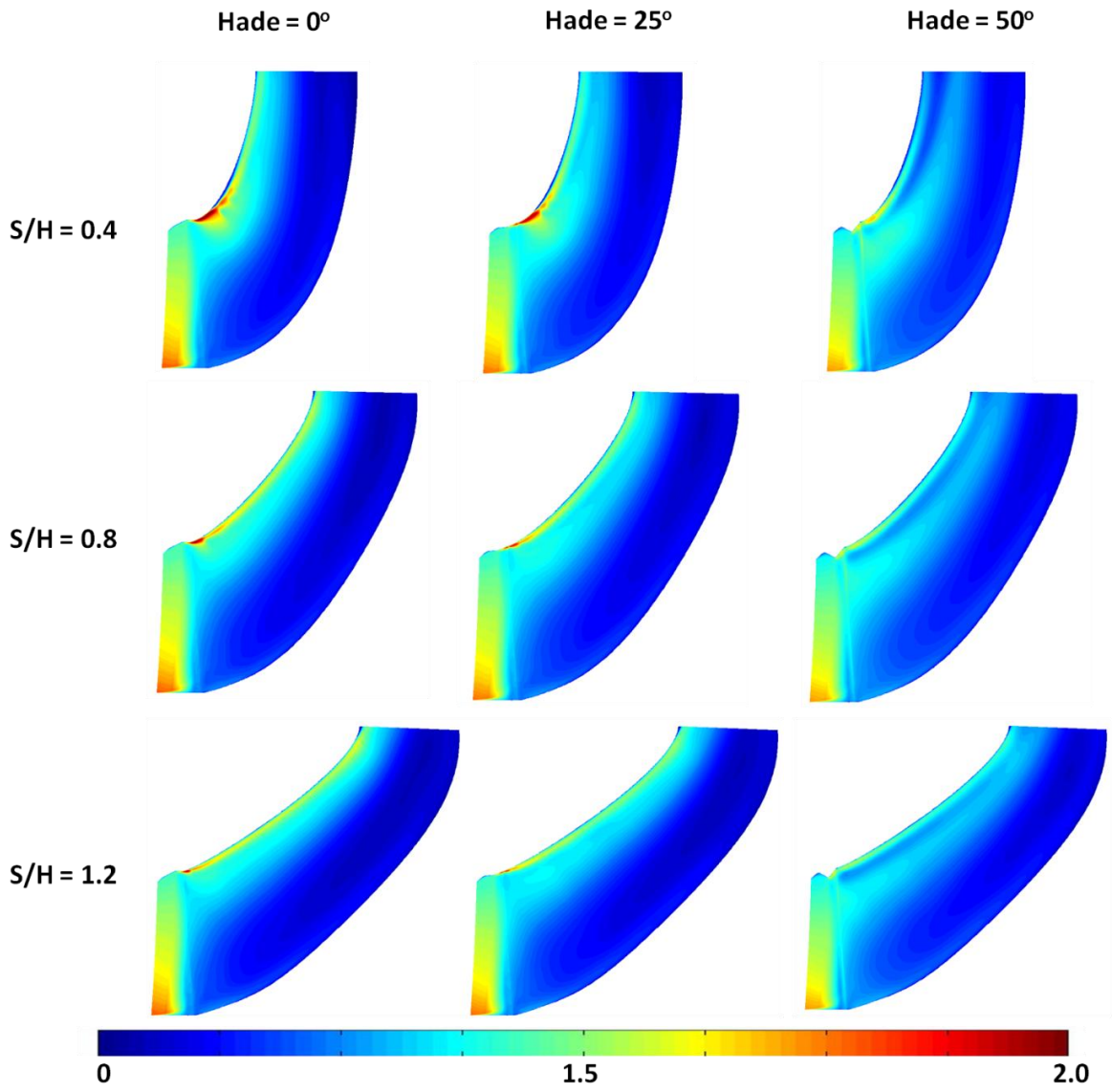

FIGURE 6.19. PITCHWISE AVERAGED ABSOLUTE MACH NUMBER AT TIP GAP OF 1.0% SPAN

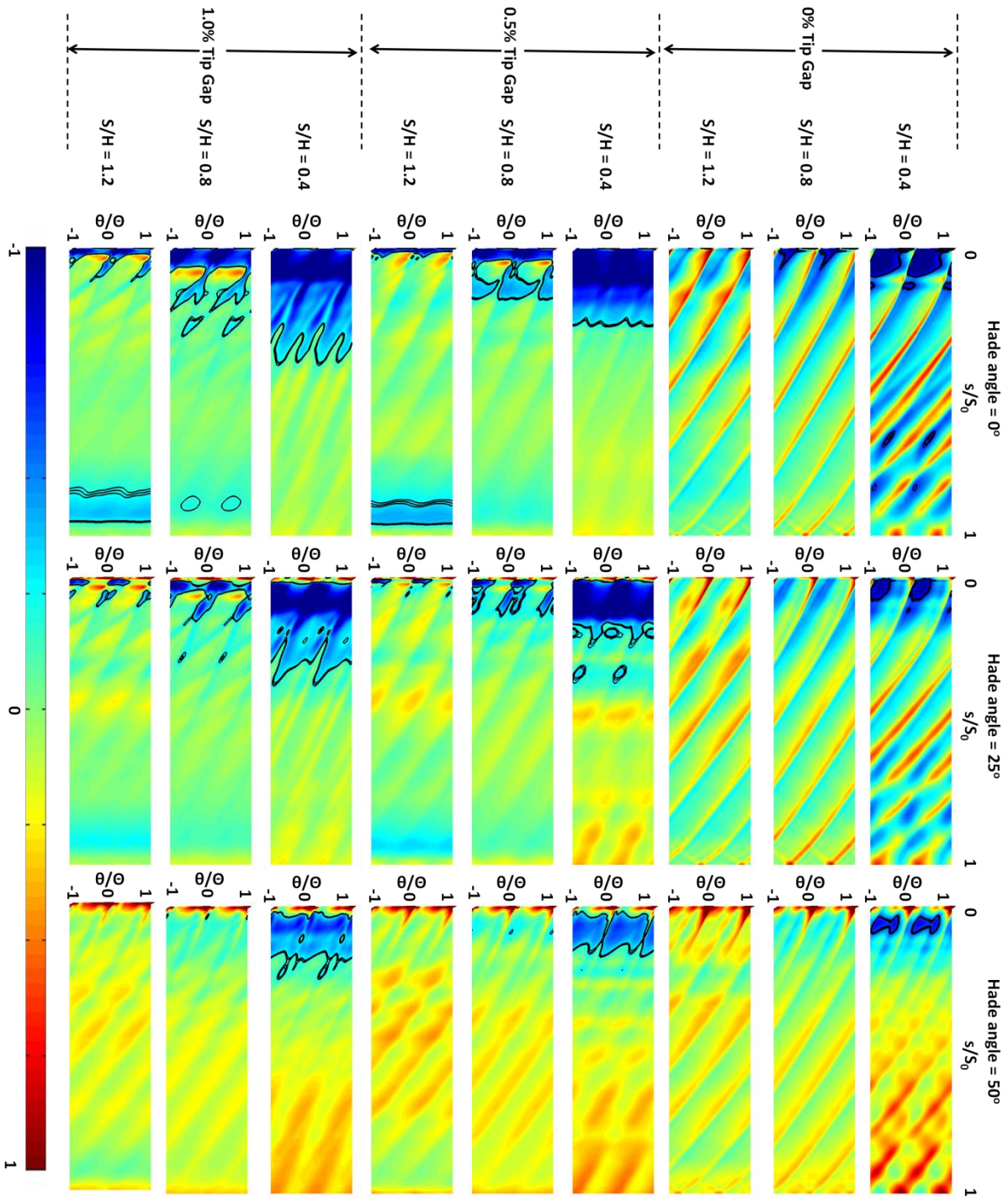

FIGURE 6.20. LOCAL CP VALUES COMPUTED ON DIFFUSER CASING

7: Conclusions and suggestions for future work

Chapter Outline:

This chapter summarizes the findings of this thesis along with the suggestions for continuing research on low pressure steam turbine and diffuser interactions.

7.1 Conclusions

Steady-state fluid flow interactions between the last stage of a low pressure steam turbine and its axial-to-radial diffuser are found to be highly three-dimensional and complex. The present study kept its focus primarily on the casing side flow features, namely: circumferential non-uniformities, rotor trailing edge shocks, tip leakage flow, blade wakes and diffuser casing side normal shocks. These flow features interact with each other and thus affect global performance factors that result in fluidynamic coupling between the rotor and diffuser.

The investigation of the study was started by systematically isolating the key flow features and understanding the relative changes in the defined performance factors and general dynamics. First, the presence of circumferential flow non-uniformities in the rotor exit flow resulted in slightly reduced rotor efficiency which was found to be driven by a small drop in the diffuser pressure recovery. Secondly, the presence of a tip leakage flow was found to lead to a drop in both rotor and diffuser performance factors. Changes in the rotor exit operating flow conditions also shifted the location of the trailing edge shock arm and casing side normal shocks which affected the estimation of averaged one-dimensional performance parameters. Under favourable conditions, a casing side normal shock can be used to efficiently raise the diffuser static pressure without much loss in the performance output. Finally, the rotor trailing edge shocks themselves proved to have a detrimental effect by increasing the entropy generation in both the rotor blade passages as well as the diffuser, since they propagated throughout the diffuser. For cases without a leakage flow, trailing-edge shocks were found to greatly influence the unsteady pressure field on the diffuser casing. However, the presence of a leakage flow virtually eliminated this effect, because the leakage flow off-loaded the rotor tip and reduced the trailing-edge shock strength.

Significant levels of stagnation temperature change occurred within the rotor tip gap flow by a process known as a ‘pumping effect’. This mechanism reduced the work extraction capability of the rotor and showed the strong presence in the mixing losses within a downstream diffuser. While designing the rotor casing profile in a such a manner that it yields a compression corner near the rotor trailing (via a 'haded rotor') was found to give rise to an improvement in diffuser pressure recovery. The rotor total-to-total efficiency was found to be insensitive in the presence of such casing side configuration.

Finally, the diffuser performance mapping revealed that there is a limit for every diffuser configuration after which increases in given geometrical area ratio do not provide significant increases in the system total-to-static efficiency. At the same time, tighter exhaust diffusers gave a considerable improvement in the performance via a reduction in the flow blockage. The mapping also revealed the existence of the optimum value of the tip leakage flow at which diffuser blockage can be minimized. However, tip leakage flows were always found to be detrimental to the rotor performance, which mitigated the effects of improved diffuser performance and there was a net reduction in system efficiency with the introduction of a leakage flow. The presence of a haded rotor was found to be much more effective in raising diffuser pressure recovery for all tested diffuser configurations, as compared to the introduction of a leakage flow.

7.2 Suggestions for future work

The focus of the present study was maintained at casing side flow interactions for an unshrouded rotor tip gap. Thus, the results presented cannot be directly correlated to shrouded rotor geometries. The study of shroud leakage flows and their interaction with a downstream diffuser would seem an interesting avenue for future research.

In this study, the existence of highly supersonic flows near the casing region gave rise to strong trailing edge shocks. Since the present design trends are moving towards making even longer blades to reduce the rotor leaving loss as much as possible, future designs are likely to suffer from strong trailing-edge shock waves. Design consideration for the bow shock present upstream of the rotor leading edge is not uncommon. One arm of this bow shock wave impinges on the pressure side of the adjacent blade affecting the design considerations of the supersonic reversed cambered aerofoils. Thus, the presence of multiple

shocks while considering stator-rotor interactions will produce an unsteady pressure flow field near the casing region. Such flow field are bound to increase the complexity of the rotor-diffuser flow interactions and would therefore be an important area for future work.

The present study used a simple configuration of hade angle, keeping a casing point near rotor trailing edge fixed. This angle produced a conical profile of the rotor casing (for all hade > 0) and cylindrical profile for (hade = 0). However, a designer may explore moving the location of the compression corner (introduced by hade angle) anywhere along the rotor blade chord. Such designs can have implications on the rotor tip gap pumping effect and may be utilized to increase interactions with blade passage shock waves. At the same time, a designer may opt for exploring the effects of the variable tip clearance alongside non-axisymmetric diffuser shape (S/H value) and surface length. However, these design changes also require deep understanding into the endwall boundary layer loss variation which can be gained by performing rigorous computations like Large Eddy Simulations (LES) along the casing line. Such modifications can provide an insight into producing an optimized rotor and diffuser casing shapes.

Again, the focus of the present study remained inside a diffuser where the majority of the static pressure recovery takes place. While gaining the understanding of flow interactions within the diffuser flow is important, it is well-known from the literature that diffuser flow structures are heavily dependent on the non-axisymmetric nature of the exhaust hood. Thus, recently developed methods such as stage-rotor coupling studies via Non Linear Harmonics can offer computationally cheap but insightful results, and such approaches would also form an important area for future research.

Bibliography

1. Adkins, G. G., and L. H. Smiths. “Spanwise Mixing in Axial Flow Turbomachines.” *81-GT-57.* ASME, 1981.

2. Babinsky, Holger, and John K. Harvey. *Shock Wave-Boundary-Layer Interactions.* Cambridge Aerospace Series, 2014.

3. Babu, M., D. Bhatia, RK. Shukla, A. M. Pradeep, and B. Roy. “Effect of Turbine Tip Leakage Flows on Exhaust Diffuser Performance.” *GT2011-45457.* Proceedings of ASME Turbo Expo, 2011.

4. Becker, S., E. Gretschel, and M. Casey. “Influence of a Tip Clearance Jet on a Swirling Flow in an Axial-radial Diffuser.” *Journal of Turbomachinery* (Proc. 6th European Conference on Turbomachinery - Fluid Dynamics and Thermodynamics), 2005: 134(2), 021017.

5. Bernier, B. C., M. Ricklick, and J. S. Kapat. “Impact of a Collector Box on the Pressure Recovery of an Exhaust Diffuser System.” *GT2011-46455.* Proceedings of ASME Turbo Expo, 2011.

6. Bhat, S. P., and R. K. Sullerey. “An Assessment of Turbulence Models for S-Duct Diffusers With Flow Control.” *GTINDIA2013-3566.* ASME 2013 Gas Turbine India Conference, 2013.

7. Bindon, J.P. “The Measurement and Formation of Tip Clearance Loss.” *88-GT-203.* ASME, 1988.

8. Blanco, E. de la Rosa, H. P. Hodson, and R. Vazquez. “Effect of the Leakage Flows and the Upstream Platform Geometry on the Endwall Flows of a Turbine Cascade.” *Journal of Turbomachinery*, 2009: Vol. 131.

9. Burton, Z, G. Ingram, and S Hogg. “A Literature Review of Low Pressure Steam Turbine Exhaust Hood and Diffuser Studies.” *Journal of Engineering for Gas Turbines and Power*, 2013a.

10. Burton, Z., S. Hogg, and G. L. Ingram. “The Influence of Inlet Asymmetry on Steam Turbine Exhaust Hood Flows.” *J. Eng. Gas Turbines Power*, 2013b: 136(4).

11. Burton, Z.; Ingram, G.; Hogg, S. “A Novel Method of Coupling the Steam Turbine Exhaust Hood and the Last Stage Blades Using the Non-Linear Harmonic Method.” *GT2013-94184.* ASME Turbo Expo 2013: Turbine Technical Conference and Exposition, 2013.

12. C. Ruhl. “BP Statistical Review of World Energy.” London, United Kingdon, 2013.

13. Chaluvadi, VSP, AI Kalfas, MR Banieghbal, HP Hodson, and JD Denton. “Blade row interaction in a high pressure turbine.” *AIAA Journal of Propulsion and Power*, 2001: 17. pp. 892-901.

14. Chandler, K.D., A.J. White, and J.B. Young. “Unsteady Wetness Effects in LP Steam Turbines.” *GT-45320.* Proceedings of ASME Turbo Expo, 2011.

15. Córdova, M., and B. Stoffel. “Comparison of Various Turbulence Models in Respect to Their Suitability for CFD Calculations of Diffuser Flows.” *GT2006-90524.* ASME Turbo Expo 2006: Power for Land, Sea, and Air, 2006.

16. Cumpsty, NA, and JH Horlock. “Averaging nonuniform flow for a purpose.” *Journal of Turbomachinery - Transactions of the ASME*, 2006: Vol: 128, Pages: 120-129.

17. Delery, J., and J.G. Marvin. *Shock-Wave Boundary Layer Interactions.* AGARD-AG-280, AGARD, 1986.

18. Denton, J. *Calculation of Fully Three Dimensional Flow Through Any Type of Turbomachine Blade Row.* LS 140., AGARD, 1985b.

19. Denton, J. D. “3D Flow Calculations on a Hypothetical Steam Turbine Last Stage.” In *Aerothermodynamics of Low Pressure Steam Turbines and Condensers*, by M.J. Moore and C.H. Sieverding. Washington DC.: Hemisphere, 1985a.

20. Denton, J. D. “The Calculation of Three-Dimensional Viscous Flow Through Multistage Turbomachines.” *Journal of Turbomachinery* (Transactions of ASME), Jan-1992: p18-26/Vol. 114.

21. Denton, J. D. “Time Marching Methods for Turbomachinery Flow Calculation.” In *Numerical Methods in Applied Fluid Dynamics*, by B. Hunt. New York: Academic Press, 1980.

22. Denton, J. “Personal communication.” *Consultant to Alstom Power, Rugby, UK.* 2012.

23. Denton, J. “The Effects of Lean and Sweep on Transonic Fan Performance: A Computational Study.” Task Quarterly 6, No1 7-23., 2002.

24. Denton, J., and G. Pullan. “A Numerical Investigation into the Sources of Endwall Loss in Axial Flow Turbines.” *GT2012-69173.* ASME Turbo Expo 2012: Turbine Technical Conference and Exposition, 2012.

25. Denton, J.D. “The 1993 IGTI Scholar Lecture: Loss Mechanisms in Turbomachines.” *Journal of Turbomachinery*, 1993.

26. Denton, J.D. “The 1993 IGTI Scholar Lecture: Loss Mechanisms in Turbomachines.” *Journal of Turbomachinery*, 1993.

27. Denton, JD. “Some Limitations of Turbomachinery CFD.” *GT2010-22540.* Proceedings of ASME Turbo Expo: Power for Land, Sea and Air, 2010.

28. Denton, JD, and Liping Xu. “The exploitation of three-dimensional flow in turbomachinery design.” *Proceedings of the Institution of Mechanical Engineers* . Part C: Journal of Mechanical Engineering Science, 1998. 125-137.

29. Denton, JD, and WN Dawes. “Computational fluid dynamics for turbomachinery design.” *Proceedings of the Institution of Mechanical Engineers Part C: Journal of Mechanical Engineering Science*, 1998: 213. pp. 107-124.

30. El-Gendi, M.M., M.K. Ibrahim, K. Mori, and Y. Nakamura. *Elliptic Trailing Edge for a High Subsonic Turbine Cascade.*

31. Finzel, C., M. Schatz, M. V. Casey, and D. Gloss. “Experimental Investigation of Geometrical Parameters on the Pressure Recovery of Low Pressure Steam Turbine Exhaust Hoods.” *Proceedings of ASME Turbo Expo.* ASME, 2011.

32. Fu, J. L., J. J. Liu, and S. J. Zhou. “Unsteady Interactions Between Axial Turbine and Nonaxisymmetric Exhaust Hood Under Different Operational Conditions.” *ASME Journal of Turbomachinery*, 2012: Vol. 134.

33. Fukuda, H.; Ohyama, H; Miyawaki, T; Mori, K; Kadoya, Y; Hirakawa, Y. *Development of 3,600-rpm 50-inch/3,000-rpm 60-inch Ultra-long Exhaust End Blades.* Vol. 46 No. 2, Mitsubishi Heavy Industries Technical Review, 2009.

34. Gallimore, S. J. “Viscous throughflow modelling of axial compressor blade rows using a tangential blade foce hypothesis.” *97-GT-415.* ASME , 1997.

35. Gallimore, S. J., and N. A. Cumpsty. “Spanwise mixing in multistage axial flow compressors, Part 1.” *ASME Journal of Turbomachinery, Vol 108,* 1986.

36. Gottlich, E. “Research on the Aerodynamics of Intermediate Turbine Diffusers.” *Progress in Aerospace Sciences, Elsevier,* 2011: Volume 47, Issue 4, p. 249-279.

37. Goudkov, E.I., M.A. Nikolaev, V.V. Ris, E.M. Smirnov, and L. Tajc. *Influence of Tip-Clearance Jet Leakage on Efficiency of Working Fluid Injection into the Diffuser as Applied for Reduction of Exhaust Hood Losses.* London, 17 12 2014.

38. Greitzer, E. M., C. S. Tan, and M. B. Graf. *Internal Flow - Concepts and Applications.* . Cambridge University Press., 2004.

39. H, Chunill, RC Douglas, and AR Wadia. “Role of Tip-Leakage Vortices and Passage Shock in Stall Inception in a Swept Transonic Compressor Rotor.” *GT2004-53867.* ASME Turbo Expo: Power for Land, Sea, and Air, 2004.

40. Haller and Hesketh. “Large Steam Turbine Retrofitting to Improve Performance.” *Power-Gen Europe.* 1993.

41. Haller, B. “Development of New High AN2 Last LP Stage Turbine and Exhaust Systems - A Cost Effective Solution for the 21st Century.” *GT2006-90009.* Reno-Tahoe,Nevada: Proceedings of TURBO EXPO: Land, Sea & Air, 2005.

42. Havakechian, Said; Denton, John;. “3D BLADE STACKING STRATEGIES AND UNDERSTANDING OF FLOW PHYSICS IN LOW PRESSURE STEAM TURBINES PART I - 3D STACKING MECHANISMS.” *Proceedings of ASME Turbo Expo 2015: Turbine Technical Conference and Exposition.* 2015.

43. He, L., and W. Ning. “Efficient Approach for Analysis of Unsteady Viscous Flows in Turbomachines.” *American Institute of Aeronautics and Astronautics,* 1998: 36(11), pp. 2005-2012.

44. Hirschmann, A., S. Volker, M. Casey, and M. Montgomery. “Hub extension in an Axial Gas Turbine Diffuser.” *GT2012-68832.* Copenhagen, Denmark: Proceedings of ASME, Turbo Expo, 2012.

45. Hirschmann, A., S. Volkmer, M. Schatz, C. Finzel, M. Casey, and M. Montgomery. “The Influence of the Total Pressure Profile on the Performance of Axial Gas Turbine Diffusers.” *Journal of Turbomachinery,* 2012: Vol. 134.

46. Huntsman, I., J. D. Denton, and W. N. Dawes. *Numerical Methods in Turbomachinery.* Cambridge Turbomachinery Course, 2004.

47. Japikse, D., and N. C. Baines. *Diffuser Design Technology.* Concepts Eti; 2 edition, 1998.

48. Jung, Y., M. Choi, S. Oh, and J. Baek. "Effects of a Nonuniform Tip Clearance Profile on the Performance and Flow Field in a Centrifugal Compressor." *International Journal of Rotating Machinery*, 2012: 11.

49. Kreitmeier, F., and R. Greim. "Optimisation of Blade-Diffuser Interaction for Improved Turbine Performance." *Proceedings of ImechE Part A, Journal of Power and Energy*, 2003: 217(4), pp 443-451.

50. Krishnababu, S. K., et al. "Aerothermal Investigations of Tip Leakage Flow in Axial Flow Turbines - Part 1: Effect of Tip Geometry and Tip Clearance Gap." *Journal of Turbomachinery*, 2009a: Vol. 131.

51. Krishnababu, S.K., W.N. Dawes, H.P. Hodson, G.D. Lock, J. Hannis, and C. Whitney. "Aerothermal Investigations of Tip Leakage Flow in Axial Flow Turbines - Pat 2: Effect of Relative Casing Motion." *Journal of Turbomachinery*, 2009b: Vol. 131.

52. Kuschel, M., and J. R. Seume. "Influence of Unsteady Turbine Flow on the Performance of an Exhaust Diffuser." *GT2011-45673.* Proceedings of ASME Turbo Expo 2011, 2011.

53. Lewis, K. L. "Spanwise Transport in Axial Flow Turbines, Pts 1 & 2." *93-GT-289 & 290.* ASME, 1990.

54. Li, J., Z. Li, and Z. Feng. "Effects of the Last Stage Rotor Tip Leakage Flow on the Aerodynamic Performance of the Exhaust Hood for Steam Turbines." *GT2013-94377.* Proceeding of ASME Turbo Expo, 2013.

55. Li, Z., J. Li, X. Yan, Z. Feng, H. Ohyama, and M. Zhang. "Investigations on the flow pattern and aerodynamic performance of last stage and exhaust hood for large power steam turbines." *GT2012-69291.* ASME Turbo Expo 2012: Turbine Technical Conference and Exposition, 2012.

56. Liu, J J, Y Cui, and H Jiang. “Investigation of Flow in a Steam Turbine Exhaust Hood with/without Turbine Exit Conditions Simulated.” *Journal of Engineering Gas Turbines Power* , 2001: 125(1), 292-299 .

57. Liu, J. J., and T. P. Hynes. “The Investigation of Turbine and Exhaust Interactions in Asymmetric Flows— Blade-Row Models Applied.” *ASME Journal of Turbomachinery*, 2003.

58. Liu, J.J., and T. P. Hynes. “The Investigation of Turbine and Exhaust Interactions in Asymmetric Flows Part 1 - Blade-Row Models Applied.” *Journal of Turbomachinery*, 2002a: 125(1), 121-127 .

59. —. “The Investigation of Turbine and Exhaust Interactions in Asymmetric Flows Part 2 - Turbine-Diffuser-Collector Interactions.” *GT2002-30343.* ASME Turbo Expo 2002: Power for Land, Sea, and Air, 2002b.

60. Luckemeyer, N., H. Almstedt, T.-U. Kern, and H. Kirchner. “Mechanical Design of Highly Loaded Large Steam Turbines.” *GT2011-45703.* Proceedings of the ASME Turbo Expo, 2011.

61. Mahle, I., and R. Schmierer. “Inverse Fin Arrangement in a Low Pressure Turbine to Improve the Interaction between Shroud Leakage Flows and Main Flow.” *GT2011-45250.* Proceedings of ASME Turbo Expo, 2011.

62. Maier, R., and J. Wachter. “Shock-Induced Flow Oscillations in Steam Turbine Diffusers.” *Journal of Turbomachinery*, 1988: Vol. 110.

63. McBean, I.; Havakechian, S.; Masserey, P.-A. “The Development of Long Last Stage Steam Turbine Blades.” *GT2010-22747.* ASME Turbo Expo 2010: Power for Land, Sea, and Air, 2010.

64. McDonald, A. T., R. W. Fox, and R. V. Dewoestine. “Effects of swirling inlet flow on pressure recovery in conical diffusers.” *American Institute of Aeronautics and Astronautics Paper.* 1971.

65. Miller, R.J., and J.D. Denton. In *Cambridge Turbomachinery Course*. 2012.

66. Mizumi, S., K. Ishibashi, and Y. Sawamura. “Steam Turbine Exhaust Hood with Swirl Flow Separation Ducts.” *GT2012-68315.* Proceedings of ASME, 2012.

67. Mizumi, S.; Ishibashi, K. “Design Philosophy and Methodology of a Low Pressure Exhaust Hood for a Large Power Steam Turbine.” *GT2013-94303.* Proceedings of ASME Turbo Expo, 2013.

68. Musch, C., H. Stuer, and G. Hermle. “Optimization Strategy for a Coupled Design of the Last Stage and The Successive Diffuser in a Low Pressure Steam Turbine.” *GT2011-46180.* Proceedings of ASME Turbo Expo, 2011.

69. Musch, C., R. Sievert, H. Stuer, and H. Stoff. “Performance Aspects of the Shroud and Cavity Design in the Last Stage of a Low Pressure Turbine.” *Proceedings of 8th European Turbomachinery Conference,* 2009.

70. Ong, J, RJ Miller, and JD Denton. “The prediction of hot streak migration in a high-pressure turbine.” *Proceedings of the Institution of Mechanical Engineers, Part A: Journal of Power and Energy,* 2010: 224. pp. 119-128.

71. Ono, H., S. Senoo, T. Kudo, and K. Murata. “The effects of the Tangential Leans for the Last Stage Nozzles of Steam Turbine.” *GT2013-95827.* Proceedings of ASME Turbo Expo, 2013.

72. Pacala, S., and R. Socolow. “Stabilization Wedges: Solving the Climate Problem for the Next 50 Years with Current Technologies.” *VOL 305 SCIENCE www.sciencemag.org,* 13 August 2004: 968-972.

73. Peacock, R.E. “A Review of Turbomachinery Tip Gap Effects: Part 1 - Cascades.” *International Journal of Heat and Fluid Flow,* 1982: Vol. 3, No. 4, pp. 185-194.

74. Peacock, R.E. “A Review of Turbomachinery Tip Gap Effects: Part 2 - Rotating Machinery.” *International Journal of Heat and Fluid Flow*, 1983: Vol. 4, No. 1, pp. 3-16.

75. Pianko, M., and F. Wazelt. *Suitable Averaging Techniques in Non-Uniform Internal Flows.* Propulsion and Energetics Panel Working Group 14, AGARD Advisory Report No. 182, 1983.

76. Prasad, A. “Calculation of the Mixed-Out State in Turbomachine Flows.” *Transactions of ASME*, 2005: 564-572. Vol. 127, July - 2005.

77. “Private communication with Alstom Power, Rugby, UK.” 2012.

78. Raj, K. S. Sunder. “Last Stage Performance Considerations in Low-Pressure Turbines of Power Plants: A Case Study.” *Journal of Engineering for Gas Turbines and Power*, 2008: March-08, Vol. 130.

79. Rosic, B., JD Denton, and G. Pullan. “The importance of shroud leakage modeling in multistage turbine flow calculations.” *Transactions of ASME, Journal of Turbomachinery*, 2006: 128. pp. 699-707.

80. Ruhl, C. “BP Energy Outlook 2035.” London, United Kingdom, 2014.

81. Sakuma, A., T. Matsuura, and H. Kodama. “Steam Turbine Retrofits Technology for Improved Performance and Reliability.” *Challenges of Power Engineering and Environment*, 2007: 251-257 Vol 1-2.

82. Senoo, S. “Development of Design Method for Supersonic Turbine Aerofoils near the Tip of Long Blades in Steam Turbines. Part 1: Overall Configuration.” *GT2012-68218*. Proceedings of ASME Turbo Expo, 2012.

83. —. “Development of Design Method for Supersonic Turbine Aerofoils near the Tip of Long Blades in Steam Turbines. Part 1: Overall Configuration.” *Proceedings of ASME Turbo Expo - GT2012-68218*. 2012.

84. Sharma, O.P., and T.L. Butler. “Predictions of endwall losses and secondary flows in axial flow turbine cascades.” *86-GT-228*. ASME, 1986.

85. Sieverding, C. “Recent Progress in the Understanding of Basic Aspects of Secondary Flows in Turbine Blades Passages.” *Transactions of ASME, Journal of Engineering for Gas Turbines and Power*, 1985: p. 248.

86. Socolow, R. H., and S. H. Lam. “Good enough tools for global warming.” *Philosophical Transactions of The Royal Society*, 2007: 897-934.

87. Sovran, G, and ED Klomp. “Experimentally determined optimum geometries for rectilinear diffusers with rectangular, conical or annular cross section.” *Fluid Mechanics of Internal Flow, Elsevier Publishing*, 1967: 270-319.

88. Spalart, P. R., and S. R. Allmaras. “A One-Equation Turbulence Model for Aerodynamic Flows .” *La Recherche Aerospatiale No. 1*, 1994: pp. 5-21.

89. Starzmann, J., M. Schatz, M. V. Casey, and J. F. Mayer. “Modelling And Validation of Wet Steam Flow in a Low Pressure Steam Turbine.” *GT2011-45672.* Proceedings of ASME Turbo Expo, 2011.

90. Stastny, M., L. Tajc, P. Kolar, and A. Tucek. “Effects of Inlet Swirl on the Flow in a Steam Turbine Exhaust Hood.” *Journal of Thermal Science,* 2000: Vol. 9, No. 4.

91. Stastny, M., P. Kolar, and A. Tucek. “3D Flow in the Axial-Radial Exhaust Hood of a Steam Turbine.” *Journal of Thermal Science Vol. 6, No. 4.*, 1997.

92. Stuer H., Truckenmuller F., Borthwick D., Denton JD. “Aerodynamic Concept for Very Large Steam Turbine Last Stages. .” *GT2005-68746 - ASME Turbo Expo: Power for Land, Sea and Air.* 2005.

93. Stuer, H., F. Truckenmuller, D. Borthwick, and J. Denton. “Aerodynamic Concept for Very Large Steam Turbine Last Stages.” *GT2005-68746.* ASME Turbo Expo 2005: Power for Land, Sea and Air., 2005.

94. Tanuma, T., et al. “Numerical Investigation of Exhaust Diffuser Performances in Low Pressure Turbine Casings.” *GT2011-45677.* Proceedings of ASME Turbo Expo 2011, 2011.

95. Tanuma, T., Y. Sasao, S. Yamamoto, Y. Niizeki, N. Shibukawa, and H. Saeki. “Numerical Investigation of Three-Dimensional Wet Steam Flows in an Exhaust Diffuser with Non-Uniform Inlet Flows from the Turbine Stages in a Steam Turbine.” *GT2012-69496.* Proceedings of ASME Turbo Expo, 2012.

96. Thorpe, S. J., R. J. Miller, S. Yoshino, R. W. Ainsworth, and N. W. Harvey. “The effect of work processes on the casing heat transfer of a transonic turbine.” *Transactions of ASME*, 2007: p84-91/Vol. 129.

97. Tyler, R. D., and A. H. Shapiro. “Pressure Rise Required for Separation in Interaction Between Turbulent Boundary-Layer and Shock-Wave.” *JAS*, 1953: Vol. 20, No. 12, pp. 858-860.

98. Volkmer, S., B. Kuschel, A. Hirschmann, M. Schatz, M. Casey, and M. Montogomery. “Hub Injection Flow Control in a Turbine Exhaust Diffuser.” *GT2012-69713.* Proceedings of ASME Turbo Expo, 2012.

99. Wallace, J.D., and M.R.D. Davies. “Entropy Generation Measurement in a Laminar Turbine Blade Boundary-Layer.” *97-GT-450.* ASME, 1997.

100. Yamamoto, A., K. Kaba, and T. Matsunuma. “Measurement and Visualisation of Three-Dimensional Flows in a Linear Turbine Cascade.” *95-GT-341.* ASME, 1995.

101. Yaras, M.I., and S.A. Sjolander. “Prediction of tip leakage losses in axial turbines.” *ASME Journal of Turbomachinery*, 1991: 114, 204 - 210.

102. Yoon, S., F. J. Stanislaus, G. Singh, and M. Claridge. “A Three-Dimensional Diffuser Design for the Retrofit of a Low Pressure Turbine using In-House Exhaust Design System.” *GT2011-45466.* Proceedings of ASME Turbo Expo 2011: Power for Land, Sea and Air, 2011.

103. Yoon, S., R. Selmeier, P. Cargill, and P. Wood. “Effect of the Stator Hub Configuration and Stage Design Parameters on Aerodynamic Loss in Axial Compressors.” *GT2014-26095.* Proceedings of ASME Turbo Expo, 2014.

104. Zachary, Justin; Koza, Donald J. “The long and short of last-stage blades.” *Bechtel Power Corp.*, 15 December 2006.

105. Zhang, L.Y., L. He, and H. Stuer. “A Numerical Investigation of Rotating Instability in Steam Turbine Last Stage.” *Journal of Turbomachinery*, 2013: Vol. 135/011009-1.